


## RESEARCH ARTICLE

# An assessment and thermodynamic analysis of an actual power plant in the frame of a tri-generation concept

Emrah Özahi\*<sup>1</sup> <sup>1</sup>Gaziantep University, Engineering Faculty, Mechanical Engineering Department, Gaziantep, Türkiye

## Article Info

### Article history:

Received: 07.03.2024

Revised: 26.06.2024

Accepted: 29.09.2024

Published Online: 24.10.2024

### Keywords:

Gas power plant

Thermodynamic analysis

Thermal efficiency

Brayton cycle

S-CO<sub>2</sub> cycle

## Abstract

In the case of technological developments, energy consumption is rising. Due to this reason, it is essential for more efficient use of limited energy resources all over the world. The waste energy should be recovered for useful applications. Moreover, the improvements in terms of system efficiency and environmental impacts should be utilized for conventional power plants in the frame of co/tri-generation systems as well as waste-to-energy concept. For all these reasons, in coal-fired power plants and other power cycle enhancement studies, supercritical and ultra-supercritical conditions are being designed for more efficient power plants. In this study, a conventional gas power plant was analyzed in terms of thermodynamic aspect and some recommendations were developed in order to increase the system efficiency. As a result of the thermodynamic analyses, the thermal efficiency of the plant was found to be 43.78%. The aim of this paper is to point out the importance of tri-generation systems that can be adapted to existing ones in order to increase system efficiency.

## 1. Introduction

Nowadays, energy consumption is increasing all over the world and its scarce amount leads to people to find out alternative solutions for efficient usage of energy. With population growth in the world, energy consumption is also increasing. It is possible to increase the efficiency of a system by decreasing the exergetic losses and/or adapting new auxiliary systems to the existing ones. The most important attempt that can be achieved in this respect is energy recovery by utilizing waste energy. In this phenomenon, first of all, the updated portrait of any system should be outlined thermodynamically. There are many studies in which thermodynamic and thermoeconomic analyses were made in this respect in the open literature [1-4]. As a result of these comprehensive analyses on actual systems, in order to increase the system efficiency, optimization studies are also performed [5-8]. An actual system's efficiency can be recovered by using many different systems such as gas turbines, supercritical CO<sub>2</sub> (S-CO<sub>2</sub>) cycles, Brayton, organic Rankine and Kalina cycles. Such as; Organic Rankine cycle (ORC) is an alternative solution for low-grade thermal energy recovery technology, which is utilized to all kinds of low-temperature heat sources including geothermal, solar, biomass and especially waste heat energies [9]. A power cycle with ammonia-water mixtures as a working fluid can be used for waste heat in order to improve the efficiency of a power plant. This cycle is named as Kalina cycle which was designed by Alexander Kalina using a bottoming cycle instead of the Rankine cycle in combined cycle power plants in 1989 [10]. A study on the S-CO<sub>2</sub> cycle in the open literature [7] was seen to optimize energy production of actual power plants. Besides this, for thermoeconomic optimization of actual power plants after well-performed

thermodynamic analyses, a method named as specific exergy costing (SPECO) method can be utilized [11, 12]. Besides this, the utilized systems can also be considered in the frame of co/tri-generation concept in the purpose of an efficiency increase. Herein a tri-generation is a simultaneous production of electricity and heat as well as cooling from a single energy source.

In the concept of more efficient power plants, a well-known Brayton cycle can be utilized. The Brayton cycle emerged for use in a two-stroke kerosene-fired reciprocating engine was patented by US engineer George Brayton in 1872. The components in gas turbines are; gas compressor, combustion chamber and expansion turbine. Air enters the compressor and pressurized. Compressed air is then burned with fuel and the burned air expands in the turbine stages, providing mechanical energy. Although the thermal efficiency of open cycle gas turbine systems is quite low, they are preferred because of their rapid commissioning and low investment costs compared to other systems. All gas turbine systems are operated by the so-called Brayton Cycle and produce mechanical power.

Moreover, supercritical fluids are of interest to the scientific community with their superior solvent properties, which can be changed easily by temperature and pressure. Among the supercritical fluids, thanks to its low critical temperature and critical pressure values, carbon dioxide solvent is frequently used because of not being toxic to the environment. S-CO<sub>2</sub> is a fluid state of carbon dioxide which is held above the critical pressure and critical temperature point, behaving similar to that of a liquid. This allows a significant reduction in the pumping power needed in a compressor and a

significant increase in the thermal energy-electric energy conversion efficiency.

In accordance with the information given above, in this paper, by combining the advantages of Brayton and S-CO<sub>2</sub> cycles, a study was carried out in the concept of tri-generation system. Thermodynamic analyses of an actual power plant as well as tri-generation system are presented. As a result, a tri-generation system to increase overall efficiency of the actual systems is suggested herein in general manner.

**2. Materials and Methods**

In the thermodynamic analyses of the actual power plant as well as the tri-generation system, Engineering Equation Solver (EES) program was used using the actual data of the plant. The actual operating data were taken and under the light of those, the system was analyzed thermodynamically. The schematic layout of the actual power plant with the proposed tri-generation system is given in Fig. 1.

The actual data of the plant are tabulated in Table 1. The operating pressure, temperature and mass flow rate data of the three working fluids such as air, water and S-CO<sub>2</sub> were taken from the system. The inlet and exit states of each device were numbered sequentially and then the thermodynamic analyses were performed in EES program in this manner.

For thermodynamic analyses, the well-known equations which are given below were used. For the mass balance throughout all devices, continuity equation for control volumes was used in the presence of steady state steady flow conditions as:

$$\sum \dot{m}_i = \sum \dot{m}_e \tag{1}$$

where  $\dot{m}$  is the mass flow rate and sub-indices  $i$  and  $e$  represent *inlet* and *exit* states, respectively. The first law of thermodynamics for steady state steady flow processes throughout the related control volumes which are given in Fig. 1 in the absence of the change in both kinetic and potential energies, is given as:

$$\dot{Q} - \dot{W} = \sum \dot{m}_e h_e - \sum \dot{m}_i h_i \tag{2}$$

After analyzing each control volume in the proposed system, the thermal efficiency of the system is evaluated by using the Eq. (3) as:

$$\eta_{th} = \dot{W}_{net} / \dot{Q}_H \tag{3}$$

where  $\eta_{th}$  is the thermal efficiency of the system,  $\dot{W}_{net}$  is the net power output,  $\dot{Q}_H$  is the heat transfer rate to the system from high temperature reservoir.

**3. Results and Discussion**

As a result of the thermodynamic analyses, the amount of heat transfer rate to/from system devices and the amount of power produced/consumed by each device were evaluated using the actual operating data and then tabulated in Table 2.

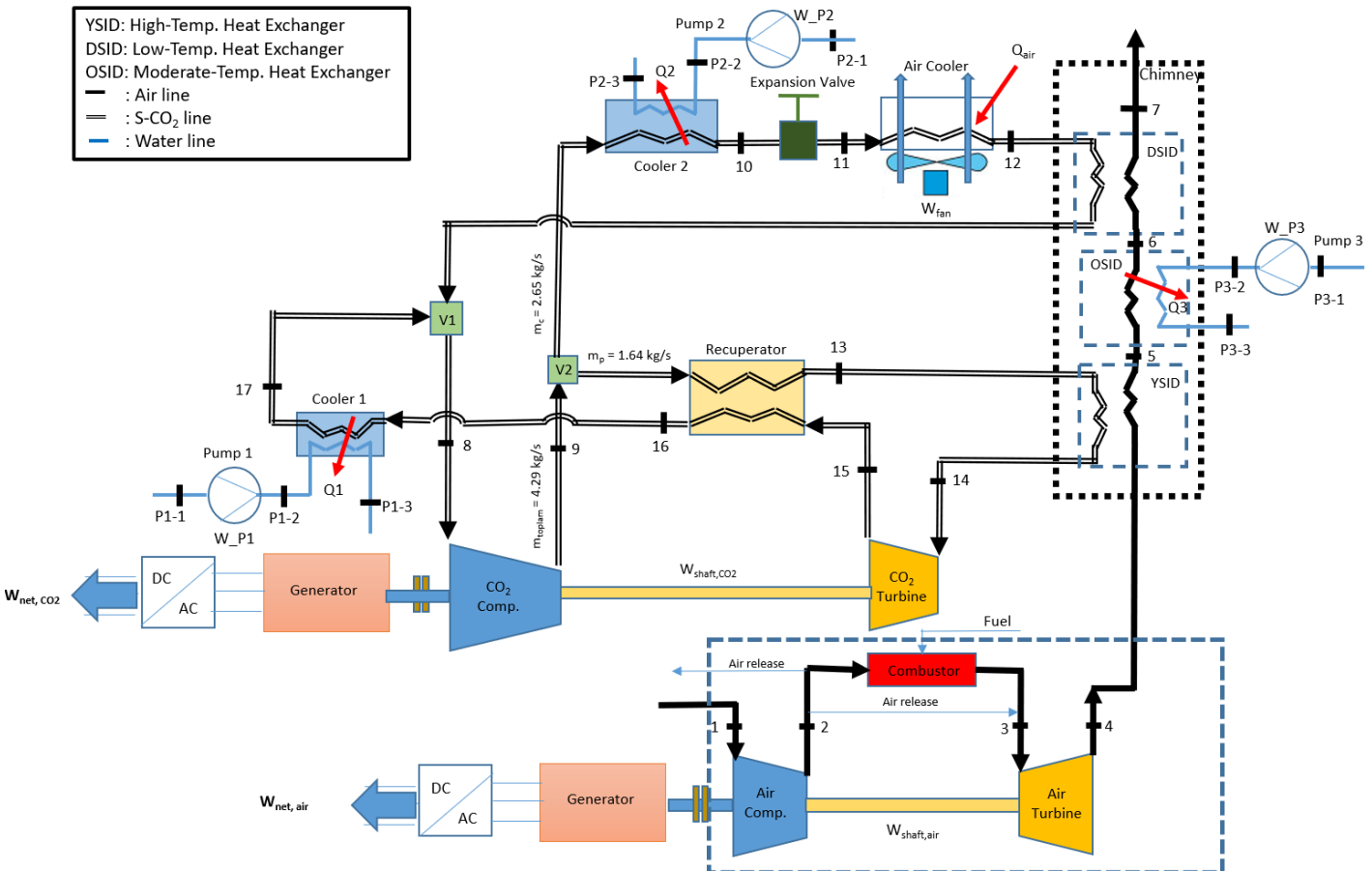


**Figure 1.** The schematic layout of the system

**Table 1.** Thermodynamic properties of the states in the plant

State	Fluid	P (bar)	T (°C)	$\dot{m}$ (kg/s)
1	air	1.01	20	1.71
2	air	14.2	420	1.71
2 -1	air evacuation (%15)	14.2	420	1.45
3	air	13.5	1250	1.45
3 -1	air evacuation (%5)	13.5	1250	1.62
4	air	1.8	801	1.62
5	air	1.5	460	1.62
6	air	1.3	97	1.62
7	air	1.03	47	1.62
8	S-CO <sub>2</sub>	78	32	4.29
8 -v1	S-CO <sub>2</sub>	78	32	2.65
9	S-CO <sub>2</sub>	230	64	4.29
9-v2-mp	S-CO <sub>2</sub>	230	64	1.64
9 -v2-mc	S-CO <sub>2</sub>	230	64	2.65
10	S-CO <sub>2</sub>	229	23	2.65
11	S-CO <sub>2</sub>	17.1	78	2.65
12	S-CO <sub>2</sub>	77.8	27	2.65
13	S-CO <sub>2</sub>	229	435	1.64
14	S-CO <sub>2</sub>	229	721	1.64
15	S-CO <sub>2</sub>	78.4	581	1.64
16	S-CO <sub>2</sub>	78.2	99	1.64
17	S-CO <sub>2</sub>	78	32	1.64
P1-1	water	1.01		1.44
P1-2	water	20	27	1.44
P1-3	water	10	95	1.44
P2-1	water	1.01		1.45
P2-2	water	20	20	1.45
P2-3	water	77.8	27	1.45
P3-1	water	1.01		1.99
P3-2	water	20	25	1.99
P3-3	water	10	95	1.99

The turbine and compressor were considered as isentropic ones. The work produced by the air turbine was found as 864 kW and the work consumed by the compressor was evaluated as 706 kW with their evaluated isentropic efficiencies of 75.86% and 80.06%, respectively. The work produced by the turbine in the S-CO<sub>2</sub> line was 276 kW besides the work consumed by the compressor was 114 kW. It was seen that the network for both air and S-CO<sub>2</sub> line systems was almost 150 kW. As a result of the thermodynamic analyses, the overall thermal efficiency of the system was found as 43.78%.

**Table 2.** Thermodynamic results

States	Devices	$\dot{Q}$ (kW)	$\dot{W}$ (kW)
1 -2	Air Compressor	-	706
2 -3	Combustion Chamber	708	-
3 -4	Air Turbine	-	864
4 -5	Air High-Temp. Heat Exch.	626	-
5 -6	Air Moderate-Temp. Heat Exch.	609	-
6 -7	Air Low-Temp. Heat Exch.	83	-
8 -9	S-CO <sub>2</sub> Compressor	-	114
9 -10	Cooler 2	239	-
11-12	Fan	87	-
13 -14	S-CO <sub>2</sub> High-Temp. Heat Exch.	592	-
14-15	S-CO <sub>2</sub> Turbine	-	276
15-16	Recuperator	922	-
9-13	Recuperator	921	-
16-17	Cooler 1	358	-
8 -12	S-CO <sub>2</sub> Low-Temp. Heat Exch.	81	-
P1.1- P1.2	Water Pump 1	-	2.85
P2.1- P2.2	Water Pump 2	-	2.87
P2.2- P2.3	Cooler 2	239	-
P3.1- 3.2	Water Pump 3	-	3.94
P3.2- 3.3	Water Moderate-Temp. Heat Exch.	581	-

#### 4. Conclusions

In this study, a thermodynamic analysis of a power plant which was constructed as a couple of two cycles, Brayton and S-CO<sub>2</sub> cycles was performed in order to illustrate the positive effect in energetic efficiency of the system. These systems are called as tri-generation ones in which simultaneous production of electricity and heat as well as cooling from a single energy source are carried out. The importance of co/tri-generation systems is emphasized herein. As a result of the thermodynamic analyses, the thermal efficiency of the power plant was found as 43.78% which is a remarkable value for a typical power plant. As a future study, in the frame of increasing of system thermal efficiency, alternative cycles such as Kalina, organic Rankine and other alternative power cycles can be adapted to conventional power plants to compare their existing thermal efficiencies.



#### References

1. Tozlu, A., Özahi, E., and Abuşoğlu, A., Thermodynamic and Thermoeconomic Analyses of an Organic Rankine Cycle Adapted Gas Turbine Cycle Using S-CO<sub>2</sub>, Journal of the Faculty of Engineering and Architecture of Gazi University, **2018**, 33(5): 917-928
2. Özahi, E., Tozlu, A., and Abuşoğlu, A., Thermodynamic Performance Assessment of Different Fluids in a Typical

- Organic Rankine Cycle for Usage in Municipal Solid Waste Power Plant, *Acta Physica Polonica A*, **2017**, 132: 807-812
3. Tozlu, A., Abuşoğlu, A., and Özahi, E., Thermoeconomic Analysis and Assessment of Gaziantep Municipal Solid Waste Power Plant, *Acta Physica Polonica A*, **2017**, 132: 513-517
  4. Tozlu, A., Abuşoğlu, A., and Özahi, E., Comparison of Five Developed Power Cycles in the frame of Waste Heat Recovery, *The International Journal of Materials and Engineering Technology (TIJMET)*, **2021**, 4(1): 1-9
  5. Özahi, E., Abuşoğlu, A., and Tozlu, A., A Comparative Thermoeconomic Analysis and Optimization of Two Different Combined Cycles by Utilizing Waste Heat Source of an MSWPP, *Energy Conversion and Management*, **2021**, 228: Article number 113583
  6. Özahi, E., and Tozlu, A., Optimization of an Adapted Kalina Cycle to an Actual Municipal Solid Waste Power Plant by Using NSGA-II Method, *Renewable Energy*, **2020**, 149: 1146-1156
  7. Tozlu, A., Abuşoğlu, A., and Özahi, E., Thermoeconomic Analysis and Optimization of a Re-compression Supercritical CO<sub>2</sub> Cycle Using Waste Heat of Gaziantep Municipal Solid Waste Power Plant, *Energy*, **2018**, 143: 168-180
  8. Özahi, E., Tozlu, A., and Abuşoğlu, A., Thermoeconomic Multi-Objective Optimization of an Organic Rankine Cycle (ORC) Adapted to an Existing Solid Waste Power Plant, *Energy Conversion and Management*, **2018**, 168: 308-319
  9. Kaşka, Ö., Energy and Exergy Analysis of an Organic Rankine for Power Generation from Waste Heat Recovery in Steel Industry, *Energy Conversion and Management*, **2014**, 77: 108-117
  10. Thorin, E., Power Cycles with Ammonia-Water Mixtures as Working Fluid: Analysis of Different Applications and the Influence of Thermophysical Properties, Stockholm, Sweden:RoyalInstitute of Technology, **2000**
  11. Abuşoğlu, A., and Kanoglu, M., Exergetic and Thermoeconomic Analyses of Diesel Engine Powered Cogeneration: Part 1 – Formulations, *Applied Thermal Engineering*, **2009**, 29: 234-241
  12. Abuşoğlu, A., and Kanoglu, M., Exergetic and Thermoeconomic Analyses of Diesel Engine Powered Cogeneration: Part 2 – Application, *Applied Thermal Engineering*, **2009**, 29: 242-249

## RESEARCH ARTICLE

# Optimization of titanium oxide nanoparticle enrichment on the tribological properties of sandbox bio-lubricant

Caleb Abiodun Popoola<sup>1</sup>  and Okwuchi Smith Onyekwere<sup>1\*</sup> <sup>1</sup>Federal University Wukari, Faculty of Engineering, Department of Chemical Engineering, Taraba State, Nigeria

## Article Info

### Article history:

Received: 10.05.2024

Revised: 05.07.2024

Accepted: 29.09.2024

Published Online: 24.10.2024

### Keywords:

Sandbox seed oil

Lubrication

Wear rate

Coefficient of friction

## Abstract

Improvement of Lubricant properties is encouraged in production industries for enhanced performance. This study investigated the effect of titanium oxide nanoparticle additive on the tribological properties of sandbox bio-lubricant. Titanium oxide nanoparticle-enriched sandbox bio-lubricant was developed by adding varying concentrations of the nanoparticle to sandbox lubricant. Central composite design was employed for the experimental design and optimization. The lubricant was enriched with nanoparticle concentration of 0 wt%, 0.75 wt%, and 1.50 wt %. The parameters values used for the evaluation were: load (2 N, 5 N, and 8 N) and speed (150 rpm, 200 rpm, and 250 rpm). Effects of these values on wear rate, friction coefficient and flash temperature parameter were evaluated. The lowest values of coefficient of friction and wear rate were obtained at a speed of 200 rpm and concentration of 0.75 wt% with 2 N load, which lead to a 78.3% and 15.3% reduction in coefficient of friction and wear rate respectively over that of pure sandbox bio-lubricant. The optimal parameters combinations for minimum coefficient of friction and wear rate as well as maximum flash temperature were: 8.0N load, 199.49rpm speed and a 0.71wt% concentration which leads to a coefficient of friction of 0.045 which is lower than that of pure sandbox bio-lubricant at all levels. The wear rate at the optimum setting is 0.0171 which is lower than that of pure sandbox at the same 8.0N load. The observed flash point at the optimal settings is 0.0381 which is higher than that of pure sandbox bio-lubricant at all levels of load and rpm. The titanium oxide nanoparticle added to sandbox lubricant improved the tribological properties of the lubricant by increasing the anti-friction and anti-wear ability of the lubricant. This shows the potential of titanium oxide nanoparticle as additive for bio-lubricant production.

## 1. Introduction

Lubricants play crucial roles in extending the life of equipment by lubricating, suspending, cooling, cleaning, and protecting metal surfaces [1]. These substances are employed in tribological contacts to separate the contacting surfaces' peak asperities. According to Jackson [2], lubricants defend against corrosion, dissipate heat, exclude impurities, and flush away wear products. According to Khasbage *et al.* [3], a lubricant should be able to transport protection chemicals to the contacts where they are needed while also moving wear particles away from the source. Lubricants should be effective in all driving circumstances, including short trips and cold starts.

According to Gulzar [4] and Shahnazar *et al.* [5], lubricants fall into three categories: mineral lubricants, natural lubricants, and synthetic lubricants. According to Chandan *et al.* [6], the majority of mineral lubricants are petroleum-based and they are widely used. Because of their superior biodegradability and renewable feedstock, natural lubricants—those made from plant- and animal-based fats and oils—are considered to be more environmentally friendly than synthetic lubricants, which are made through chemical synthesis from a variety of materials, including olefins, aromatics, alcohols, acids, and halogenated compounds.

According to Naik and Galhe [7], numerous research has demonstrated that vegetable oils, such as oleic and palmitic,

are the optimum feedstock for lubricants since they include monounsaturated fatty acids. Because of the action of the highly polar fatty acids which forms protective hydrocarbon coatings on the metal surfaces, vegetable oils work well as a boundary lubricant. According to Hassan *et al.* [8], the ester groups in sandbox oil give it a strong affinity for metal surfaces, forming protective layers on surfaces that come into touch with it.

Nanoparticles, which have the potential to reduce wear and friction, are emerging additives in the lubricant. It has been reported that nanoparticles lubricating effect depend on their concentration, shape and size [9, 10]. The use of nanoparticles as additives to oil is motivated by a number of factors. The key advantage of using nanoparticles is their tiny sizes that allows them to enter the cavities of contact area, which leads to effective lubrication effect [11]. This small size enables them to pass through the filters of the lubrication system without affecting their concentration during use.

Four possible ways the nanoparticles added to base oil act are; protective film, rolling effect, mending effect, and polishing effect [10, 12]. By forming a thin surface protective film with the friction paired surfaces, the nanoparticle in the protective film lowers wear and friction. Spherical nanoparticles roll between contact surfaces in the rolling effect, altering the sliding friction to provide a mixture of rolling and sliding friction. Nanoparticles are applied to the

surface to produce a physical tribofilm that makes up for the mass loss in order to produce the mending effect [10]. The nanoparticle abrasiveness reduces the rubbing surface roughness in the polishing effect.

The performance of titanium oxide nanoparticles as lubricant additives is good because of their low toxicity, non-volatility, anti-oxidant properties, and other pleasant properties [13]. A nanoparticle additive made of titanium oxide ( $\text{TiO}_2$ ) was reported by Le and Lin [14] to have the potential to increase the applicable load, decrease the friction force, and increase the anti-wear properties of the lubricant. Lubricant with titanium dioxide nanoparticle additive was examined by Battez and Rodriguez [15], and it was discovered that the properties of titanium dioxide make it well suited for use in tribological applications. According to Afzal *et al* [16], for titanium oxide nanoparticles dispersed in lubricating oil obtained through sonication process, nanoparticle agglomeration can be avoided by application of surfactant.

Comparing plain oils without nanoparticle additive to those with  $\text{TiO}_2$  nanoparticle lubricant additive, Binu *et al.* [17] showed an improvement in the journal bearing's capacity to carry load. The tribological properties of titanium oxide nanoparticle additive in petroleum-based engine oil were examined by Laad and Jatti [13]. They discovered that adding  $\text{TiO}_2$  nanoparticles to engine oil significantly lowers wear rate and friction, which enhances the lubricating properties of the lubricant. The stability and superior solubility of the titanium oxide nanoparticles in the lubricant are further confirmed by the dispersion investigation.

Traditional lubricant additives, due to their sizes have a challenge of protective film formation on contact surfaces, low durability and poor solubility in non-polar lubricants compared to nanoparticles. This research is aimed at replacing traditional lubricant additives with nanoparticles as a step towards sustainable development of bio-lubricants using sandbox oil – which is abundant in Nigeria. Lubrication potential of titanium oxide nanoparticle and the effect of the nanoparticle on tribological performance of the bio-lubricant were also investigated.

## 2. Materials and methods

The materials and methods employed in this study are highlighted in this section.

### 2.1. Materials and equipment

Sandbox (Hura crepitans) oil, methanol, potassium hydroxide, trimethylolpropane (TMP), oleic acid (OA), titanium oxide ( $\text{TiO}_2$ ) nanoparticle, conventional lubricant SAE 40, were among the materials and reagents utilized in this study. Anton Paar ball-on-disc tribometer (Model TRN) was used for the wear test.

Sandbox oil was used because it is abundant in Nigeria and it has been reported to work well in biodiesel – reducing pollution emission while maintaining efficiency [18]. Oleic acid was selected to be used as a surfactant because of its ability to enhance the dispersion stability of the nanoparticle [19]. Potassium hydroxide was selected because of its ability to act as catalyst in methyl ester synthesis using methanol [20]. Conventional lubricant SAE 40 is a common lubricant for engines bearing load within the range of this study and beyond. Thus, it was selected for comparison. Anton Paar ball-on-disc tribometer (Model TRN) was selected to carry out wear test because it is the wear test equipment available where this

research was carried out and the range of parameters tested fall within its capacity. Titanium oxide is used for solid lubricant production and it has been found to improve the tribological properties of conventional engine oil [21]. Thus, it was selected for this study. Trimethylolpropane (TMP) has been found to have good performance in biolubricating oils [22]. It was thus selected for this study.

### 2.2. Methods

The following sequence was followed in carrying out this research; firstly, the materials were collected and prepared, second stage was the production of nanoparticle-enriched sandbox bio-lubricant and finally the tribological evaluation of the bio-lubricants was performed.

#### 2.2.1. Materials collection and preparation

Sandbox (Hura crepitans) seeds were gathered in Wukari town, Taraba State, and appropriately identified at Federal University Wukari's Department of Biological Science. After being washed, the seeds were manually dehulled and then ground in a mill. Using n-hexane as the extraction solvent, the oil was extracted using a Soxhlet extractor. Other chemicals and commercially available titanium oxide nanoparticles were obtained from Bristol Scientific Company Ltd. in Lagos. Sigma-Aldrich, USA, produced the titanium oxide nanoparticles that were used, with a particle size of less than 100 nm.

#### 2.2.2. Formulation of titanium oxide nanoparticle-enriched bio-lubricant

Using sandbox oil as the base oil, a titanium oxide nanoparticle-enriched bio-lubricant was prepared following the guidelines of the ISO 5509 [23] technique as reported by Bilal *et al.* [24]. A double transesterification process—methyl ester synthesis and bio-lubricant synthesis—was used in the formulation. In the initial transesterification, the oil sample was mixed with methanol using potassium hydroxide as a catalyst to produce methyl ester of the oil, an intermediate product. Potassium hydroxide was added at a weight percentage of 0.5% of the oil weight, and the weight ratio of the oil to methanol was 3:1. The required bio-lubricant was produced during the second transesterification by mixing trimethylolpropane (TMP) with the sandbox methyl ester. Attempt was made to enhance the tribological characteristics of the bio-lubricant by adding titanium oxide ( $\text{TiO}_2$ ) nanoparticles at weight percentages of 0.75 wt% and 1.50 wt%. Oleic acid was added as a surfactant to enhance the dispersion stability of the nanoparticle and avoid agglomeration during the dispersion process. Figure 1 shows the formulation process.

The bio-lubricants, designated SB100 (sandbox oil), SBTiO75 (sandbox oil + 0.75 wt%  $\text{TiO}_2$ ), and SBTiO150 (sandbox oil + 1.50 wt%  $\text{TiO}_2$ ), were formulated utilizing varying concentrations of  $\text{TiO}_2$  nanoparticles. The tribological analysis of the bio-lubricant was conducted using Minitab 16.00 software and a three-level, three-factor ( $3^3$ ) factorial design was used. The codes for the levels were -1, 0 and +1. The three factors, referred to as independent variables used are concentration of titanium oxide ( $\text{TiO}_2$ ) nanoparticles with different weight concentrations, speed, and load. The factors and their levels are shown in Table 1. The values selected for the factors were based on a number of studies on nanoparticles-enriched bio-lubricants by Gulzar [4], Abere

[25], Le and Lin [14], Hassan *et al.* [8], Thottackkad *et al.* [26] and Umaru *et al.* [27].

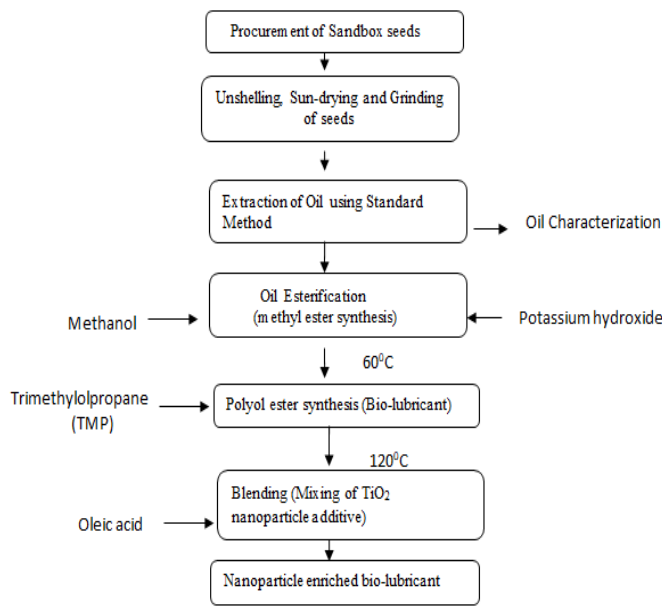


**Figure 1.** Methodology for formulation of nanoparticle-enriched bio-lubricant

**2.3. Tribological evaluation of the bio-lubricant**

Evaluation of the tribological behaviours of the produced lubricant was carried out. Comparison was made between the performance of three categories of lubricants - those with titanium oxide nanoparticles, those without titanium oxide nanoparticles and SAE 40 conventional lubricants. ASTM G99-05 (2010) test method was employed to assess the tribological behaviour of the bio-lubricants. Figure 2 shows the schematic diagram of the ball-on-disc tribometer used. Stainless steel balls of 6 mm diameter were placed in the upper stationary ball holder on a tribometer. A 70 mm diameter and 6.35 mm thick aluminium alloy discs were used. Tests were then conducted on the lubricating oils using the design parameters. 50m was set as the sliding distance and all the tests were done for 5 – 12 minutes duration range. To ensure the required contact conditions, the ball specimen was carefully put into the holder and set perpendicularly to the disc surface. Applying lubricant between the disc and the ball satisfied the requirements for boundary lubrication. The system lever was given the proper load to apply the chosen force that pressed the ball up against the disc.

**Table 1.** Factors and levels for experiment

Factors	Symbol	Level		
		(-1)	(0)	(+1)
Load (N)	A	2.0	5.0	8.0
Speed (rpm)	B	150	200	250
Concentration (wt%)	C	0	0.75	1.50

After adjusting the speed and rotation counter to the proper levels, the electric motor was switched on. Once the required number of revolutions was reached, the test was terminated. After removal, the specimen was cleaned. To determine the wear rate and friction coefficient, the process was repeated for each test. The acquired friction coefficient and wear rate

figures were noted. According to Jabal *et al.* [28], the flash temperature parameter—a figure used to represent the critical flash temperature at which a lubricant will perform satisfactorily under specific circumstances—was also determined for each experimental scenario using equation (1).

$$FTP = \frac{W}{d^{1.4}} \tag{1}$$

where

$W = \text{load (kg)}$

$d = \text{mean wear track diameter } (\mu\text{m})$

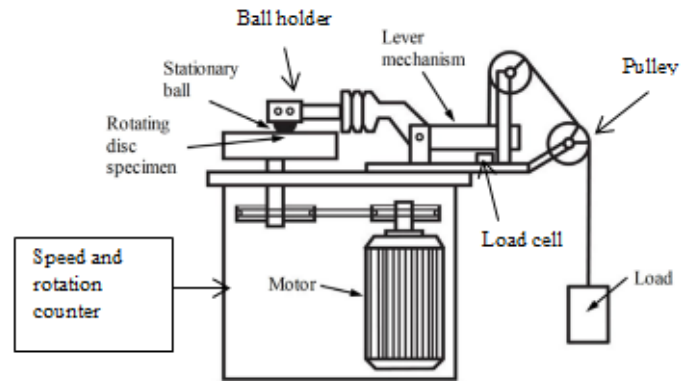


**Figure 2.** Schematic diagram of the Anton Paar ball on disc tribometer used

The disc specimens' surfaces were analysed in line with Gulzar [4] in order to comprehend the lubricant's lubricating mechanism. The research was conducted using scanning electron microscopy, a flexible technique for examining surfaces at a wide variety of magnifications and high resolution. SEM was utilized to scan the sample surface with a focused electron beam, and the image was captured.

**3. Results and discussion**

Description of the experimental results and their interpretation as well as the conclusions drawn is contained in this section.

**3.1. Tribological performance of the formulated bio-lubricant**

Both the developed bio-lubricant and the traditional lubricant SAE 40's tribological capabilities were assessed. Figures 3 through 7 display the observed tribological parameters, such as the wear rate, coefficient of friction, and flash temperature.

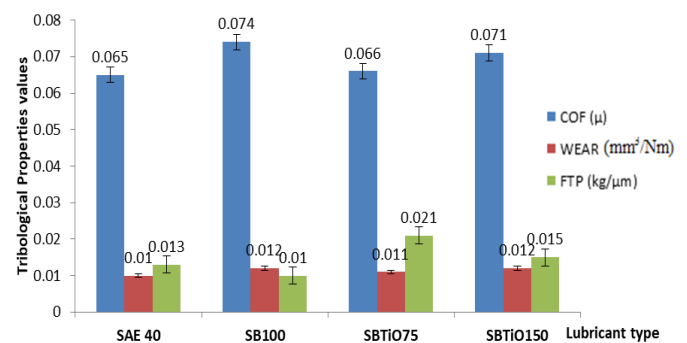


**Figure 3.** Effect of nanoparticle enrichment on coefficient of friction of the bio-lubricants (2 N, 150 rpm)

SAE 40: Conventional lubricant, SB100: Sandbox oil only, SBTiO75: Oil + 0.75 wt% TiO<sub>2</sub>, SBTiO150: Oil + 1.50 wt% TiO<sub>2</sub>

3.2. Effect of nanoparticle enrichment on friction coefficient

Figures 3 through 7 illustrate the effect of nanoparticle enrichment on the friction coefficient at various speeds and loads. The findings demonstrate that nanoparticle-enriched sandbox oil exhibited superior anti-friction properties at some concentrations, weights, and speeds, and poor properties at others. When SBTiO75 and SBTiO150 were compared to pure sandbox oil at 150 rpm and 2 N load, the friction coefficients of the two bio-lubricants were reduced by 10.81% and 4.05%, respectively. Additionally, at 150 rpm with an 8 N load, the friction coefficient decreased by 14.80% for SBTiO75 and 36.40% for SBTiO150. At 200 rpm with a 5 N load, the reductions were 38.96% and 18.18% for SBTiO75 and SBTiO150, respectively, and at 250 rpm with a 2 N load, the reductions were 78.30% and 33.02% for SBTiO75 and SBTiO150, respectively. Friction coefficient increased by 9.33% for SBTiO75 at 250 rpm with an 8 N load, but decreased by 5.88% for SBTiO150. These findings demonstrated that sandbox oil loaded with nanoparticles provides substantially lower friction coefficients than sandbox oil without nanoparticles.

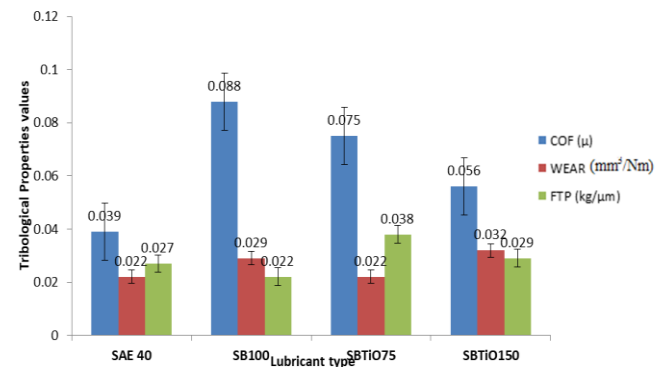


Figure 4. Effect of nanoparticle enrichment on coefficient of friction of the bio-lubricants (8 N, 150 rpm)

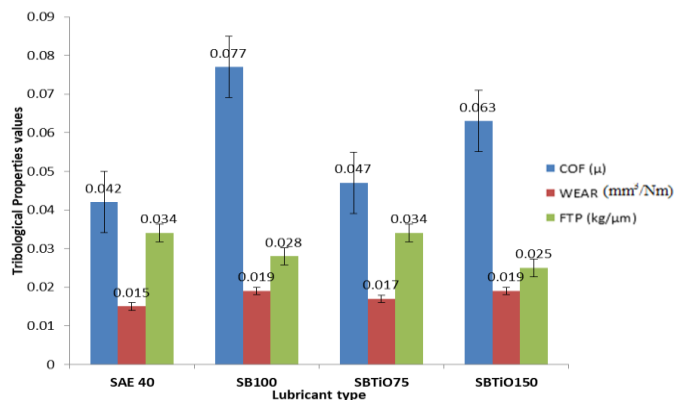


Figure 5. Effect of nanoparticle enrichment on coefficient of friction of the bio-lubricants (5 N, 200 rpm)

When the effect of percentage enrichment was compared for the lubricants, it was found that SBTiO75 had a lower friction coefficient than SBTiO150 at 150 rpm with a 2 N load, 200 rpm with a 5 N load, and 250 rpm with a 2 N load. However, SBTiO150 had a lower friction coefficient than

SBTiO75 when subjected to an 8 N load at two distinct speeds—150 rpm and 250 rpm. This demonstrates that the lubricant's anti-friction behavior was significantly influenced by the percentage or amount of enrichment and load. When the lubricant was first enriched with 0.75 weight percent of nanoparticles at 2 N and 5 N load, the friction coefficient significantly decreased; however, when the enrichment was increased to 1.50 weight percent, the friction coefficient rose in comparison to the 0.75 weight percent enrichment. These findings demonstrate that higher load requires high enrichment and lesser load demands low enrichment. These findings are consistent with studies published by Ali *et al.* [10], Shahnazar *et al.* [5], Ali and Xianjun [11], Jabal *et al.* [23], Patil *et al.* [9] and Alves *et al.* [12], which found that oils enriched with nanoparticles had lower friction coefficients than oils without nanoparticles. These results also compare favorably with the friction coefficient of conventional lubricant, SAE 40.

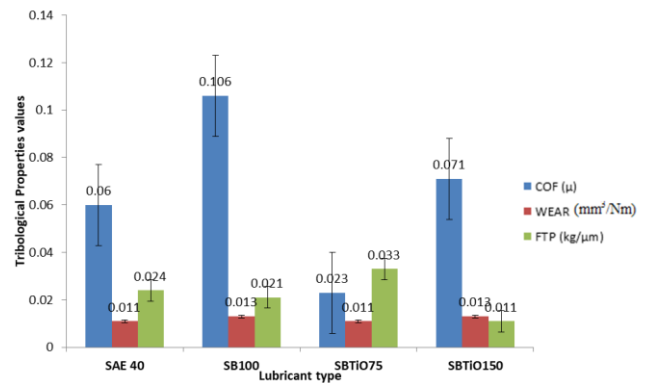


Figure 6. Effect of nanoparticle enrichment on coefficient of friction of the bio-lubricants (2 N, 200 rpm)

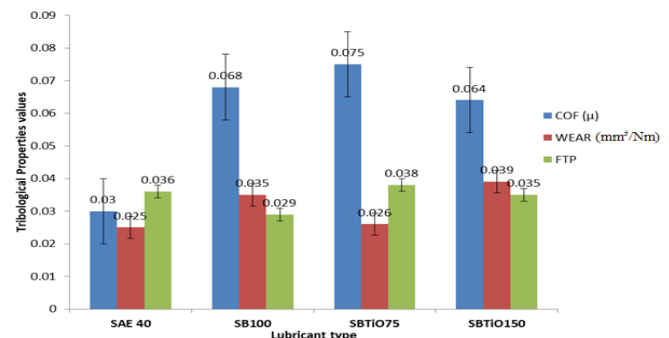


Figure 7. Effect of nanoparticle enrichment on coefficient of friction of the bio-lubricants (8 N, 250 rpm)

When the friction coefficient results were analysed, it was shown that the nanoparticle-enriched bio-lubricant show a significant improvement over the pure sandbox oil. The coefficient of friction reduces until it reaches a specific point where it begins to increase as the concentration of the nanoparticle in the bio-lubricant increases from 0.75 weight percent to 1.50 weight percent. According to Thottackkad *et al.* [26], this demonstrates that there is an optimal enrichment level at which the friction coefficient is at its lowest for a given weight and speed. As the lubricant's nanoparticle enrichment level is raised to the optimum level, the friction coefficient (COF) rises as well. Thottackkad *et al.* [29], Laad and Jatti [13], and Gulzar [4] have all observed similar trends of higher friction coefficient with greater concentration of nanoparticle towards the optimum concentration. It was found that a



uniform and steady dispersion of titanium oxide nanoparticles in the base oil significantly contributed to the improvement in the friction coefficient of the lubricants. According to Gulzar [4], nanoparticle concentration is important for the creation of stable dispersion, which leads to better friction behaviour. Stable dispersion contributed to the steady resistance to friction. The lubricant's homogeneous distribution of nanoparticles increased the likelihood of improving the rubbing surfaces. According to Ali *et al.* [10], the ability of the nanoparticle to convert pure sliding friction to rolling friction due to reduced interfacial interaction for frictional surfaces as well as the secondary effect of surface enhancement due to the surface polishing nature of the nanoparticle are additional reasons for the decrease in friction coefficient of the nanoparticle-enriched bio-lubricant.

When the concentration of nanoparticles is smaller, the lubricant's nanoparticles create a third body rolling effect between the sliding surfaces which reduces friction. Thottackkad *et al.* [26] and Ghaednia *et al.* [30] stated that this impact is significantly more noticeable at greater loads when the nanoparticles agglomerate and give the contacting area more supportive effort. Friction is raised as a result of the solid particle contact becoming more prevalent as the enrichment level is raised. According to Zulkifli *et al.* [31]'s report on the mechanical entrapment theory, nanoparticles in the lubricant are deposited at the contacting surfaces and form a layer that is later removed during further sliding, resulting in a decrease in friction. Additional causes include the formation of tribo-film on worn surfaces, which reduces the lubricant's ability to withstand shearing, and the effectiveness of fatty acids. Bahari [32] claims that the creation of the mono-molecular layer is also aided by the strong polarity of the fatty acids found in vegetable oils, which attracts the carboxyl group (COOH) to metallic surfaces.

### 3.3. Effect of nanoparticle enrichment on wear behaviour

Figures 3 through 7 further illustrate how the wear rate of the bio-lubricants is affected by the enrichment of nanoparticles. The findings demonstrated that whereas pure sandbox oil had poor anti-wear qualities at some concentrations, loads, and speeds, nanoparticle-enriched sandbox oil exhibited superior anti-wear properties at others. The findings demonstrate that, as long as the proportion of enrichment remained within the optimal level, nanoparticle enrichment increased the bio-lubricant's wear rate. When the percentage of enrichment exceeded the optimum concentration, the bio-lubricant's wear rate rose. Battez and Rodriguez [15] stated that this was caused by granule abrasions brought on by an overabundance of nanoparticles in the contact area. When the effect of percentage enrichment was compared to the bio-lubricants' wear rates, SBTiO75 was shown to have a lower wear rate than SBTiO150 at the loads (2, 5, and 8 N) and speeds (150, 200, and 250 rpm). As the concentration of the nanoparticle additions increases from 0.75 weight percent to 1.50 weight percent, the anti-wear advantages gradually diminish. At varying speeds of 150 rpm and 250 rpm, it was found that the wear rate for a 2 N load was less than that of an 8 N load. Additionally, it was noted that wear rate increased as load and speed increased.

Compared to speed, this rate of increase is more noticeable in relation to load. According to Mohan *et al.* [33], wear increases with load and speed beyond the deposition of nanoparticles created by tribo-film production. This further

demonstrates the significant influence that load and enrichment percentage or level had on the lubricant's anti-wear properties. Abere [25] suggests that the impact of the chemical makeup of the bio-lubricants on film formation could be the cause of the wear rate reduction resulting from this nanoparticle addition. The nanoparticle formed a stable and homogeneous solution in the lubricant, penetrated the contact area, and deposited on the mating surfaces to form a tribo-film through a deposition mechanism during lubrication.

The wear scar on the disc was altered by the addition of titanium oxide nanoparticle additive to the basic oil. A surface that is comparatively smooth, as seen in Figure 8 was produced after testing. Tao *et al.* [34] claim that the less severe disc wear is probably caused by the bio-lubricant's capacity to create a protective tribo-film. The nanoparticle's enhanced behaviour may be attributed to its minuscule size and consistent, stable dispersions, which allowed them to permeate the rubbing surfaces and fill in the worn scar. Numerous researchers have reported on this material filling technique using nanoparticles [4,20,27].

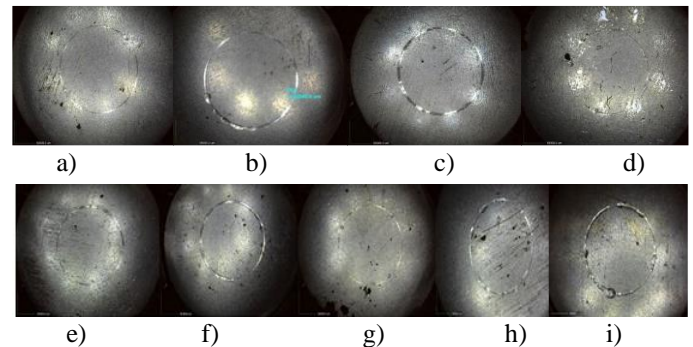


**Figure 8.** Typical optical micrographs of wear track on the discs; a) SB100 (2 N), b) SB100 (5 N), c) SB100 (8 N), d) SBTiO75 (2 N), e) SBTiO75 (5N), f) SBTiO75 (8N), g) SBTiO150 (2N), h) SBTiO150 (2N), and i) SBTiO75 (2N)

Some of the worn tracks in Figure 8 were so hardly noticeable. It shows that the nanoparticle was successful in forming a protective layer. This demonstrates enhanced wear resistance. According to Gulzar [4], this could be explained by the bio-lubricant's stable and uniform nanoparticle dispersion as well as the presence of fatty acid, which might aid in the lubricant layer's ability to maintain thickness and adhere well to the surface in order to lessen metal-to-metal contact. The creation of a protective layer and the significantly smaller size of the nanoparticles, which allowed them to more easily penetrate the contact zones, are other possible explanations for this anti-wear mechanism. Nanoparticles also deposit between interaction surfaces. The disc specimens' surfaces were analysed in order to comprehend the lubricant's lubricating mechanism. Figure 9 shows that the surface mending caused by the nanoparticle deposition on the disc surface was enhanced by an increasing concentration of nanoparticles. Figures 9(a), (b), and (c) demonstrate a larger tendency of wear tracks at low nanoparticle concentrations. However, as the concentration of nanoparticles increased, the tracks were filled in and the surface mended effect enhanced (Fig. 9(d), (e), and (f)).

Running-in or breaking-in wear mechanism was observed in figures 8 and 9. According to Bahari [32], in this mechanism the wear rate is often initially high, but as the surface become smoother and the more prominent asperities are flattened or lost,

the wear rate falls. After a suitable time, the full-service conditions can be applied without any sudden increase in wear rate and the steady low wear rate is maintained for the operational life of the component. It is evident from the analysis of wear and friction that when applied at the ball-disc interface, titanium oxide nanoparticle-enriched bio-lubricant exhibits superior tribological capabilities than the base oil lubricant. These findings were in line with earlier studies by Laad and Jatti [13], who found that the addition of titanium oxide (TiO<sub>2</sub>) nanoparticle improved the tribological properties of lubricating oil, as well as studies by Ali and Xianjun [11] who found that base oil containing nanoparticle additives had exceptional anti-friction and anti-wear qualities.

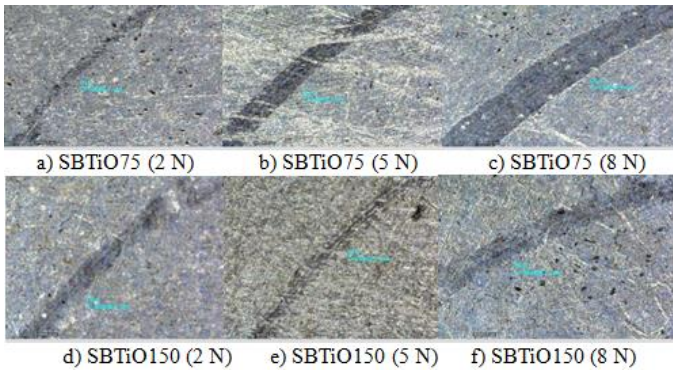


**Figure 9.** SEM micrographs of disc specimens tested with the formulated bio-lubricants

**3.4. Effect on flash temperature parameter (FTP)**

A value known as the flash temperature parameter is used to indicate the critical temperature below which a lubricant can form a film and endure without breaking down. It is a single number that is frequently used to convey the censorious flash temperatures that occur when lubricants totally fail in specific circumstances. The bonding between the lubrication molecules was broken at that point, according to Syahrullail *et al.* [35], and the surface began to starve of lubricant. The effect of nanoparticle enrichment on the bio-lubricant's flash temperature parameter is displayed in Figs. 3–7. Because of the increased frictional force caused by an increase in load, the flash temperature parameter generally rose when the load was increased from 2 N to 8 N. Similar patterns were noted by Singh [36] for the *Jatropha* bio-lubricant, showing an increase in the flash temperature parameter from 50 N to 150 N of load.

The results implies that the lubricant could keep the lubrication layer intact for a longer amount of time. This is because the bio-lubricant performs better at higher FTP values. As a result, it is noted that, in comparison to base oil, the nanoparticle enrichment increased lubricity overall performance and decreased the likelihood of lubricant film breakup.

**3.5. Optimum enrichment level**

The projected operating conditions required to achieve the lowest coefficient of friction and wear rate as well as the maximum flash temperature parameter were, according to the optimization result in Figure 10, a load of 8 N, a speed of 199.4949 rpm, and a concentration of 0.7121 weight percent of TiO<sub>2</sub> nanoparticles. At the optimum setting, the wear rate and coefficient of friction has values of 0.0171 and 0.0490

(mm<sup>3</sup>/Nm), respectively, and the flash temperature parameter had value of 0.0381.

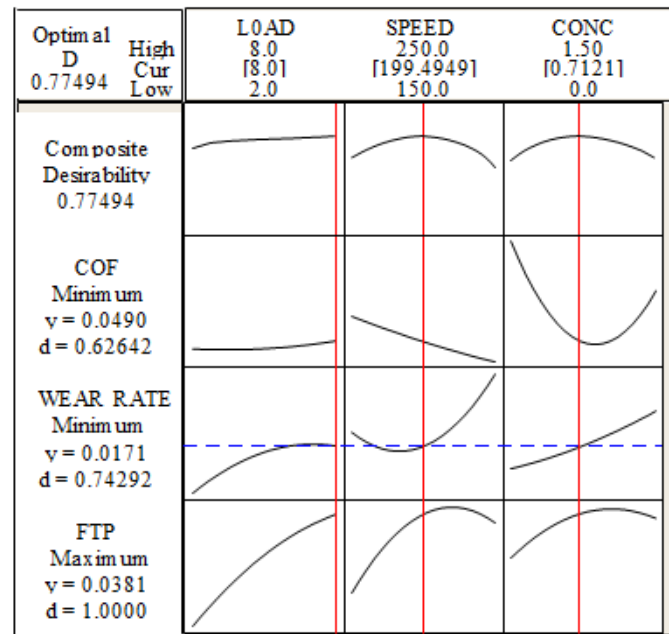


**Figure 10.** Optimization results for titanium oxide nanoparticle-enriched bio-lubricant

**4. Conclusions**

The bio-lubricant's tribological behaviour revealed that the titanium oxide nanoparticle enhanced the flash temperature parameter, decreased friction and wear rate because the particles were deposited on the worn surfaces and between the rubbing surfaces, and ultimately decreased the shearing resistance. When SBTiO75 and SBTiO150 were compared to pure sandbox oil at 150 rpm and 2 N load, the friction coefficients of the two bio-lubricants were reduced by 10.81% and 4.05%, respectively. Additionally, at 150 rpm with an 8 N load, the friction coefficient decreased by 14.80% for SBTiO75 and 36.40% for SBTiO150. At 200 rpm with a 5 N load, the reductions were 38.96% and 18.18% for SBTiO75 and SBTiO150, respectively, and at 250 rpm with a 2 N load, the reductions were 78.30% and 33.02% for SBTiO75 and SBTiO150, respectively. Friction coefficient increased by 9.33% for SBTiO75 at 250 rpm with an 8 N load, but decreased by 5.88% for SBTiO150. These findings demonstrated that sandbox oil loaded with nanoparticles provides substantially lower friction coefficients than sandbox oil without nanoparticles. The nanoparticle created a stable and homogeneous solution in the lubricant, penetrated the contact area, and deposited on the mating surfaces to form a tribo-film through the deposition mechanism during lubrication. In order to enhance the bio-lubricant's tribological qualities, titanium oxide nanoparticles can be employed as an anti-friction and anti-wear additive.

**Author contributions**

Caleb Abiodun Popoola: conceptualization, methodology, validation, formal analysis, investigation, resources, data maintenance, writing-creating the initial design, visualization, monitoring and management, funding procurement

Okwuchi Smith Onyekwere: methodology, software, validation, resources, data maintenance, writing-reviewing and editing, funding procurement

## References

- Mehic, S.H., Additives In Lubricant: Types and Chemical Composition of Lubricant Additives, Chemicals office of the Republic of Slovenia. **2017**
- Jackson, R.P., Engineering Tribology, PDH Online, **2012**
- Khasbage, S., Patil, V., and Dhande, D., Performance of Jatropa Biolubricant for Hydrodynamic Journal Bearing Lubrication. International Research Journal of Engineering and Technology, **2016**, 03(07): 627 – 632
- Gulzar, M., Tribological Study of Nanoparticles Enriched Bio-Based Lubricants for Engine Piston Ring–Cylinder Interaction, Unpublished Phd Thesis, Faculty of Engineering, University of Malaya, Kuala Lumpur, **2017**
- Shahnazar, S., Bagheri, S., and Abd Hamid, S.B., Enhancing Lubricant Properties by Nanoparticle Additives. International Journal of Hydrogen Energy, **2016**, 41: 3153 – 3170
- Chandan, S., Ganipantapalli, S.S., Harish, B.K., Srinivas, M.S., and Smitha, B.S., Experimental Study on the Use of Neem Oil as Lubricant in IC Engine, International Research Journal of Engineering and Technology, **2017**, 04(08): 1087 – 1092
- Naik, A.U. and Galhe, D.S., Review on Vegetable Oil as Bio-Lubricant, Int. Journal for Scientific Research and Development, **2016**, 5(10):587 – 589
- Hassan, M., Ani, F.N., and Syahrullail, S., Tribological Performance of Refined, Bleached and Deodorised Palm Olein Blends Bio-Lubricants, Journal of Oil Palm Research, **2016**, 28(4): 510 – 519
- Patil, S.J., Patil, D.P., Shrotri, A.P., and Patil, V.P., A Review on Effect of Addition of Nanoparticles on Tribological Properties of Lubricants, International Journal of Mechanical Engineering and Technology (IJMET), **2014**, 5(11): 120 – 129
- Ali, M.K.A., Xianjun, H., Mai, L., Bicheng, C., Turkson, R.F and Qingping, C., Reducing Frictional Power Losses and Improving the Scuffing Resistance in Automotive Engines Using Hybrid Nanomaterials as Nano-Lubricant Additives, Wear, **2016**, 364-365: 270 – 281
- Ali, M.K.A. and Xianjun, H., Improving the Tribological Behaviour of internal Combustion Engines Via the Addition of Nanoparticles to Engine Oils, Nanotechnology Rev, **2015**, 4(4): 347 – 358
- Alves, S.M., Barros, B.S., Trajano, M.F., Ribeiro, K.S.B. and Moura, E., Tribological Behaviour of Vegetable Oil-Based Lubricants with Nanoparticles of Oxides in Boundary Lubrication Conditions, Tribology International, **2013**, 65: 28 – 36
- Laad, M. and Jatti, V.K.S., Titanium Oxide Nanoparticles as Additives In Engine Oil, Journal of King Saud University – Engineering Sciences, **2018**, 30: 116 – 112
- Le, V.N. and Lin, J., Tribological Properties of Aluminum Nanoparticles as Additives in an Aqueous Glycerol Solution, Applied Sciences, **2017**, 7(80): 1 – 15
- Battez, A.H., and Rodriguez, R.G., Tribological Properties of the Lubricant Containing Titanium Dioxide Nanoparticles as an Additive, Lubricants, **2016**, 4(2): 1–17
- Afzal, A., Kumar, M., and Ramis, M.K., Investigation of Physicochemical and Tribological Properties of TiO<sub>2</sub> Nano-Lubricant Oil of Different Concentrations. TRIBOLOGIA – Finnish Journal of Tribology, **2017**, 35(3):6 – 15
- Binu, K.G., Shenoy, B.S., Rao, D.S. and Pai, R., A Variable Viscosity Approach for the Evaluation of Load Carrying Capacity of Oil Lubricated Journal Bearing with TiO<sub>2</sub> Nanoparticles as Lubricant Additives, Proceedings of 3<sup>rd</sup> International Conference on Materials Processing and Characterisation (ICMPC), **2014**, 6(2014):1051– 1067
- Akintunde, S.B., Obayopo, S.O., Adekunle, A.S., Combustion and emission study of sandbox seed oil biodiesel performance in a compression ignition (CI) engine, Energy Reports, **2021**, 7: 3869–3876
- Birleanu, C., Pustan, M., Cioaza, M., Molea, A., Papa, F., Effect of TiO<sub>2</sub> nanoparticle on the tribological properties of lubricating oil: an experimental investigation, Scientific Reports, **2022**, 12: 5201
- Samidin, S, Salih, N., and Salimon, J., Synthesis and Characterization of Trimethylolpropane Based Esters as Green Biolubricant Basestock, Biointerface research in applied chemistry, 2021, 11(5): 13638 – 13651
- Mohamed, M., Ndyaye, S., Talla, K., Mbow, C., and Beye, A., Enhanced Oil Recovery by Injecting Oleic Acid as a Surfactant into the Porous Medium, *Open Journal of Fluid Dynamics*, **2020**, 10: 82-94
- Jimoh, A. A., Otori, A. A., Azeez, S. O., Adebayo, Z. F., Abdulsalam, Z. A., and Mathew, J.T., Optimization of biodiesel production from parinarium macrophyllum seed oil using potassium hydroxide loaded on calcium oxide catalyst, *Lapai Journal of Science and Technology*, **2022**, 8(1): 56-74
- ISO 5509., Animal and Vegetable Fats and Oils in: Preparation of Methyl Esters of Fatty Acids. 2<sup>nd</sup> Ed., International Organization for Standardization, Geneva, Switzerland, **2000**
- Bilal, S., Mohammed-Dabo, I.A., Nuhu, M., Kasim, S.A., Almustapha, I.H. and Yamusa, Y.A., Production of Biolubricant from Jatropa Curcas Seed Oil, Journal of Chemical Engineering and Materials Science, **2013**, 4(6): 72 – 79
- Abere, J.O., Improved Performance of Bio-Lubricant by Nanoparticles Additives, Unpublished Phd Thesis, Department of Mechanical Engineering, University of Sheffield, **2017**
- Thottackkad, M.V., Rajendrakumar, P.K., and Prabhakaran, N.K., Tribological Analysis of Surfactant Modified Nanolubricants Containing CeO<sub>2</sub> Nanoparticles, Tribology, **2014**, 8(3):125 – 130
- Umaru, M., Aris, M.I., Munnir, S.M., Aliyu, A.M., Aberuagba, F., and Isaac, A.J., Statistical Optimization of Biolubricant Production from Jatropa Curcas Oil Using Trimethylolpropane ss a Polyol, Proceedings of the World Congress on Engineering and Computer Science, October 19 – 21, **2016**
- Jabal, M.H., Ani, F.N., and Syahrullail, S., The Tribological Characteristic of the Blends of RBD Palm Olein with Mineral Oil Using Four-Ball Tribotester, Jurnal Tecknologi, **2014**, 69(6): 11 – 14
- Thottackkad, M.V., Perikinalil, R.K., and Kumarapillai, P.N., Experimental Evaluation on the Tribological Properties of Coconut Oil by the Addition of CuO Nanoparticles. International Journal of Precision Engineering, and Manufacturing, **2012**, 13(1):111 – 116

30. Ghaednia, H., Jackson, R.L., and Khodadadi, J.M., Experimental Analysis of Stable CuO Nanoparticle Enhanced Lubricants, *Journal of Experimental Nanoscience*, **2015**, 10(1): 1–18
31. Zulkifli, N.W.M., Kalam, M.A., Masjuki, H.H. and Yunus, R., Experimental Analysis of Tribological Properties of Biolubricant with Nanoparticle Additive, *Procedia Engineering*, **2013**, 68: 152 – 157
32. Bahari, A., Investigation Into Tribological Performance of Vegetable Oils as Biolubricants at Severe Contact Conditions. Unpublished Phd Thesis, Department of Mechanical Engineering, University of Sheffield, **2017**
33. Mohan, N., Sharma, M., Singh, R., and Kumar, N., Tribological Properties of Automotive SAE 20W-40 Containing Nano-Al<sub>2</sub>O<sub>3</sub> Particles. SAE International, SAE Technical Paper, **2014**, 01-2781
34. Tao, C., Wang, B., Barber, G., Schall, J., Zou, Q., and Wang, J., Tribological Mechanism of Friction and Wear Reduction Using Oil-Based ZnO Nanofluid Applied on Brass, *European Scientific Journal*, **2019**, 15(3): 223 – 238
35. Syahrullail, S., Wira, J.Y., Wan Nik, W.B., and Fawwaz, W.N., Friction Characteristics of RBD Palm Olein Using Four-Ball Tribotester, *Applied Mechanics and Materials*, **2013**, 315: 936 – 940
36. Singh, Y., Tribological Behaviour as Lubricant Additive and Physiochemical Characterization of Jatropha Oil Blends, *Friction*, **2015**, 3(4): 320 – 332

# Comparison of NACA 0012 and KFm-4 wing profiles for high subsonic speed unmanned aerial vehicles

Muktedir Gözüm<sup>\*1</sup> and Cevat Özarpa<sup>2</sup>

<sup>1</sup>Ankara Medipol University Health Services Vocational School of Higher Education, Biomedical Device Technology Department, Ankara, Türkiye

<sup>2</sup>Ankara Medipol University Engineering Faculty Biomedical Engineering Department, Ankara, Türkiye

## Article Info

### Article history:

Received 08.12.2023

Revised: 22.07.2024

Accepted: 23.10.2024

Published Online: 23.12.2024

### Keywords:

Kline-Fogleman

NACA 0012

High speed UAV

Symmetrical airfoil

CFD analysis

## Abstract

KFm airfoil, attracts attention among radio-controlled aircraft enthusiasts due to its simplicity of construction. It was not preferred in manned aircraft due to its poor lift-to-drag ratio performance in wind tunnel tests. In this article, by comparing it with the NACA0012 profile, which is generally preferred at high subsonic speeds, the consequences of choosing the KFm-4 wing profile over the NACA0012 profile due to its ease of production, and what advantages and disadvantages it has. The comparison; While increasing the speed of high-speed unmanned aerial vehicles, it will be important to fly more stable, have better maneuverability, reduce the drag force and delay separation. The calculations were obtained by performing computational fluid dynamics analysis in 2 dimensions. Analysis was conducted under conditions of a low Reynolds number, with a consistent velocity at Mach 0.6 and a zero-degree angle of attack. To validate the precision of the outcomes, a series of tests were executed, involving variations in grid size or node configurations. With the increase in the number of nodes, the lift coefficient exhibited a rising trend; however, upon reaching 305100 nodes, further increase in nodes did not lead to any significant change in the lift coefficient. As a result, a lift coefficient value of 0.1010 was obtained for the NACA 0012 profile, while a lift coefficient value of 0.0720 was obtained for the KFm-4 profile. Thus, it was concluded that it would be more appropriate to use the NACA 0012 profile in high-speed unmanned aerial vehicles.

## 1. Introduction

Unmanned aerial vehicles are very important today, both civilian and military, especially in missions where the risk of losing an aircraft is high. In this case, the aircraft must aerodynamically perform its duty stably at both low and high subsonic speeds ( $<980 \text{ kmh}=609 \text{ mph}=0.8 \text{ Mach}$ ). For this, the wing profile must be selected correctly so that the aircraft can fly stably even at high angles of attack, so that the possibility of stalling is minimized [1].

It is possible to improve the aerodynamics of an aircraft by trying various types of wing profiles. Richard Kline and Floyd Fogleman designed several staggered airfoils designed solely for paper airplanes in 1960. Richard Kline's goal was to create a paper airplane that could fly long distances and automatically increase altitude by countering wind resistance and turbulence. Thus, he achieved the stepped wing profile. Kline Fogleman profile structure can also be called stepped wing profile. Stepped wing profiles enable the creation of a vortex-shaped airflow by preventing the separation of the airflow and maintaining the airflow. The airflow behind the step is separated from the airfoil [1]. After making preliminary examinations and models, the designers submitted their patents to the patent office [2]. The NACA 0012 airfoil is a symmetrical wing profile without any humps, commonly employed in diverse aviation applications. Similar to the KFm-4 profile, it exhibits excellent performance at low Mach numbers. [3].

In the 21st century, the KF airfoil has seen renewed interest among radio-controlled aircraft enthusiasts due to its simplicity

of construction, but it has not been adopted for full-size aircraft capable of carrying pilots, passengers or other significant payloads. Poor lift-to-drag ratio performance in wind tunnel tests means that to date the KF airfoil has not been used on any full-size aircraft. However, the KF airfoil and its derivative 'staggered' airfoils have gained a following in recent years in the world of radio-controlled model airplanes made of foam. Their low Reynolds numbers allow staggered airfoils to generate a significant amount of lift for the friction incurred, which has made them increasingly popular with RC enthusiasts. This paper investigates the advantages and disadvantages of choosing the KFm-4 airfoil over the NACA0012 airfoil due to its ease of manufacture, in comparison to the NACA0012 airfoil, which is generally preferred for high subsonic speeds.

In this study,  $k-\omega$  SST turbulence model was used to simulate the problem using CFD analysis [4]. A comparison was made in terms of lift and drag coefficients of both airfoils at 0.6 Mach speed. Understanding low Reynolds number aerodynamics holds paramount importance in both military and civilian sectors. Consequently, this investigation places particular emphasis on examining the separation phenomena at the trailing edge of symmetrical airfoils operating within the constraints of low Reynolds numbers. [4].

## 2. Materials and Methods

### 2.1 Force Equations

Drag  $F_D$  and Lift  $F_L$  are basically expressed in two terms and these are dimensionless coefficients [5]:

$$C_D = \frac{F_D}{\frac{1}{2}\rho_\infty v_\infty^2 A} \quad (1)$$

$$C_L = \frac{F_L}{\frac{1}{2}\rho_\infty v_\infty^2 A} \quad (2)$$

The occurrence of lift in an airfoil depends on several factors such as air density, airflow velocity, angle of attack and total area of the airfoil. In the equation above,  $C_D$  and  $C_L$  are the drag and lift coefficients,  $F_D$  and  $F_L$  are the drag and lift forces,  $\rho_\infty$  is the density of the air,  $v_\infty$  is the cruise speed and  $A$  is the wing area.

## 2.2 Other Equations

Other equations used are listed here:

Continuity equation [5]:

$$\nabla \cdot \vec{v} = 0 \quad (3)$$

Conservation of momentum [5]:

$$\frac{\partial \vec{v}}{\partial t} + \vec{v} \cdot \nabla \vec{v} = -\frac{1}{\rho} \nabla p + \frac{\mu}{\rho_0} \nabla^2 \vec{v} + \vec{g} - \beta(T - T_0) \vec{g} \quad (4)$$

$\beta$  is the coefficient of thermal expansion. Conservation of Energy [5]:

$$\frac{\partial T}{\partial t} + \vec{v} \cdot \nabla T = \alpha \nabla^2 T \quad (5)$$

## 2.3 Turbulence Model

In the setup section, the solver type was selected as density based for compressible flow [5]. Air speed is taken into account as 0.6 Mach. The k- $\omega$  SST turbulence model was used to simulate the problem [6].

The specific dissipation rate of kinetic energy is solved by k- $\omega$  turbulent models. This model requires computers with higher memory for calculation. It is quite sensitive and difficult to converge. The equations for the models are below [6].

k- $\epsilon$  turbulence model equation [6]:

$$\frac{\partial}{\partial t}(\rho k) + \frac{\partial}{\partial x_i}(\rho k u_i) = \frac{\partial}{\partial x_j} \left[ \left( \mu + \frac{\mu_t}{\sigma_k} \right) \frac{\partial k}{\partial x_j} \right] + G_k + G_b - \rho \epsilon - Y_k + S_k \quad (6)$$

$$\frac{\partial}{\partial t}(\rho \epsilon) + \frac{\partial}{\partial x_i}(\rho \epsilon u_i) = \frac{\partial}{\partial x_j} \left[ \left( \mu + \frac{\mu_t}{\sigma_\epsilon} \right) \frac{\partial \epsilon}{\partial x_j} \right] + C_{1\epsilon} \frac{\epsilon}{k} (G_k + C_{3\epsilon} G_b) - C_{2\epsilon} \rho \frac{\epsilon^2}{k} + S_\epsilon \quad (7)$$

k- $\omega$  turbulence model equation [6]:

$$\frac{\partial}{\partial t}(\rho k) + \frac{\partial}{\partial x}(\rho k u_i) - \frac{\partial}{\partial x_i} \left( \Gamma_k \frac{\partial k}{\partial x_i} \right) + G_k - Y_k + S_k \quad (8)$$

$$\frac{\partial}{\partial t}(\rho \omega) + \frac{\partial}{\partial x}(\rho \omega u_i) = \frac{\partial}{\partial x_i} \left( \Gamma_\omega \frac{\partial \omega}{\partial x_i} \right) + G_\omega - Y_\omega + S_\omega \quad (9)$$

Explanations of the symbols used in the formulas are; ( $G_k$ : Production of turbulent kinetic energy due to mean velocity gradients,  $G_b$ : Turbulent kinetic energy production due to lift force,  $G_\omega$ :  $\omega$  represents the derivation,  $Y_M$ : Undulating expansion in compressible turbulence towards overall dissipation velocity,  $Y_k$  and  $Y_\omega$ : Dispersion of  $k$  and  $\omega$  due to

turbulence,  $\Gamma_k$  and  $\Gamma_\omega$ : Effective diffusion of  $k$  and  $\omega$  respectively,  $S_k$  and  $S_\omega$ : User-defined source terms).

## 2.4 Model, Mesh and Boundary Conditions

The calculation model and research methodology were created using ANSYS Fluent 19 software [7]. Here, a flow analysis was performed around NACA 0012 and KFM-4 airfoils with the following initial parameters (Table 1). The calculation domain is divided into finite volumes by the calculation model, as shown in Figures 1, 2 and 5. The mesh structure is concentrated in computational areas where there are large changes in the calculated parameters.

**Table 1.** Calculation conditions

Density (Air)	1.225 kg/m <sup>3</sup>
Wind speed	204.17 m/s (0.6 Mach)
Angle of Attack	0 (Degrees)
Chord Length	1.0 m
Temperature	293 K
Reference Pressure	101325 Pa

While boundary conditions are generally used up to 20c in the geometry section before making the C type mesh, [4], [8], [9] in this study it was drawn taking into account the 12.5 c (c: chord) dimension.

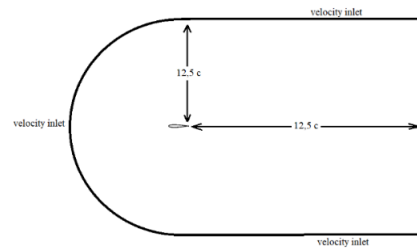


**Figure 1.** The computational domain around the airfoils

Chord length is taken into account as 1m. The inlet and walls are called fluid inlets, the exit part is called fluid outlet, and the wing boundaries are called airfoil [10].

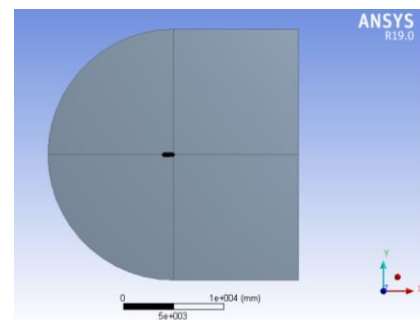


**Figure 2.** The computational domain around the airfoils in ANSYS for NACA 0012 and KFM-4

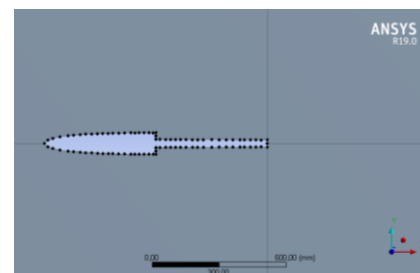


**Figure 3.** KFM-4 Airfoil

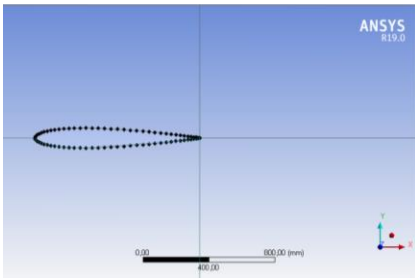


Figure 4. NACA 0012 Airfoil

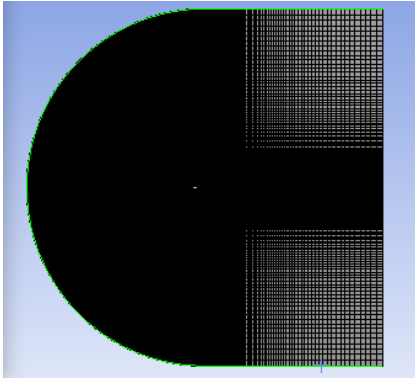


Figure 5. Boundary condition and mesh structure for NACA 0012 (mapped mesh)

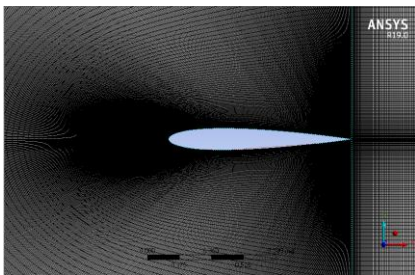


Figure 6. Mesh structure (mapped mesh)

Airfoil data on Ansys is shown as a drawing in Figures 3 and 4.

Table 2. Ansys mesh settings for NACA0012 and KfM-4 airfoils

Nodes	305100	
Elements	303750	
Mesh Metric	None	
Suppressed	No	
Type	Number of Divisions	
Number of Divisions	450	225
Mapped Mesh	Yes	
Method	Quadrilaterals	
Constrain Boundary	No	
Size Function	Uniform	
Behavior	Hard	
Bias Type	-----	
Bias Option	Bias Factor	
Bias Factor	150.0	

In the Table 2; Meshing process of KfM-4 Profile, 303750 meshes were cast (Number of elements). In Figure 6, the "Mapped Mesh" structure is shown on Ansys Fluent.

The freestream velocity is 204.17 m/s,  
Density is  $1.225 \text{ kg/m}^3$

Dynamic viscosity is  $1.82\text{e-}5 \text{ kg/ms}$ ,  
Boundary layer length is 1 m,  
Y+ Value is 1,  
Reynold number is  $1.1\text{e+}6$ ,  
Estimated Wall distance is  $2.0\text{e-}5$ .

3. Results and Discussion

As an initial condition, the airflow velocity is assumed to be equal to 204.17 m/s (0.6 Mach). The results of the numerical investigations are presented below. The distributions of the velocity field around the examined airfoil models and the pressure values for these models are shown (NACA 0012 and KfM-4). All figures are presented for 0-degree angle of attack. In Figure 7, the maximum dynamic pressure is shown as 83768 Pascal.

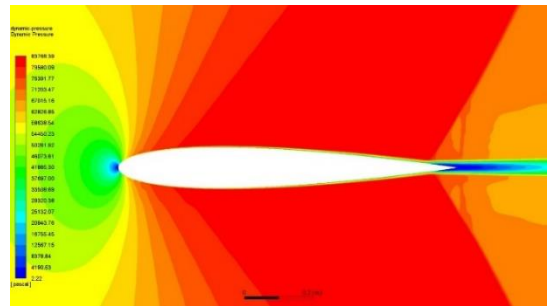


Figure 7. NACA 0012 dynamic pressure distribution (Pa)

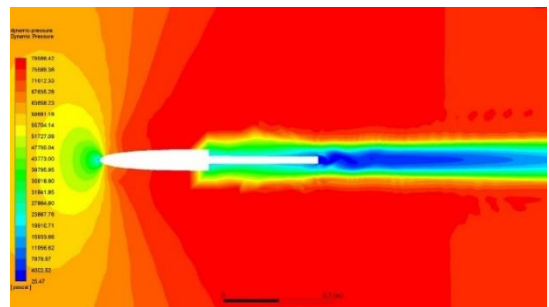


Figure 8. KfM-4 Dynamic pressure distribution (Pa)

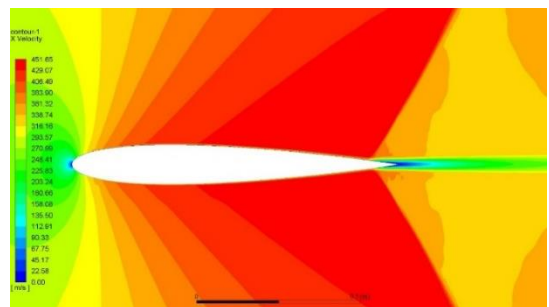


Figure 9. NACA 0012 Speed distribution (m/s)

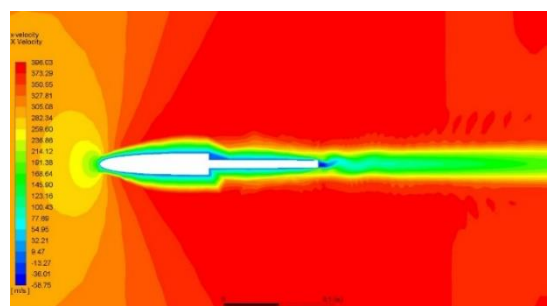


Figure 10. KfM-4 Speed distribution (m/s)

In Figure 8, the maximum dynamic pressure is shown as 79566.42 Pa. From the shapes of the pressure lines, it can be seen that the leading edge has lower pressure, while the upper and lower surfaces have higher pressure. This shows that the surfaces with high pressure try to lift the fuselage and therefore increase the lift coefficient, but it should not be forgotten that the analysis was carried out at 0-degree angle of attack and on a symmetrical airfoil. As can be seen from the figure, the pressure contours are distributed symmetrically and positioned to fully meet the wind (at 0 degrees). In the given form of pressure contours it is shown that there is a green color on the leading edge, on the lower and upper side the color is red, the red color indicates a higher-pressure value and the green color indicates a lower value.

As the angle of attack increases, the lift coefficient also increases, but when the angle of attack reaches 16 degrees, a stall situation will occur [6, 11].

In Figure 9, the maximum speed of the air flowing on the surface is shown as 451.65 m/s. The interpretation of Figure 9 is given in the conclusions section.

In Figure 10, the maximum speed of the air flowing on the surface is shown as 396.03 m/s. The interpretation of Figure 10 is given in the conclusions section.

When we look at the speed distributions above, we see that the highest speeds are reached as we move from the wing surface towards the tips. As you move towards the wing tips, the boundary layer becomes thinner, resulting in less drag and a higher speed at the wing tips. When we look at the speed distributions above, we see that the highest speeds are reached as we move from the wing surface towards the tips.

**Table 3.** Forces acting on NACA 0012 Profile

Lift	7165.5	N
Drag	-373.4	N
$C_l$	0.1010	
$C_d$	-0.0052	

**Table 4.** Forces acting on KFm-4 Profile

Lift	5109.40	N
Drag	-729.01	N
$C_l$	0.0720	
$C_d$	-0.0102	

The table 3 and 4 shows the force and coefficient values calculated as a result of the analysis.  $C_l$  refers to the lift coefficient, and  $C_d$  refers to the drag coefficient. As can be seen from the table, at 0-degree angle, the NACA 0012 airfoil is superior to the KFm-4 profile in terms of lift and drag forces.

#### 4. Conclusions

Aerodynamic comparison was made between the values assumed above and the results of modeling the flow in 2D. Special attention was paid to determine the 2D pressure distribution and velocity for the model with the initial parameters set. Based on the lift and drag forces in Table 3 and Table 4, it was concluded that the NACA 0012 airfoil was superior for 0 degrees.

In High Subsonic Speed Unmanned Aerial Vehicles, the KFm-4 airfoil can be used, but the NACA0012 airfoil is more suitable, especially when high subsonic speed is required. As a result of the analysis, it was seen that it is not suitable for use in

large-sized and man-carrying aircraft compared to the NACA0012 profile.

However, KFm airfoils can increase the level of flight safety by reversing accidents that occur by exceeding critical angles of attack (stalling at higher angles). If these airfoils are designed in hybrid with NACA symmetric airfoils, they can provide a significant advantage. In a more detailed analysis, it is possible to formulate the following results:

- At high angles of attack, vortex formations can be seen on the upper surface of the airfoil.
- The results obtained in the analysis are based on numerical errors, the applicability of the computational models and the limitations of the mesh. For this reason, experimental verification of the numerical results should be performed on platforms such as wind tunnels.

#### Acknowledgments

This article was supported by Karabuk University Scientific Research Projects Coordination Office with the project number KBÜBAP-22-YL-071. I would like to thank Karabuk University Scientific Research Projects Coordination Office for its support. I would like to express my endless gratitude to Dr. Cevat ÖZARPA, who showed interest and support in the planning, research, execution and formation of this thesis study and made a great contribution with his guidance and information.

#### Author contributions

Muktedir Gözüm: Research, Methodology, Design, Analysis and writing the original draft.

Cevat Özarpa: Formal analysis, Funding acquisition, Project management, Validation, Review and editing of the article.

#### References

1. Kowaleczko, G., Stryczniewicz, W., Szczepaniak, R., Bąbel, R., and Grzywacz, A., The effect of using the Kline-Fogleman modification upon the coefficient characteristics of aerodynamic forces in the airfoil, *Journal of KONES Powertrain and Transport*, **2018**, 25(2): 349–356
2. Fogleman, F., Kline, R., Airfoil for aircraft having improved lift generating device, US patent No. US4046338A, United States Patent and Trademark Office, **1977**
3. Fincham, J.H., and Friswell, M.I., Aerodynamic optimisation of a camber morphing aerofoil, *Aerosp. Technol.*, **2015**, 43, 245–255
4. Lei, J., Guo, F., and Huang, C., Numerical study of separation on the trailing edge of a symmetrical airfoil at a low Reynolds number, *Chinese J. Aeronaut.*, **2013**, 26(4): 918–925,
5. Kabir, M.A., Islam, M., Akib, Y.M., and Hafiz, A., Comparison between two Kline–Fogleman modified (KFm) based stepped airfoils for better aerodynamic performance, *International Conference on Innovation in Engineering and Technology*, Dhaka, Bangladesh, **2019**
6. Saraf, A.K., Singh, M.P., Chouhan T.J., Aerodynamic analysis of NACA 0012 airfoil using CFD, *International Journal of Mechanical and Production Engineering*, **2017**, 5(12): 21-25
7. ANSYS Inc., ANSYS Fluent Tutorial Guide 18, **2018**, 229-265
8. Z., Li, P., Zhang, T., Pan, and Q., Li, Study on effects of thickness on airfoil-stall at low Reynolds numbers by cusp-



- catastrophic model based on GA (W) -1 airfoil, Chinese J. Aeronaut., **2020**, 33(5): 1444–1453
9. Zhen, T.K., Zubair, M., and Ahmad, K.A., Experimental and Numerical Investigation of the Effects of Passive Vortex Generators on Aludra UAV Performance, Chinese J. Aeronaut., 2011, 24(5): 577–583
  10. Soğukpınar, H., Uçak Kanatlarında En İdeal Hücüm Açısını Bulmak İçin 4 Rakamli Naca 00xx Kanat Profillerinin Nümerik Analizi, Uludağ Üniversitesi Mühendislik Fakültesi Dergisi, **2017**, 22(1), 169-178
  11. Simons, M., Model Aircraft Aerodynamics, 4 th., Adelaide: Argus Books, **1994**

# Effect of deep cryogenic treatment on microstructural and mechanical properties of high-performance CPOH and WP7V tool steels

Volkan Karakurt<sup>\*1</sup>, Feyzanur Öztürk<sup>1</sup>, Talip Çitrak<sup>1</sup>, Gamze Nur Gözüak<sup>1</sup>, Orçun Zığındere<sup>1</sup>

<sup>1</sup>Sağlam Metal San.ve Tic. A.Ş., R&D Department, Çayırova, Kocaeli, Türkiye

## Article Info

### Article history:

Received 11.06.2024

Revised: 24.12.2024

Accepted: 26.12.2024

Published Online: 30.12.2024

### Keywords:

Tool steel

CPOH

WP7V

Deep cryogenic treatment

Wear test

## Abstract

In recent years, deep cryogenic treatment (DCT) has been applied to steel materials as an additional heat treatment to improve various material properties such as wear resistance, impact resistance and hardness. In this study, the mechanical properties of CPOH cold work tool steel with high wear and impact resistance and Dörrenberg Edelstahl patented WP7V cold work tool steel used in applications requiring high hardness were improved by deep cryogenic heat treatment. The materials subjected to deep cryogenic heat treatment were subjected to a conventional austenitizing and quenching process. After quenching, the materials were subjected to deep cryogenic treatment and then tempered. The microstructure, hardness, wear and impact properties of cryogenically heat treated materials were investigated in comparison with those obtained after conventional heat treatment. It was found that the wear rate of CPOH steel increased by 76.22% and WP7V steel increased by 88.95% with deep cryogenic heat treatment. At the same time, as a result of microstructure examinations, it was determined that the amount of residual austenite decreased and finer secondary carbide distribution was realized. It was found that deep cryogenic heat treatment of tool steels in addition to conventional heat treatment can improve material performance and provide high performance tool steels required by the industry.

## 1. Introduction

CPOH steel material; It is a new generation cold work tool steel that combines high wear and impact resistance with 8% chromium and 2.5% molybdenum. This tool steel is used in bolt rolling rollers and combs, cold rolling mill rollers, precision cutting dies for sheet metal up to 10 mm. WP7V tool steel is a special tool steel with high chromium, molybdenum and vanadium alloy patented by Dörrenberg Edelstahl. It is used in molds subjected to high stresses due to its high hardness depth, engraving molds with flat shapes such as forks and spoons, cold or hot cutting molds or punches, sheet metal cutting molds of 7 mm and above [1].

In hard various applications such as precision cutting, stamping and punching applications, tool steels are subjected to high loads, contact pressures, contact temperatures and conditions that cause wear of the materials. Tool steels exhibit mechanical properties such as high hardness, wear resistance and impact strength due to their tempered martensite microstructure and carbides in their structure. In order to further improve these properties under harsh conditions of use, deep cryogenic treatment has attracted much attention in recent years [2].

In the last decade, the application of cryogenic heat treatment to metallic materials has led to significant advances in various industries, such as medicine, aerospace, robotics, materials science, nanotechnology and mining. This technique, 19. it evolved over the century from the first attempts of James Dewar and Karol Olszewski to process materials at low temperatures using liquefied gases (nitrogen and hydrogen). Scientific foundations of cryogenic heat treatment, 20. it was further reinforced by the first observations made by NASA in the

middle of the century. NASA has detected a noticeable increase in hardness and wear resistance in the materials used on space shuttles returning from space, especially aluminum components. These findings have revealed the potential of cryogenic heat treatment to improve the properties of metallic materials. Since then, cryogenic heat treatment has been adapted by various methods to improve the macroscopic and microscopic properties of metallic materials and significant achievements have been achieved in industrial applications. This process improves the microstructure of the materials, increases their durability and enables the emergence of longer-lasting and efficient products that meet the performance requirements [3-4]. However, a study by Hong et al. [5] indicated that cryogenic heat treatment reduces the cost by 50%. Therefore, it is recognized as an environmentally friendly and economical approach to improving materials.

Deep cryogenic processing (DCT) involves holding materials at very low temperatures, such as -125 to -196 °C, for 12 to 48 hours [6]. In deep cryogenic processes, materials are gradually cooled from room temperature to cryogenic temperatures of -196°C. After maintaining this temperature for a certain period of time, the temperature is raised to room temperature at the same rate as the cooling rate. The use of liquid nitrogen or nitrogen gas as the cooling medium avoids thermal stress problems during slow cooling [7].

In general, in tool steels, the purpose of deep cryogenic treatment is to remove residual austenite and distribute fine carbides evenly. The transformation from austenite to martensitic phase begins at the martensite initial temperature ( $M_s$ ) and is completed at the martensite ending temperature ( $M_f$ ). However, the martensite terminal temperature ( $M_f$ ) is considered

Corresponding Author: Volkan Karakurt  
E-mail: volkan.karakurt@saglammetal.com

How to cite this article:

Karakurt, V., Öztürk, F., Çitrak, T., Gözüak, G.N., Zığındere, O., Effect of deep cryogenic treatment on microstructural and mechanical properties of high-performance CPOH and WP7V tool steels, The International Journal of Materials and Engineering Technology (TIJMET), 2024, 7(2): 77-84

to be below room temperature. This results in the partial transformation of austenite to martensite during rapid cooling (Q). Deep cryogenic treatment accelerates the conversion of retained austenite to martensite by reducing the temperature to extremely low temperatures (-196 °C). At the same time, deep cryogenic treatment contributes to the formation of finer secondary carbides [8–10]. These changes in the microstructure after cryogenic treatment of tool steels help improve the mechanical properties of the material, including hardness, impact strength and wear resistance [11]. Marcos Perez et al., [12] in their study, investigated the effect of deep cryogenic heat treatment applied at -196°C for 12 hours on the mechanical properties of AISI H13 steel. They reported that the cryogenic heat treatment significantly improved the fracture toughness of H13 steel, attributing this improvement to the homogeneous distribution of fine carbides resulting from the cryogenic process. In another study, D. Das et al., [13] investigated the effect of deep cryogenic heat treatment performed at -196°C for 36 and 84 hours on carbide precipitation and tribological behavior of D2 steel. The samples subjected to both conventional and deep cryogenic heat treatment were tested for wear under sliding conditions at three different loads (49.05 N, 68.67 N, and 78.48 N) using a constant sliding speed. Their findings demonstrated that deep cryogenic heat treatment promotes the formation of refined secondary carbides, increases their volume fraction, and leads to a more homogeneous distribution. They also reported that the wear resistance of the material improved due to a reduction in retained austenite, an increase in carbide content, and the homogeneous distribution of carbides.

This study investigates the effects of deep cryogenic treatment (DCT) on the next-generation tool steels, CPOH and WP7V, in comparison to conventional quenching and tempering (QT) processes. DCT is applied to enhance the performance of these innovative steels, which are subjected to challenging industrial conditions. To date, no studies in the literature have examined the application of cryogenic treatment on these patented steels, making this research a valuable contribution to achieving superior performance in industrial applications.

In this context, samples treated with and without DCT were analyzed for hardness, microstructure, and mechanical properties (wear and impact resistance). The findings of this study provide a comprehensive evaluation of how DCT affects the performance of steels compared to traditional heat treatment methods.

## 2. Materials and methods

### 2.1. Materials

Table 1 shows the chemical compositions of CPOH and WP7V tool steels. The tool steels were obtained from SAĞLAM METAL A.Ş.

**Table 1.** Chemical composition of CPOH and WP7V tool steels

Tool Steel	Fe	C	Cr	Mo	V
CPOH	Balance	1.00	8.00	2.50	0.30
WP7V	Balance	0.50	7.80	1.50	1.50

### 2.2. Heat treatment of the materials

Quench and tempering heat treatments of tool steels were carried out in a vacuum environment in the Schmetz furnace at Sağlam Metal. Both tool steels were gradually pre-annealed at

different temperatures after vacuum was applied and then the furnace was raised to process temperature. After the austenitic transformation was achieved at 1040 °C for 45 minutes, the materials were cooled with nitrogen gas and the martensitic transformation (hardening) of the tool steel was carried out. For comparison purposes, some samples were taken into a deep cryogenic heat treatment cabinet and subjected to deep cryogenic heat treatment at -150 °C for 24 hours. In this process, nitrogen gas was used as the cooling medium. Then, tool steels without deep cryogenic heat treatment (conventional quench) and with deep cryogenic heat treatment were completed with two-stage tempering under the same conditions at 520°C for 5 hours. The heat treatment process applied to CPOH and WP7V tool steels is shown in the graph in Figure 1.

### 2.3. Microstructure investigations of materials

For metallographic examinations, the tool steels were first sanded with sandpaper at 320, 600, 800, 1200 and 2500 grit intervals and the surface cleaning was completed by polishing with 3 µm diamond paste. Chemical etching of the samples was carried out by immersion in 100 ml of distilled water containing 3% Nital (HNO<sub>3</sub>). Microstructure characterizations were performed using a Nikon LV150N flat metal microscope.

### 2.4. Hardness measurements

Hardness measurements of tool steels were carried out by the Vickers method using the Future-Tech FM800e device with a diamond pyramid tip under a load of 500 gf. Measurements were made with a sinking time of 10 seconds and five separate measurements were taken for each material and the average value was reported.

### 2.5. Impact Test

Impact test samples with dimensions of 75x10x10 mm were prepared from tool steels with and without deep cryogenic treatment. Charpy Impact Test was carried out in Karabük University Iron and Steel Institute MARGEM Laboratory according to ASTM E23-16b standard. Charpy Impact Test results of CPOH and WP7V tool steels were calculated by taking the average of 2 tests.

### 2.6. Wear test

Wear tests of tool steels were carried out using the linear wear test device within Sağlam Metal. Tool steels were tested using aluminum trioxide (Al<sub>2</sub>O<sub>3</sub>) balls in a dry environment, at a speed of 175 rpm and under a load of 20 N for a distance of 500 meters. After the test, volume losses were determined by examining the surface profilometry of the wear marks on the materials.

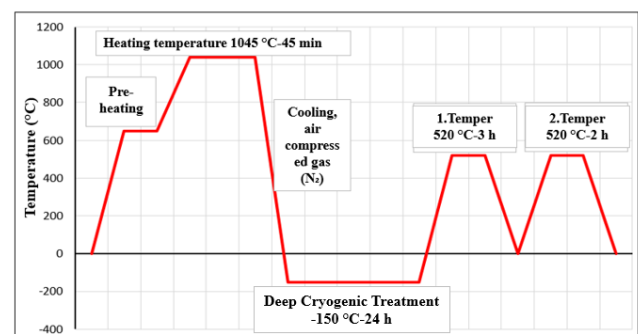


**Figure 1.** Process graph of heat treatment of CPOH and WP7V quality tool steels

### 3. Results and discussion

#### 3.1. Microstructure investigations

Figures 2 and 3 show the microstructure images of CPOH and WP7V tool steels with conventional (QT) and deep cryogenic heat treatment (DCT). The microstructure of both steels consists of matrix and carbides. In both cases, the matrix consists primarily of tempered martensite. The irregular, spherical, white structures seen in microstructural images are alloyed carbide phases, which are primary and secondary carbides [14]. In Figures 2(a) and 3(a), micrographs of CPOH and WP7V tool steels without cryogenic treatment reveal an uneven distribution of primary carbides. Additionally, the presence of austenite retained in the microstructure of WP7V tool steel without deep cryogenic treatment is observed more clearly in Figure 3 (a).

When the cryogenically treated microstructure images of CPOH and WP7V tool steels presented in Figure 2(b) and Figure 3(b) are examined, it is seen that both steels have a tempered martensite structure, primary carbides are not observed and secondary carbides are smaller than 5  $\mu\text{m}$ . The formation mechanism of secondary carbides is attributed to thermal stresses generated during the deep cryogenic process, leading to the fragmentation or refinement of existing large primary carbides into smaller secondary carbides [15–16]. There are also effects of deep cryogenic treatment such as (i) homogeneous redistribution of fine alloy carbide, (ii) precipitation of very small size ( $<1 \mu\text{m}$ ) carbide alloy elements. [17].

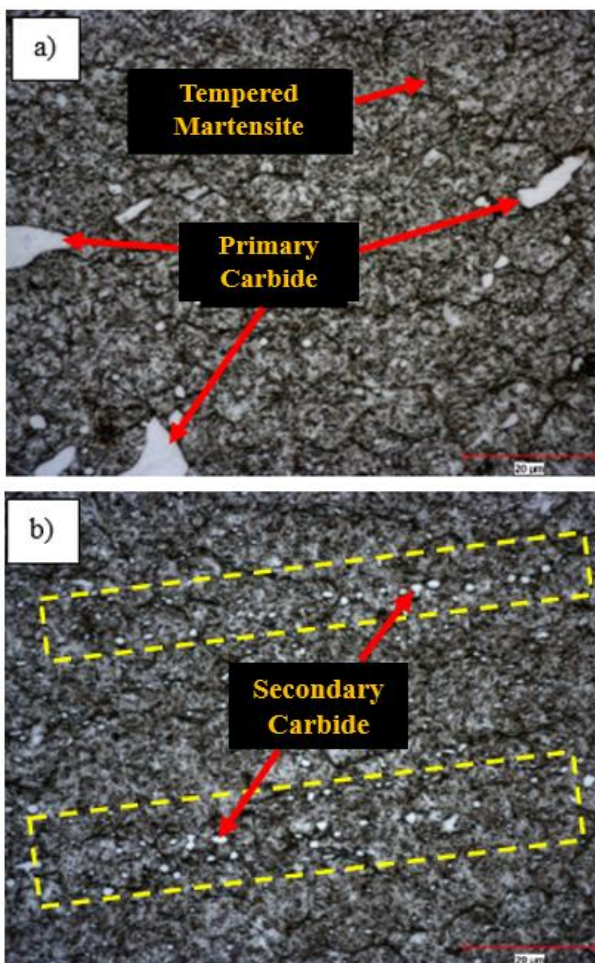


**Figure 2.** Optical microstructure image of CPOH tool steel at 1000X magnification a) QT, b) Q+DCT+T

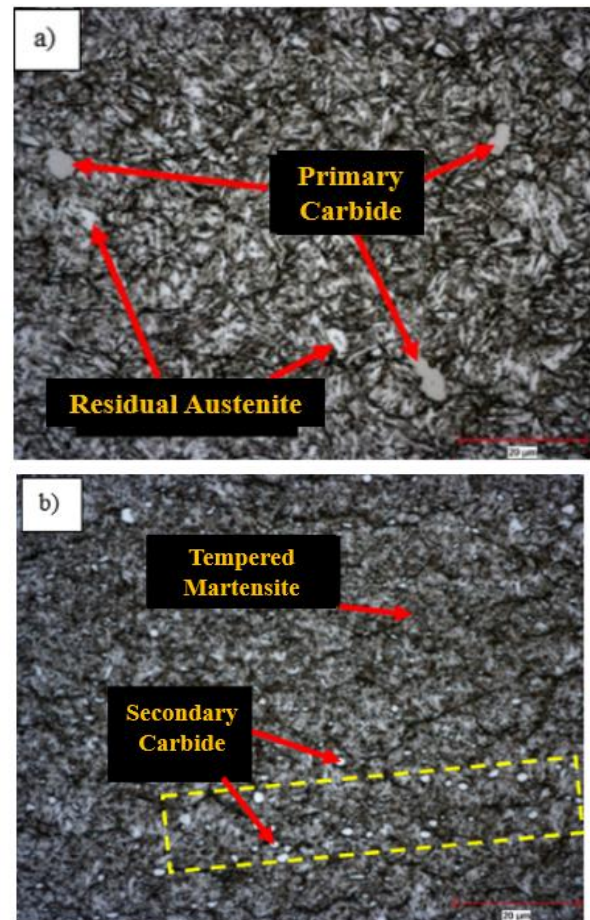


**Figure 3.** Optical microscope image of WP7V tool steel at 1000X magnification a) QT, b) QT+DCT+T

#### 3.2. Hardness test results

Vickers hardness results of CPOH and WP7V tool steels without deep cryogenic treatment (Conventional (QT)) and with deep cryogenic heat treatment (DCT) are shown in Figure 4. The hardness of CPOH and WP7V tool steels with conventional heat treatment was determined as 788.8 HV and 714.9 HV, respectively. The hardness of CPOH and WP7V tool steels subjected to deep cryogenic heat treatment was measured as 803.1 HV and 724.7 HV, respectively. After deep cryogenic heat treatment, an increase in the hardness of the tool steel was observed by 15 HV for CPOH and 10 HV for WP7V. This increase in hardness after deep cryogenic heat treatment increases the hardness strength by causing the remaining austenite, a softer phase seen in the microstructure image, to transform into martensite, a harder phase with a higher carbon content [18]. Moreover, hardness increased in deep cryogenic heat treated samples due to continuous austenite removal, more uniform carbide distribution, and higher secondary carbide content [19–20]. It is reported in the literature that the presence of secondary fine carbides significantly increases the mechanical strength of steel due to their small and hard properties [21].

In both cases, CPOH tool steel was observed to be harder than WP7V. This is due to the fact that CPOH tool steel contains 0.5% more carbon than WP7V tool steel in the chemical composition given in Table 1. The higher amount of carbon in CPOH tool steel increases the solid solubility in the steel crystal structure, causing the crystals to bond more tightly to each other and increasing the hardness [22].

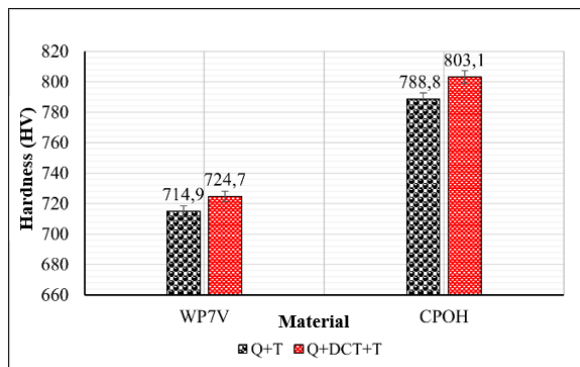


Figure 4. Hardness test results of QT and DCT heat treated CPOH and WP7V tool steels

3.2. Impact test results

Table 2 shows the data obtained from the Charpy impact test. While the average impact energy of CPOH and WP7V tool steels subjected to conventional heat treatment was calculated as 2.11 J and 5.8 J, respectively, the impact energy of CPOH and WP7V tool steels subjected to deep cryogenic heat treatment was calculated as 3.77 J and 8.76 J. It was observed that the impact energy increased when both tool steels were subjected to deep cryogenic processing. The notch impact strength of the material was calculated using the notch impact strength calculation formula (1) [23]. The impact strength of CPOH tool steel was found to be 26.38 kJ/m<sup>2</sup> after conventional heat treatment, while it was 47.13 kJ/m<sup>2</sup> after deep cryogenic heat treatment. The impact notch strength of WP7V tool steel under conventional heat treatment and deep cryogenic heat treatment was found to be 72.5 kJ/m<sup>2</sup> and 109.5 kJ/m<sup>2</sup>, respectively. It was observed that the impact notch strength of both tool steels increased after deep cryogenic heat treatment.

$$\text{Impact strength} = \frac{\text{absorbed energy}}{A} \tag{1}$$

A = Cross-sectional area in the notch area

This increase in impact toughness resulting from deep cryogenic treatment is believed to be an improvement due to finer and more uniform carbide precipitation seen in microstructural images [24]. In both conditions, CPOH tool steel was found to have lower impact notch strength compared to WP7V tool steel. The higher the carbon content in tool steels, the more brittle the material becomes, thus reducing its ductility and making the steel more brittle. Based on this mechanism, it was concluded that the impact notch strength of CPOH tool steel was lower than that of WP7V tool steel.

Table 2. Charpy Impact Test Results of CPOH and WP7V Tool Steels

Tool Steels	Average Impact Energy (J)		Impact Strength (kJ/m <sup>2</sup> )	
	QT	Q+DCT+T	QT	Q+DCT+T
CPOH	2.11	3.77	26.38	47.13
WP7V	5.8	8.76	72.5	109.5

3.4. Wear test results

Table 3 shows the average friction coefficients of CPOH and WP7V tool steels obtained from the dry wear test for 500 m. While the friction coefficient of CPOH tool steel with

conventional heat treatment was 0.478μ, the friction coefficient after deep cryogenic heat treatment was 0.389μ. While the friction coefficient of WP7V tool steel was 0.545μ after conventional heat treatment, it decreased to 0.401μ after cryogenic treatment. Both materials showed a decreasing trend in friction coefficient after deep cryogenic treatment.

Table 3. Coefficient of friction values of CPOH and WP7V tool steels.

Tool Steel	Coefficient of Friction (μ)	
	QT	Q+DCT+T
CPOH	0.478	0.389
WP7V	0.545	0.401

Figure 5 shows the 3D profile topographies of the wear scars of (a) conventional (b) deep cryogenically treated CPOH tool steel after the wear test. Considering the color concentration, it was observed that the depth color concentration of the deep cryogenically treated material was lower than that of the conventionally heat treated material.

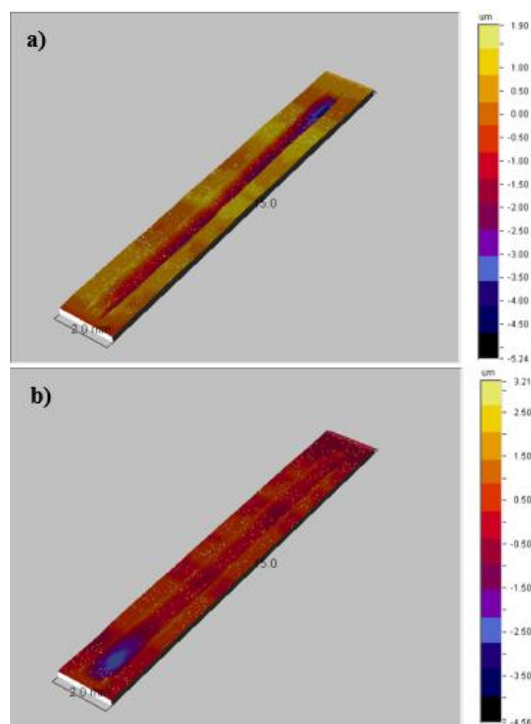


Figure 5. 3D surface topography images of CPOH tool steel a) QT, b) Q+DCT+T

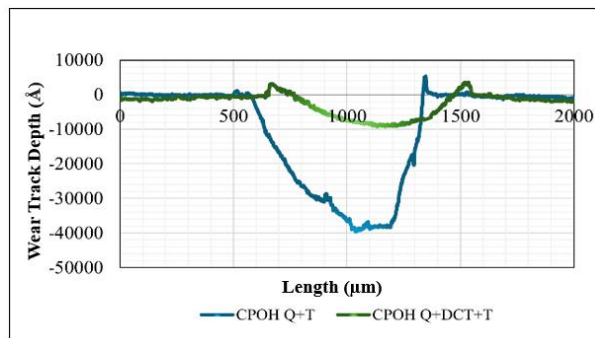


Figure 6. Two-dimensional profilometer images of the worn surfaces of conventional and deep cryogenic heat treated CPOH tool steel

Figure 6 shows the 2D profilometer image of conventional (QT) and deep cryogenic heat treated (DCT) CPOH tool steel after the wear test under 20 N load. Detailed examination of the profilometer images shows that deep cryogenic treatment reduces the pit depth and wear area.

Figure 7 shows the 3D surface topographies of (a) conventional and (b) deep cryogenic treated WP7V tool steel after the wear test. It is observed that the depth color concentration is higher in the conventional heat treated 3D topography of WP7V tool steel compared to the deep cryogenic treated material.

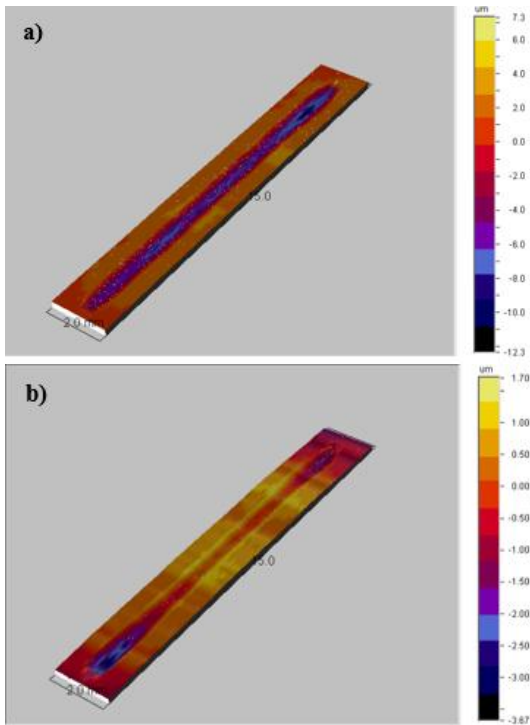


Figure 7. 3D surface topography images of WP7V tool steel a) QT, b) Q+DCT+T

cryogenic heat treatment showed better wear resistance compared to WP7V tool steel with conventional and deep cryogenic heat treatment. In both cases, it is thought that the fact that CPOH tool steel has a lower pit depth than WP7V tool steel is due to the alloying elements it contains. The high carbon content in CPOH tool steel increases the hardness resistance, making the interatomic bonds in the material stronger during wear as the hardness increases. This makes it difficult for abrasive particles to dislodge the material. This reduces the effectiveness of mechanisms such as microscraping and notching as the material hardens.

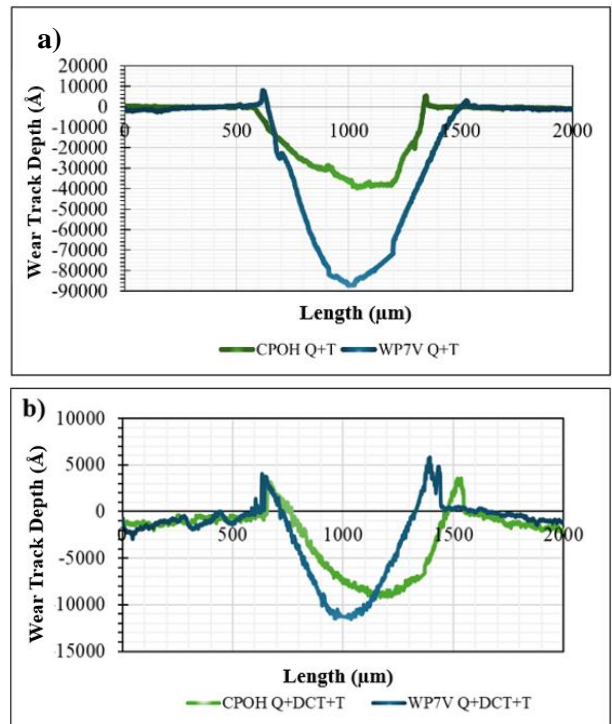


Figure 9. Comparative wear depth plot of CPOH and WP7V tool steel a) QT, b) Q+DCT+T

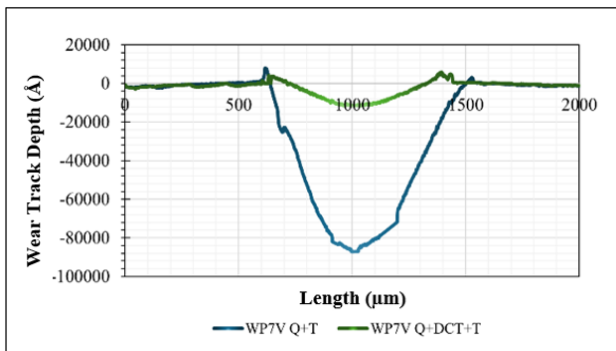


Figure 8. Two-dimensional profilometer images of the worn surfaces of conventional and deep cryogenic heat treated WP7V tool steel

Figure 8 shows the 2D profilometer image of conventional (QT) and deep cryogenic heat treated (DCT) WP7V tool steel after the wear test under 20 N load. The deep cryogenic heat-treated WP7V tool steel was observed to exhibit less wear depth and better wear properties compared to the conventionally heat-treated WP7V tool steel.

In Figure 9, the wear depths of conventional and deep cryogenic heat treated CPOH and WP7V tool steels are compared. CPOH tool steel with conventional and deep

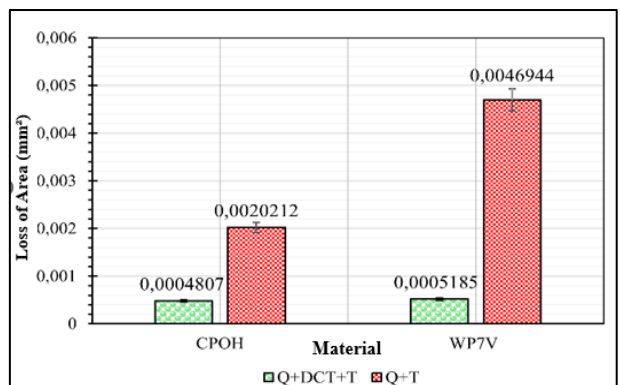


Figure 10. Area measurements calculated from two-dimensional profilometer images of the worn surfaces of CPOH and WP7V tool steel

Figure 10 shows the area loss diagram of the material, consistent with the wear scars obtained from two-dimensional profilometer analyzes of CPOH and WP7V tool steels. It is observed in Figure 10 that the highest area loss occurs in conventionally heat-treated WP7V tool steel.

Although area loss after deep cryogenic heat treatment decreased compared to conventional heat treatment for both tool

steels, for WP7V tool steel, deep cryogenic heat treatment resulted in a more significant improvement in area loss compared to CPOH tool steel. This observation can be explained by the fact that the alloying elements in WP7V tool steel promote secondary carbide formation. It is thought that the high content of vanadium alloying element in WP7V tool steel allows the precipitation of vanadium-rich secondary carbides [25].

Figure 11 shows the wear rate graphs of WP7V and CPOH tool steels. Wear rates were calculated with the formula given below [26].

$$\text{Wear rate} = \frac{\text{loss of area}}{\text{load} \times \text{distance} \times \text{density}} \quad (2)$$

The wear rates of CPOH and WP7V tool steels subjected to conventional heat treatment are  $2.57478\text{E-}08$  and  $5.98013\text{E-}08$ , respectively. The wear rates of CPOH and WP7V tool steels subjected to deep cryogenic heat treatment were  $6.12357\text{E-}09$  and  $6.6051\text{E-}09$ , respectively. A significant reduction in the wear rates of both tool steels subjected to deep cryogenic heat treatment was observed. The effect of deep cryogenic heat treatment to improve wear resistance is thought to be due to the increased density of uniformly dispersed fine secondary carbides formed by deep cryogenic heat treatment and the removal of retained austenite, a soft phase [27-28]. After deep cryogenic treatment, an improvement in wear resistance of 76.22% for CPOH tool steel and 88.95% for WP7V tool steel was observed.

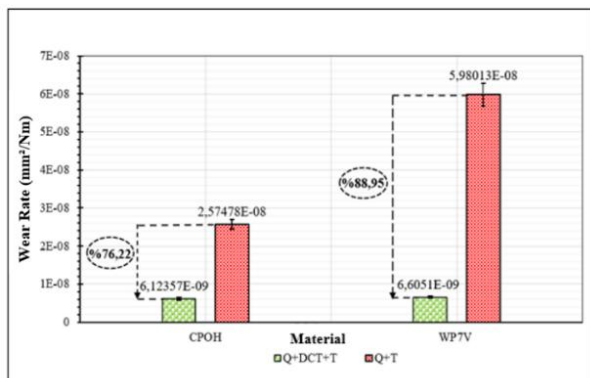


Figure 11. Wear rate graphs of CPOH and WP7V tool steels

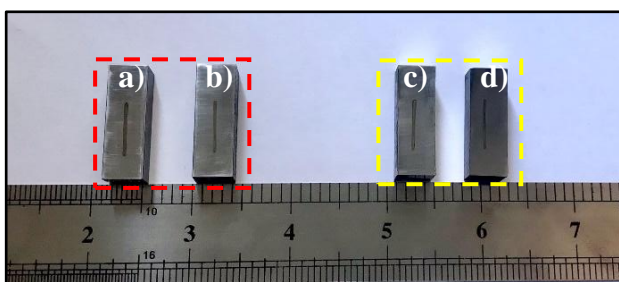


Figure 12. Macro images of WP7V and CPOH tool steels subjected to wear testing. a) WP7V QT, b) WP7V Q+DCT+T, c) CPOH QT, d) CPOH Q+DCT+T

According to the wear test results applied over a distance of 500m under 20N load, macro and micro images of the wear marks of conventional and cryogenically treated WP7V and CPOH tool steels are presented in Figure 12 and Figure 13. As seen in the 50X microstructure images of the wear scars in Figure 13, it was determined that conventionally heat-treated

WP7V and CPOH tool steels had wider scar depths compared to their cryogenically treated forms.

When the wear traces of (a) conventional (Q+T) and (b) cryogenically treated (Q+DCT+T) states of WP7V tool steel are examined in Figure 13, it is seen that in the case of conventional heat treatment, the parts broken off from the surface along the wear trace are removed from the system without adhering to the surface again. It is considered to be moving away. At the same time, it is seen that they do not interact much with the surfaces of the sample and the alumina ball. This indicates that it exhibits intense abrasive wear. In the case where cryogenic treatment was applied, particles adhering to the surface as well as intense abrasive wear were observed. Adhesive wear type was also occasionally exhibited in cases where cryogenic treatment was applied.

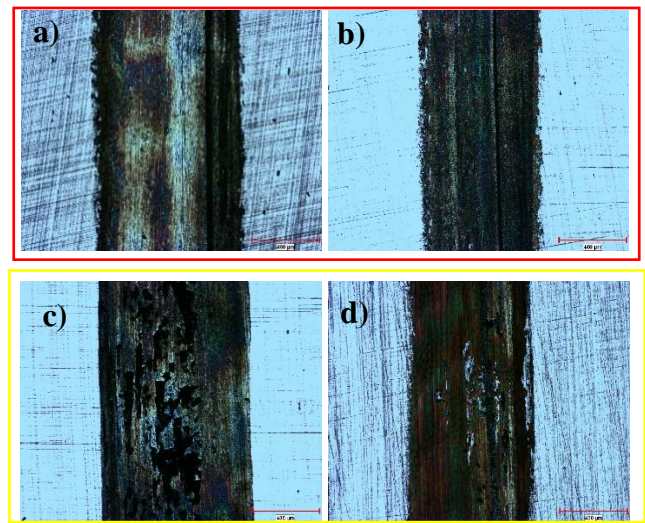


Figure 13. 50X optical microscope images of WP7V and CPOH tool steels subjected to wear testing, a) WP7V QT, b) WP7V Q+DCT+T, c) CPOH QT, d) CPOH Q+DCT+T

Figure 13 shows the wear marks of both conventional (Q+T) and cryogenically heat-treated (Q+DCT+T) forms of CPOH tool steel. In both (c) conventional and (d) cryogenic heat treated forms, it is observed that adhesive wear is dominant, with the particles that break off at the beginning of wear sticking to the surface again.

The predominance of adhesive wear in CPOH tool steel is considered to stop or slow down the progression of wear during sliding compared to WP7V tool steel. As seen in the wear rate graphs in Figure 11, CPOH tool steel supports this assessment by exhibiting a lower wear rate compared to WP7V tool steel.

Figure 14 illustrates the schematic wear mechanism based on carbide size and distribution. As shown in the mechanism, homogeneously distributed secondary carbides create a uniform hardness and surface during wear, resulting in stable wear across the entire surface. In contrast, the wear mechanism of tool steel with primary carbides reveals that irregularly distributed primary carbides lead to instability on the tool steel surface, causing more wear in areas lacking carbides due to lower hardness.

This mechanism highlights the wear characteristics of materials subjected to both conventional and deep cryogenic heat treatments. The research findings indicate that the presence of primary carbides in conventionally heat-treated materials increases the wear rate, whereas the wear rate decreases after

deep cryogenic treatment due to the formation of secondary carbides, enhancing wear resistance.

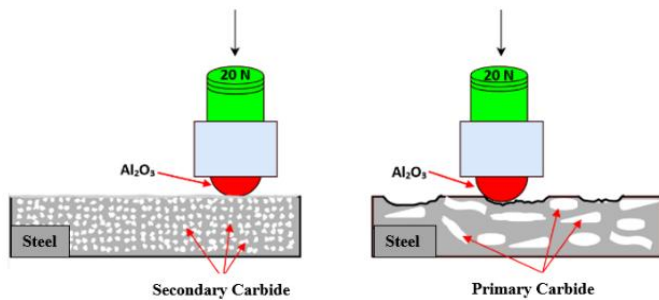


**Figure 14.** Schematic illustration of the wear mechanism according to carbide type (Primary-Secondary) and distribution

Additionally, it is believed that the deep cryogenic treatment in CPOH and WP7V tool steels induces martensitic conditioning, leading to the formation of defects such as dislocations, where carbon atoms accumulate. Deep cryogenic treatments also generate residual compressive stresses within the structure, particularly at interfaces such as the carbide-matrix interface. These compressive stresses can mitigate the tensile stresses that occur during wear, thereby reducing crack initiation and propagation and enhancing the adhesion of carbides to the matrix. This results in improved wear resistance during wear [29-30].

#### 4. Conclusions

- In this study, the hardness of CPOH tool steel treated with conventional heat treatment was measured at 788.8 HV, whereas the hardness of CPOH tool steel subjected to deep cryogenic treatment was 803.1 HV. It was found that the deep cryogenic treatment increased the material's hardness by 1.8%.
- While the hardness of WP7V tool steel with conventional heat treatment was measured as 714.9 HV, the hardness of WP7V tool steel with deep cryogenic treatment was measured as 724.7 HV. Deep cryogenic treatment increased the hardness of WP7V tool steel by 1.4%.
- According to the Charpy impact test results, the average impact energy of CPOH tool steel increased by 78.67% after deep cryogenic treatment, while the average impact energy of WP7V tool steel increased by 51.03%.
- According to the wear test results, the application of deep cryogenic treatment reduced the area loss of CPOH tool steel by 76.22% and the area loss of WP7V tool steel by 88.95%.
- Compared with conventional heat treatment, deep cryogenic treatment reduced the wear rate of CPOH tool steel by 76.22% and the wear rate of WP7V tool steel by 88.95%.
- As a result of the study, it was evaluated that deep cryogenic treatment, when used in conjunction with conventional heat treatment in both new generation tool steels and other tool steels, can improve mechanical and wear properties, thereby extending the service life in applications where wear and impact resistance are critical, such as in the aerospace, automotive, defense, and metalworking and machinery industries.

#### Author contributions

Volkan Karakurt: Investigation, writing, review, explanation of wear mechanisms

Talip Çitrak: Performing of hardness measurements, heat treatment of samples according to specific parameters

Feyzanur Öztürk: Performing of wear tests

Orçun Zığındere: Interpretation of impact tests, review & editing, conceptualization

Gamze Nur Gözüak: Microstructure characterization

#### References

1. Koçak H., Takım Çelikleri, 10. Baskı, Bolokur Teknik Yayıncılık A.Ş., **2019**
2. Podgornik, B., et al., Deep cryogenic treatment of tool steels, *Journal of Materials Processing Technology*, **2016**, 229, 398-406
3. Jovičević-Klug, P., & Podgornik, B., Review on the effect of deep cryogenic treatment of metallic materials in automotive applications, *Metals*, **2020**, 10(4):434
4. Jovicevic-Klug, P., Mechanisms and Effect of Deep Cryogenic Treatment on Steel Properties, Institute of Metals and Technology: Ljubljana, Slovenia, **2022**
5. Hong, S. Y., & Broomer, M., Economical and ecological cryogenic machining of AISI 304 austenitic stainless steel, *Clean Products and Processes*, **2000**, 2(3):157-166
6. Molinari, A., et al., Effect of deep cryogenic treatment on the mechanical properties of tool steels, *Journal of materials processing technology*, **2001**, 118(1-3): 350-355
7. Sonar, T., Sachin L., and Chandrashekar G., Cryogenic treatment of metal—a review, *Materials Today: Proceedings*, **2018**, 5(11):25219-25228
8. Pérez, M., and Francisco J. B., The effect of deep cryogenic treatments on the mechanical properties of an AISI H13 steel, *Materials Science and Engineering: A*, **2015**, 624, 32-40
9. Gill, S.S., et al., Metallurgical principles of cryogenically treated tool steels—a review on the current state of science, *The International Journal of Advanced Manufacturing Technology*, **2011**, 54, 59-82
10. Dumasia, C. A., et al., A review on the effect of cryogenic treatment on metals, *International Research Journal of Engineering and Technology*, **2017**, 4(7): 2402-2406
11. Jovičević-Klug, P., Tóth, L., & Podgornik, B., Comparison of K340 Steel Microstructure and Mechanical Properties Using Shallow and Deep Cryogenic Treatment, *Coatings*, **2022**, 12, 1296
12. Pérez, M., and Francisco J. B., The effect of deep cryogenic treatments on the mechanical properties of an AISI H13 steel, *Materials Science and Engineering: A*, **2015**, 624, 32-40
13. Das, D., et al., Effect of deep cryogenic treatment on the carbide precipitation and tribological behavior of D2 steel, *Materials and Manufacturing Processes*, **2007**, 22(4), 474-480
14. Mochtar, et al., Effect of tempering temperature and subzero treatment on microstructures, retained austenite, and hardness of AISI D2 tool steel, *Materials Research Express*, **2023**, 10(5): 056511
15. Jain, A.S., et al., Refinement of primary carbides in hypereutectic high-chromium cast irons: a review, *Journal of Materials Science*, **2021**, 56, 999-1038
16. Podder, A.S., Lonardelli, I., Molinari, A., & Bhadeshia, H.K.D.H., Thermal stability of retained austenite in bainitic



- steel: an in situ study, *Proceedings of the Royal Society A: Mathematical, Physical and Engineering Sciences*, **2011**, 467(2135), 3141-3156
17. Demir E., Toktaş I., Effects of cryogenic treatment on residual stresses of AISI D2 tool steel *Metallic Materials*, **2018**, 56, 153-61
  18. Essam, M.A., et al., Effect of Deep Cryogenic Treatment on Wear Behavior of Cold Work Tool Steel, *Metals*, **2023**, 13(2):382
  19. Garcia, C., et al., Effect of vanadium carbide on dry sliding wear behavior of powder metallurgy AISI M2 high speed steel processed by concentrated solar energy, *Materials Characterization*, **2016**, 121, 175-186
  20. Amini, K., et al., Effect of deep cryogenic treatment on the formation of nano-sized carbides and the wear behavior of D2 tool steel, *International Journal of Minerals, Metallurgy, and Materials*, **2012**, 19, 795-799
  21. Akhbarizadeh, A., Effects of cryogenic treatment on wear behavior of D6 tool steel, *Materials & Design*, **2009**, 30(8): 3259-3264
  22. Salunkhe, S., et al., Effect of single and double austenitization treatments on the microstructure and hardness of AISI D2 tool steel, *Materials Today: Proceedings*, **2015**, 2(4-5):1901-1906
  23. Soy, U., 1000 Soruda Malzeme Bilimi, *Değişim Yayınları*, **2017**
  24. Pellizzari, M., Caliskanoglu, D., Fernández, A., Barbero, J. I., Pena, B., Uemit, T., & Alava, L.A., Influence of different deep cryogenic treatment routes on the properties of high speed steel, *HTM Journal of Heat Treatment and Materials*, **2012**, 67(2), 111-117
  25. Jubica, J., Characterization of Secondary Carbides in Low-Alloyed Martensitic Model Alloy Tool Steels, **2020**
  26. Yazıcı, M., et al., 316l İmplant Malzemesinin Aşınma ve Manyetik Özellikleri Üzerine Plazma Nitrürleme Sıcaklığının Etkisi, *Mühendislik Bilimleri ve Tasarım Dergisi*, **2014**, 2(3):319-326
  27. Korade, D., Ramana, K.V., Jagtap, K., Influence of cryogenic treatment on the tribological behaviour of AISI H21 tool steel, *Materials Research*, **2018**, 22, e20170745
  28. Xu, G., et al., Microstructural variations and mechanical properties of deep cryogenic treated AISI M35 high-speed steel tempered at various temperatures, *Journal of Materials Research and Technology*, **2022**, 17, 3371-3383
  29. Gerson, A., Microstructure of Cryogenically Treated High Performance Tool Steels, *Materials Australia, Australia*, **2007**
  30. Das, D., Dutta, A.K., and Ray, K.K., Correlation of microstructure with wear behaviour of deep cryogenically treated AISI D2 steel, *Wear*, **2009**, 267(9-10):1371-1380

# Experimental and numerical investigation of the use of organic and inorganic materials melted with infrared rays for thermal energy storage

Ali Kemal Özcan<sup>\*1</sup>, Ömer Öksüz<sup>2</sup> and Cevdet Demirtaş<sup>2</sup>

<sup>1</sup>Karadeniz Technical University, Graduate School of Natural and Applied Science, Trabzon, Türkiye

<sup>2</sup>Karadeniz Technical University, Faculty of Engineering, Department of Mechanical Engineering, Trabzon, Türkiye

## Article Info

### Article history:

Received 12.09.2024

Revised: 26.12.2024

Accepted: 30.12.2024

Published Online: 31.12.2024

### Keywords:

Infrared rays

Paraffin

Hitec salt

Thermal storage

## Abstract

Energy storage processes need to be researched and developed to ensure the conversion and sustainability of energy. The original value of this study lies in the experimental and numerical investigation of the performance of an innovative heat storage system using infrared radiation and phase change materials (PCMs). In a laboratory setting, infrared rays emitted by a lamp are directed through a conical concentrator onto organic as paraffin and inorganic Hitec salts. These materials are melted and analyzed for their potential use in thermal energy storage. During a 4-hour charging process, the focal temperature ranged between 200–300°C. The maximum temperatures measured in the upper region of a 10-liter furnace were 87°C for paraffin and 240°C for Hitec salts. In the subsequent 4-hour discharge process, the upper region temperature of the Hitec salt decreased from approximately 102°C to 46°C, while the paraffin's temperature dropped from 75°C to 55°C. With mass flow rates of 0.047 g s<sup>-1</sup> for paraffin and 0.061 g s<sup>-1</sup> for Hitec salt, the average thermal efficiencies in the furnace were calculated as 56% for paraffin and 65.6% for Hitec salts. The first-law thermodynamic efficiencies were determined to be 8% for paraffin and 19.7% for Hitec salts. In summary, paraffin is ideal for low-temperature applications (below 80°C), while Hitec salts are more suitable for medium to high-temperature applications due to their superior thermal properties.

## 1. Introduction

There are many different energy production methods to meet the demand for energy consumption. The demand for renewable and sustainable energy production and energy storage methods is increasingly increasing. Innovative energy storage methods are being researched and implemented to ensure continuity and diversity in energy. Thermal energy storage studies are also increasing with the point heat source created by concentrating solar energy, which is one of the renewable energy sources. Thermal energy is provided with infrared lamps to ensure continuity in cases where there is no solar energy. The phase change materials used in thermal energy storage consist of organic, inorganic and eutectic mixtures. Thermal energy storage types made with phase change materials are sensible and latent heat storage.

Latent heat storage systems (LHSS) are leading the way in providing environmentally friendly energy saving solutions. Solid-liquid phase change materials are particularly attractive and innovative for thermal energy storage because they offer a wide temperature range between the four possible phase transitions in LHSS (solid-liquid, liquid-liquid, liquid-gas, solid-gas and solid-solid) and have high heat storage capacities. These systems are classified into 3 categories: organic, inorganic and eutectic types, as seen in the Figure 1, which heat storage during the transition from solid to liquid phase and release it during the transition from liquid to solid phase [1].

Thermal processes such as melting and solidification can be carried out with the help of infrared lamps. There are very few

literature studies on these high current solar simulators. In the study conducted by Gallo et al., it is stated that solar simulators are widely used in cases where solar rays are not sufficient. In addition, solar simulators represent artificial high-current light sources similar to concentrated solar rays [2]. In a similar literature study, a high flux solar simulator was used to provide process heat for glass production using concentrated solar radiation. Preliminary information on the use and applicability of concentrated solar radiation to melt glass at optimum scale was presented [3].

In the study conducted by Sarı and Karaipekli, in order to obtain a stable composite as a phase change material (PCM), the determination of the appropriate amount of paraffin (n-docosane) absorbed into Expanded Graphite (EG) and the effect of EG addition on thermal conductivity were investigated using the transient hot wire method. The thermal conductivity of pure paraffin and composite PCMs containing 2%, 4%, 7%, and 10% EG by weight was measured as 0.22, 0.40, 0.52, 0.68, and 0.82 W/mK, respectively. For these composite PCMs, the composite containing 10% EG is more suitable for latent heat storage with higher thermal conductivity and better melting temperature [4].

In the study by Akgün et al., a vertical tube geometry was designed to determine the charging and discharging properties of paraffin as a phase change material. The thermophysical properties of the investigated paraffin were determined by differential scanning calorimetry analysis. The effect of increasing the inlet temperature and mass flow rate of the heat transfer fluid (HTA) on both the charging and discharging

Corresponding Author: Ali Kemal Özcan  
E-mail: ozcants61@gmail.com

How to cite this article:

Özcan, A.K., Öksüz, Ö., Demirtaş C., Experimental and numerical investigation of the use of organic and inorganic materials melted with infrared rays for thermal energy storage, The International Journal of Materials and Engineering Technology (TIJMET), 2024, 7(2): 85-99

processes of the PCM was investigated. An increase in the inlet temperature of the heat transfer fluid resulted in shorter melting times [5].

In order to increase the thermal conductivity of paraffin, the melting processes of pure paraffin and paraffin with 10%  $\text{Al}_2\text{O}_3$  nanoparticle doping by mass in a two-dimensional rectangular melting area were investigated numerically with ANSYS Fluent software by Arslan et al. The effect of increasing the wall temperature of the rectangular area to 65 °C, 70 °C and 75 °C on the total melting time for pure paraffin and nanoparticle-doped paraffin was investigated. As a result, it was found that the use of  $\text{Al}_2\text{O}_3$  nanoparticles increased the heat transfer rate of paraffin [6].

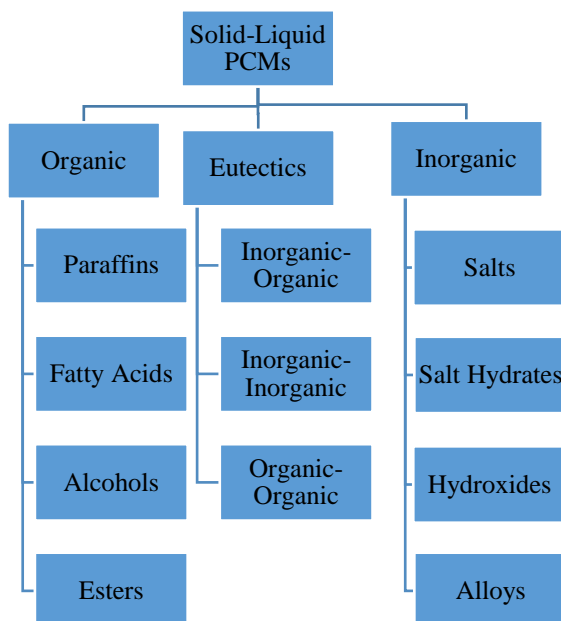


**Figure 1.** Classification of PCMs [1]

By Sinaringati et al., Paraffin and beeswax were used as PCM that can give off heat energy to heat the baby incubator. Paraffin and wax have high latent heat to keep the heat at constant temperature and release it. As a result, the PCMs were able to maintain heat energy at a temperature above 305 K for more than 8 hours in the infant incubator room. However, it was observed that beeswax performed better than paraffin in thermal energy storage [7].

There are many studies on molten salts. In this literature study, various triple and quadruple salt formulations containing  $\text{NO}_3/\text{NO}_2$  as an anion in addition to lithium and calcium in their formulations have been investigated in order to lower the melting points of molten salts for heat storage and thus provide higher operating temperature ranges [8]. By Fernandez et al., in order to improve the current solar salt used as thermal energy storage fluid in Concentrated Solar Power plants, Hitec blend consisting of 53%  $\text{KNO}_3$ , 40%  $\text{NaNO}_2$  and 7%  $\text{NaNO}_3$  by mass has been extensively studied. The Hitec molten salt shows better physicochemical properties than the binary solar salt (60%  $\text{NaNO}_3$  40%  $\text{KNO}_3$ ) due to its lower melting point, which can improve the operating temperature range in commercial solar power plants [9].

By Chauhan et al., solar dryers integrated with thermal energy storage units using paraffin wax were comprehensively investigated. Different types of paraffin wax and their thermophysical properties were presented, the thermal

performances of solar dryer with paraffin wax and without paraffin wax were investigated and their effects on drying time and drying efficiency were reported. Furthermore, different locations of TES units in the dryer were reviewed and methods to increase the heat transfer rate between paraffin wax and drying air were investigated. The advantages and challenges of using paraffin wax in solar drying technology were also discussed [10].

A study conducted by Kraiem et al., at the CERTES laboratory of Paris Est University, focusing on the thermophysical characterization of four paraffin's (RT21, RT27, RT35HC, RT50) at different temperatures in both solid and liquid phases showed that melting temperatures and latent heats decreased with increasing heating rate. The study observed that the thermal conductivity increases with temperature in the solid phase but decreases with increasing temperature in the liquid phase. It was also found that thermal diffusions in the liquid state decreased with temperature [1].

The rays coming out of the infrared lamp are aimed to be focused on the determined area by conical reflector. The originality of this study lies in the numerical and experimental investigation of the use of organic phase change material (paraffin) and inorganic phase change material (Hitec salt) molten using concentrated infrared rays in thermal energy storage. Both materials are analyzed for their potential in sensible and latent heat storage across medium to high temperature applications, ranging from 100 °C to 300 °C. In this study, the heat flux entering the furnace is found theoretically by determining the absorption coefficient and emissivity rate of the energy coming to the furnace by the PCM and finding the heat flux at the focus. Thus, the first law of thermodynamics efficiency of this system is also calculated. In this study, where the Computational Fluid Dynamics (CFD) finite element method is used, ANSYS Fluent software is used to analyze the thermal behavior in the furnace. As a result of numerical and experimental data, it has been shown that charged PCMs can be used for up to approximately 4 hours. In addition, with this method, it is aimed to measure the amount of molten material ( $\text{kg s}^{-1}$ ) depending on the infrared lamp power. Another aim is to present the stored thermal energy to the areas where it will be used, through heat exchangers created inside or outside the furnace. By performing processes without contacting organic and inorganic materials with the thermal power created by the rays, the harmful effects especially caused by the electrical conductivity of inorganic materials were also eliminated. In cases where renewable energy sources such as solar energy are insufficient, fuel heaters, infrared heaters and resistance heaters can be used as alternatives to provide continuous and reliable power.

## 2. Materials and methods

Infrared lamps, which are used artificially as substitutes for sunlight, are known for emitting both light and heat. The rays from the infrared lamp are focused on the furnace through a conical concentrator. Infrared lamps with different power ratings can be used depending on the desired focal temperature in the furnace. In this study, a single 500 W Golden Fer brand infrared lamp, powered by 220 V, was used. Additionally, the infrared lamp can be adjusted vertically to maintain a constant focal temperature. The infrared rays focused on the furnace melt the organic or inorganic phase change materials (PCMs), enabling thermal energy storage using materials with high heat capacity.

2.1. Experimental setup of the infrared lamp concentrator system

The infrared lamp concentrator system is based on the principle of focusing artificial rays onto a single point. A concentrator is placed between the light source and the receiver. The schematic representation of the ideal reflection of the infrared lamp and the basic geometric parameters of the conical concentrator system are shown in Figure 2. The number of conical concentrators can be increased up to the limit defined by the receiver surface area. Accordingly, the number of infrared lamps used corresponds to the number of conical concentrators. The physical properties and geometric dimensions of the conical concentrator system with the infrared lamp are provided in Table 1.

In the in Figure 2, A simple setup related to the reflection of the infrared ray concentrator system has been presented. Additionally, the infrared lamp is positioned at a 90° angle to the upper platform, which is designed to move up and down for adjustment if necessary. The infrared lamp and the concentrator can move together. This allows the artificial ray concentrator system to be easily positioned in the focal area of the receiving furnace. T-type thermocouples are placed at the bottom, middle, and top of the furnace to take temperature measurements. For the experiments, a 12-channel Lutron-brand datalogger with K-type and T-type thermocouples is used. Additionally, a K-type thermocouple is placed in the furnace for focal point temperature measurement. Temperature measurements are also taken with a thermal camera to support the thermocouple readings. The Fluke TiX501 thermal camera is capable of measuring temperatures in the range of -20 °C to 650 °C, with a thermal sensitivity of 0.075 °C at 30 °C and an infrared spectrum band of 7.5 μm to 14 μm.

2.2. Heat storage experiment of paraffin melted with infrared lamp

In the first experiment, paraffin ( $C_nH_{2n+2}$ ) suitable for low-temperature applications, was used as the PCM. The thermophysical properties of the paraffin used for thermal energy storage are provided in Table 2 [11]. A 9-liter glass jar was utilized as the furnace, with the surroundings insulated using glass wool and aluminum foil. The use of a glass furnace enables observation and measurement of the melted paraffin. A total of nine T-type thermocouples were placed in the jar furnace at the bottom, middle, and top, while two K-type thermocouples were positioned in the focal region. A schematic and general

view of the paraffin experimental setup is presented in Figure 3. The paraffin was melted and poured into the glass furnace to ensure homogeneous distribution. Once the paraffin cooled and solidified in the furnace, experiments were conducted using the ray concentrator system.

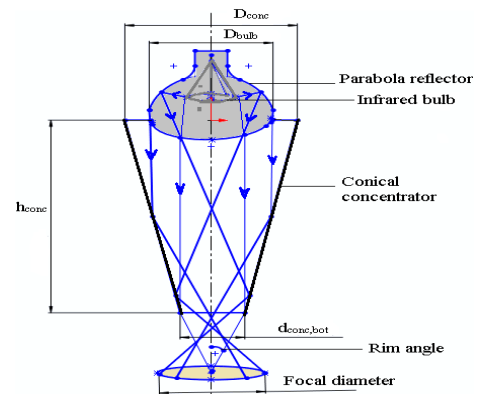


Figure 2. Schematic view of the positioning and geometric dimensions of the conical concentrator and infrared lamp

Table 1. Geometric properties and dimensions of the conical concentrator with infrared lamp

Geometric properties	Symbol	Value
Infrared lamp diameter	$D_{lamp}$	12 cm
Conical concentrator top diameter	$D_{conc}$	16 cm
Conical concentrator bottom diameter	$d_{conc,bot}$	6 cm
Conical concentrator length	$h_{conc}$	25 cm
Receiver focal diameter	$d_{focal}$	8 cm
Rim angle of concentrator	$\phi_R$	22.6°

Table 2. Thermophysical properties of paraffin [11]

Parameters	Symbol	Value
Density ( $kg\ m^{-3}$ )	$P$	870 (T= 300K) 780 (T= 340K)
Specific heat $c_p$ ( $J\ kg^{-1}K^{-1}$ )	$c_p$	2900
Thermal conductivity coefficient ( $W\ m^{-1}K^{-1}$ )	$K$	0.24 (T=300K) 0.22 (T= 340K)
Viscosity ( $kg\ m^{-1}s^{-1}$ )	$\mu$	0.0057933
Latent heat of fusion ( $kJ\ kg^{-1}$ )	$L_e$	190
Melting temperature (K)	$T_m$	331
Evaporation temperature (K)	$T_b$	355

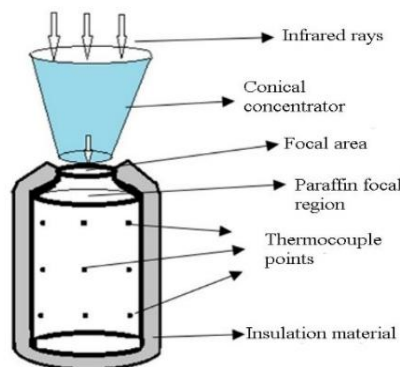


Figure 3. Schematic view of paraffin heat storage with infrared lamp and its appearance in the experiment

In the experiments, the temperature of the ray concentrator was initially adjusted due to the low evaporation point of paraffin (355 K). The temperature achieved by the rays entering

the furnace was maintained at approximately 80 °C. Consequently, while the upper region of the paraffin in the furnace reached a temperature of about 80 °C, the temperature

gradually decreased toward the bottom of the furnace. In Figure 4, a thermal camera (TiX501) image shows a temperature of 73.29 °C near the top of the furnace and 24.55 °C at the bottom. Meanwhile, the temperature measured at the conical concentrator was 128.81 °C

When Figure 5 is examined, the temperature of the upper region, measured with a thermal camera by momentarily opening the glass vertically from the edge of the furnace, is 74.4 °C, while the temperature near the middle region is 24.66 °C. Additionally, the emissivity coefficient measured by the thermal camera in these regions is 0.95.

2.3. Heat storage experiment of Hitec salt melted with infrared lamp

Inorganic Hitec salt (53% KNO<sub>3</sub>, 40% NaNO<sub>2</sub>, and 7% NaNO<sub>3</sub>), with a low melting point and high heat storage capacity, was used as a PCM in conjunction with the ray concentrator system. The thermophysical properties of the Hitec salt used for heat storage are provided in Table 3 [12,13]. To prepare approximately 26 kg of Hitec salt, 53% potassium nitrate, 40% sodium nitrite, and 7% sodium nitrate were mixed by weight and melted in an electric furnace. To homogenize the Hitec salt to 99% purity, it was cooled and ground into a powder. The powdered Hitec salt was then poured into the furnace. After preparation, the Hitec salt was calibrated by verifying its suitability for the desired melting temperature. A general view and schematic of the prepared Hitec salt heat storage experiment are shown in Figure 6. A 10-liter stainless steel furnace was used, with six T-type thermocouples placed at the bottom, middle, and top points, and two K-type thermocouples placed in the focal

region. The top of the furnace was covered with quartz glass to allow the passage of rays. The difference in this experiment was that all the rays were allowed to enter the furnace. As a result, high temperatures were achieved inside the furnace, causing the Hitec salt to begin melting.



Figure 4. An image of the infrared lamp experimental level taken with a thermal camera

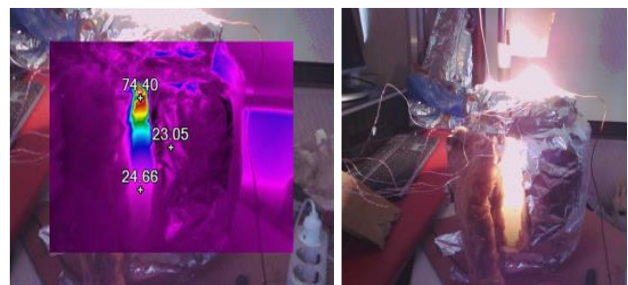


Figure 5. Images taken with a thermal camera over the glass furnace in the paraffin experiment

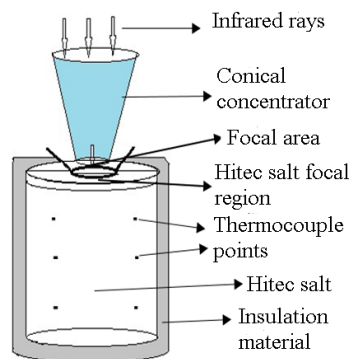


Figure 6. Schematic view of heat storage of Hitec salt by infrared lamp and its image in the experiment

Table 3. Some physical properties of Hitec salt [12,13]

Parameters	Symbol	Value
Density (solid-liquid)	$\rho$	(2013-1857) kg m <sup>-3</sup>
Specific heat (solid-liquid)	$c_p$	(1090-1570) J kg <sup>-1</sup> K <sup>-1</sup>
Thermal conductivity coefficient (solid-liquid)	$k$	(0.74-0.439) W m <sup>-1</sup> K <sup>-1</sup>
Latent heat of fusion	$L_e$	83740 J kg <sup>-1</sup>
Viscosity	$\mu$	(0.024-0.0012) kg m <sup>-1</sup> s <sup>-1</sup>
Melting point temperature	$T_m$	415 K
Stable max operating temperature	$T_b$	811 K

2.4. Thermal energy conversion calculations in furnace with infrared rays

Thermal storage is achieved through the latent and sensible heat absorbed during the melting of these substances. The thermal energy storage system is typically analyzed in three stages: energy loading (charging), energy storage, and energy

discharge, as shown in Figure 7. When the furnace is considered as a closed system, the differences in energy entering and leaving the furnace are balanced by the sensible and latent heat stored within the furnace. It is assumed that no work is performed within the system and that there are no changes in kinetic or potential energy. The energy balance for the furnace

is given by Eq. (1) [14]. The amount of energy stored in the furnace is calculated by Eq. (2) [14-17].

$$\frac{d(m c_p T + mL)}{dt} = E_{fur,in} - E_{fur,out} \quad (1)$$

$$\Delta E = \dot{m}_l \beta c_p (T_l - T_a) + \dot{m}_l L + \dot{m}_s (1 - \beta) c_p (T_s - T_a) \quad (2)$$

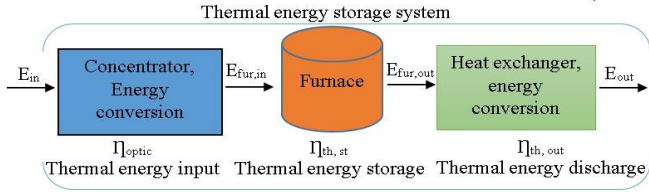


**Figure 7.** Energy balance status of the thermal energy storage system

For the charging state, the efficiency of the furnace, according to the first law of Thermodynamics, is calculated as the ratio of the energy stored in the furnace to the energy entering the furnace, as shown in Eq. (3) [18].

$$\eta_{th,st} = \frac{E_{st}}{E_{fur,in}} = \frac{\dot{m}_l \beta c_p (T_l - T_a) + \dot{m}_l L + \dot{m}_s (1 - \beta) c_p (T_s - T_a)}{I A \eta_{op}} \quad (3)$$

Where  $T_l$  (K) is the average temperature of the molten liquid state of the substance in the furnace,  $T_s$  (K) is the average temperature of the solid state of the substance in the furnace,  $T_a$  (K) is the ambient temperature,  $\beta$  is the liquid fraction of the molten substance,  $\dot{m}_l$  (kg/s) is the mass flow rate of the molten substance in the liquid state,  $\dot{m}_s$  (kg/s) is mass flow rate of the substance remaining from melting and  $E_{in}$  (W) is the amount of thermal energy entering the furnace. In order to find the energy entering the furnace, the heat flux of the infrared lamp to the concentrator was found. In order to find the heat flux, using the experimentally measured focal temperature values, the radiation value  $I$  (W/m<sup>2</sup>) coming to the receiver was calculated with Eq. (4) by using the heat transfer equation with radiation [19-21].

$$I = \frac{\varepsilon \sigma}{\eta_{op} \times C_R \times \alpha \times \tau} \times \left( \frac{T_{focal}}{F_B R_S} \right)^4 \quad (4)$$

The optical efficiency  $\eta_{op}$  is calculated as 83.2% with Eq. (5) based on the reflective surface coefficient (0.9) and rim angle (22.6°) of the conical concentrator [20,25]. Where, the focal temperature was used within the degradation factor ( $F_B = 0.9$ ) and cooling coefficient ( $R_S = 0.8$ ) range to be closer to reality, as a result of an experimental study [20].

$$\eta_{op} = \cos \theta_i \times \rho_{ref} \times (f_s \Gamma) \quad (5)$$

Where,  $\theta_i$  is the incident ray angle, assuming that there is no cosine loss  $\theta_i = 0$  are taken,  $\rho_{ref}$  concentrator reflective surface coefficient is taken as 0.9, and the shading and intercept factor is calculated by Eq. (6) [20,25].

$$f_s \Gamma = \frac{\sin^2 \theta_R - \sin^2 \theta_{min}}{4 \tan^2 \left( \frac{\theta_R}{2} \right)} \quad (6)$$

Also, the shadow angle ( $\theta_{min}$ ) is taken as zero assuming that there is no shadow at the focus and. The concentrator rim angle was found to be  $\theta_R = 22.6^\circ$  as seen in Table 1. The geometric concentration ratio ( $C_R = A_c/A_f$ ) is calculated as approximately

6.11. The permeability coefficient ( $\tau$ ) is taken as 0.92 for quartz glass through authorized companies.

The absorption coefficient of paraffin in the furnace with a penetration distance of 30 cm was found to be 0.6 [26]. As the thickness of the paraffin sample increases, its absorption coefficient increases and its permeability decreases. Using the emissivity model proposed by Astarita and Carlomagno [27] and a refractive index of 1.43 presented by Mark and Kroschwitz [28], a wall emissivity of 0.91 was found for paraffin wax [29, 30]. Table 4 shows the emissivity and absorption coefficient ranges of paraffin and Hitec salt. The emissivity of Hitec salt varies in the range of 0.6-0.8 for the melt temperatures between 150 and 400 °C and wavelengths between 500 and 1000 nanometers [31]. Hitec salt has a spectral absorption coefficient of 160-220 (m<sup>-1</sup>) in the wavelength range of 500-1000 nanometers at the melt temperature of 150-400 C. This value shows that hitec salt has a very high absorption coefficient ( $\alpha=0.95$ ) in the liquid state [31].

**Table 4.** The emissivity and absorption coefficient ranges of paraffin and Hitec salt [26-31]

Materials	Emissivity, $\varepsilon$	Absorption coefficient, $\alpha$
Paraffin	(0.91-0.95)	0.6±0.05
Hitec salt	(0.6-0.8)	0.9±0.05

### 2.5. Numerical CFD calculation

In the numerical method, the melting states and temperature values of the materials in the furnace were determined using ANSYS Fluent program. ANSYS Fluent is a CFD software using the finite volume method. Initially, the PCMs are in a solid state, with the PCM's starting temperature set at 300 K. The assumptions made during numerical modelling are as follows:

- 1- 2D state is considered as transient regimes.
- 2- The motion of PCMs in liquid state is incompressible, Newtonian and the flow is laminar.
- 3- While the viscosity of PCM varies, its density and thermal conductivity are assumed to change linearly.
- 4- Viscous heating and volume expansion are neglected.
- 5- PCM is considered isentropic and homogeneous.

Accordingly, continuity with Eq. (7), energy with Eq. (8), momentum with Eq. (9) for two dimensional transient laminar flow are given below [32, 33]. Continuity:

$$\frac{\partial \rho_f}{\partial t} + \nabla \cdot (\rho_f \vec{U}) = 0 \quad (7)$$

Energy:

$$\frac{\partial (\rho_f H)}{\partial t} + \nabla \cdot (\rho_f \vec{U} H) = \nabla \cdot (k_f \nabla T) \quad (8)$$

Momentum:

$$\begin{aligned} \frac{\rho}{\varepsilon} \frac{\partial u}{\partial t} + \frac{\rho_f}{\varepsilon^2} (\vec{U} \nabla u) &= - \frac{\partial p}{\partial x} + \frac{\mu_f}{\varepsilon} \nabla^2 u + S_u \\ \frac{\rho}{\varepsilon} \frac{\partial v}{\partial t} + \frac{\rho_f}{\varepsilon^2} (\vec{U} \nabla v) &= - \frac{\partial p}{\partial y} + \frac{\mu_f}{\varepsilon} \nabla^2 v + \rho_f g \beta_{te} (T - T_m) + S_v \end{aligned} \quad (9)$$

$$(10)$$

In the above conservation equations,  $\vec{U}$  is the fluid velocity,  $\rho_f$  is the density,  $\mu$  is the dynamics viscosity,  $P$  is the pressure,  $g$  is the gravitational acceleration,  $k$  is the thermal conductivity,  $\beta_{te}$  is the coefficient of thermal expansion. In addition,  $H$  is the

total enthalpy of the molten material and is calculated as the sum of sensible enthalpy and latent heat as follows.

$$H = h + \Delta H = h_{ref} + \int_{T_{ref}}^T c_p dT + \beta L_{sf} \quad (11)$$

$\beta$  for the melt liquid fraction is defined as follows [32, 34, 35].

- If  $T < T_s$ ,  $\beta = 0$ . If  $T > T_l$ ,  $\beta = 1$ .
- If  $T_s < T < T_l$  at the interface  $\beta = \frac{T - T_s}{T_l - T_s}$

The momentum loss due to decreasing porosity in the partially solid region was calculated with Eq. (12) [32, 35]

$$S = \frac{(1-\beta)^2}{(\beta^3 - \epsilon)} A_{mush}(\vec{U}) \quad (12)$$

Here  $\epsilon$  is a very small number (0.001) to avoid division by zero [35] and the coefficient  $A_{mush}$  is a mushy zone constant which is fixed at a value of  $10^5 \text{ kg m}^{-3} \text{ s}$  [32].

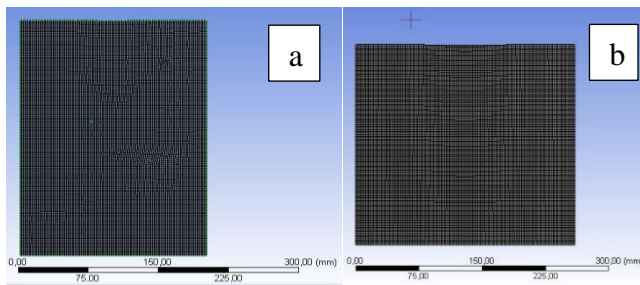


**Figure 8.** 2D mesh structures of the relevant furnaces; a) paraffin and b) Hitec salt

**2.5.1. Numerical CFD calculation of furnace filled with paraffin**

First, the initial and boundary conditions were determined for the paraffin solution in the Fluent program. In accordance with the experimental conditions, the mesh structure of the furnace filled with paraffin, with dimensions of 20x28 cm, is shown in Fig. 8a. Due to the large number of elements and nodes in the furnace model and the lengthy computation time required for numerical analysis (which depends on the computer's processing speed), faster results were obtained by designing a 2D model. The element size for paraffin in this model is 2 mm, with 14,278 nodes and 14,039 elements. The mesh structure was created as uniform in CFD Fluent to achieve more realistic results based on element size. For the boundary conditions of the model, the focal surface temperature was set to 100 °C, and

all other surfaces were assumed to be insulated ( $q'' = 0$ ). In this model, the flow was assumed to be laminar with a low velocity. The coupling between pressure and velocity was solved using the SIMPLE algorithm, with pressure-velocity fields, momentum, and continuity equations. For pressure interpolation, the PRESTO method was chosen, as it is suitable for any mesh structure. The energy and momentum equations were solved using second-order upwind, and the transient formulation equations were set to second order. For paraffin, the optimal time step was 0.3 s, and the number of iterations was set to 25 to achieve stable temperatures and increasing melting rates.

**2.5.2. Numerical CFD calculation of furnace filled with Hitec salt**

The mesh structures of the furnace filled with Hitec salt with dimensions of 26x26 cm are given in Figure 8b. This furnace has a mesh structure with an element size of 2 mm, number of nodes 16,632 and number of elements 16,375, and a skewness value of 0.9. In the transient regime, energy, solidification and melting equations were selected in the modelling. Hitec salt was chosen as the fluid material and the focal point was assumed to be 200 °C and the other surfaces were insulated with 1 mm steel material depending on the experimental conditions as the boundary condition. This Hitec furnace model was numerically analysed similar to paraffin. In this model, the viscous flow was chosen to be laminar with low velocity assumption. The coupling between pressure and velocity using the pressure and velocity fields, momentum and continuity equations is solved with the SIMPLE algorithm. For pressure interpolation, PRESTO was chosen. The energy and momentum equations are second order upwind and the transient formulation equations are second order. For Hitec salt, the optimal time step was 0.3 s and the number of iterations was 25.

**2.6. Uncertainty analysis of heat storage system with infrared ray**

Uncertainty analysis is performed due to measurement errors and assumption errors made for numerical and experimental thermal analysis. Some error values of this system; Error due to thermocouple pairs  $\pm 0.75 \text{ }^\circ\text{C}$ , Average error due to digital thermometer  $\pm 0.5 \text{ }^\circ\text{C}$ , Average error in furnace interior temperature measurement  $\pm 3^\circ\text{C}$ , Surface reflection angle 2%, Incident beam angle 2% and Incident light power error 5%. According to these data, the total uncertainty ratio of the infrared ray concentrator system is calculated as approximately 6.5% with the uncertainty equation obtained by Kline and McClintock [36]. This uncertainty value is suitable for the experimental data.

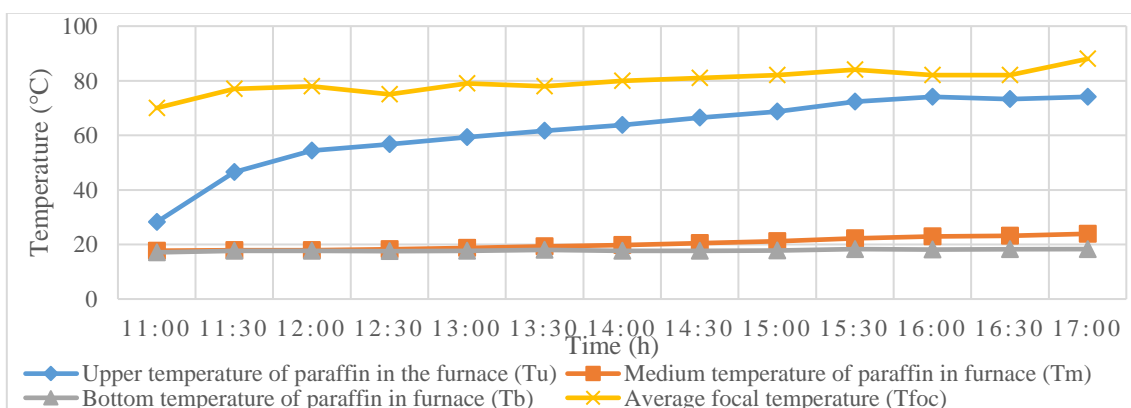


**Figure 9.** Variation of furnace temperatures with respect to time in the first experiment with paraffin

**3. Results**

The differences and similarities of paraffin and Hitec salt materials in thermal energy storage were investigated in the laboratory using experimental and numerical CFD methods and the results are presented.

*3.1. Experimental data in laboratory environment*

*3.1.1. Experimental data on thermal energy storage with paraffin*

The data obtained from the paraffin melting experiment with an infrared lamp, when the ambient temperature was between

17 °C and 19 °C, are presented graphically in Figure 9. In the 28 cm high furnace, it can be observed that the temperature in the upper region gradually approaches the focal temperature over time. As paraffin began to melt at approximately 60 °C, the temperature in the upper region increased. Due to the low thermal conductivity, the average temperature in the bottom region of the paraffin in the furnace remained around 19 °C. Approximately 0.7 kg of paraffin was melted over the 4-hour duration of the experiment. Based on this, the melting flow rate was calculated to be approximately 0.047 g s<sup>-1</sup> using the 500 W infrared lamp power.

**Table 5.** Paraffin heat storage charging experiment data

Time	Upper temperature of paraffin T <sub>u</sub> , (°C)	Middle temperature of paraffin T <sub>m</sub> , (°C)	Bottom temperature of paraffin T <sub>b</sub> , (°C)	Average focal temperature T <sub>foc</sub> , (°C)	Paraffin focal surface temperature T <sub>s</sub> , (°C)	Ambient temperature T <sub>a</sub> , (°C)
11:00	30,2	17,8	17,75	170	76	18
11:30	38,45	18,1	17,95	200	79	18
12:00	48,45	18,3	18,05	220	82	19
12:30	60,9	18,8	18,15	211	81	19
13:00	68,3	19,35	18,15	213	83	19
13:30	73,1	20,05	18,35	210	83	19
14:00	77,2	20,8	18,5	213	80	19
14:30	77,8	21,5	18,55	210	80	19
15:00	78,6	22,1	18,65	210	80	19

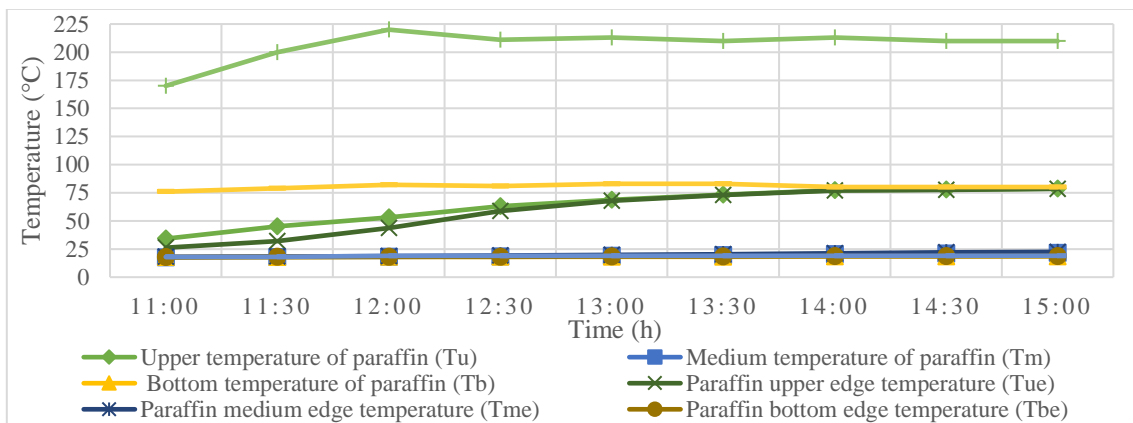


**Figure 10.** Furnace temperature curves of the second charging experiment with paraffin

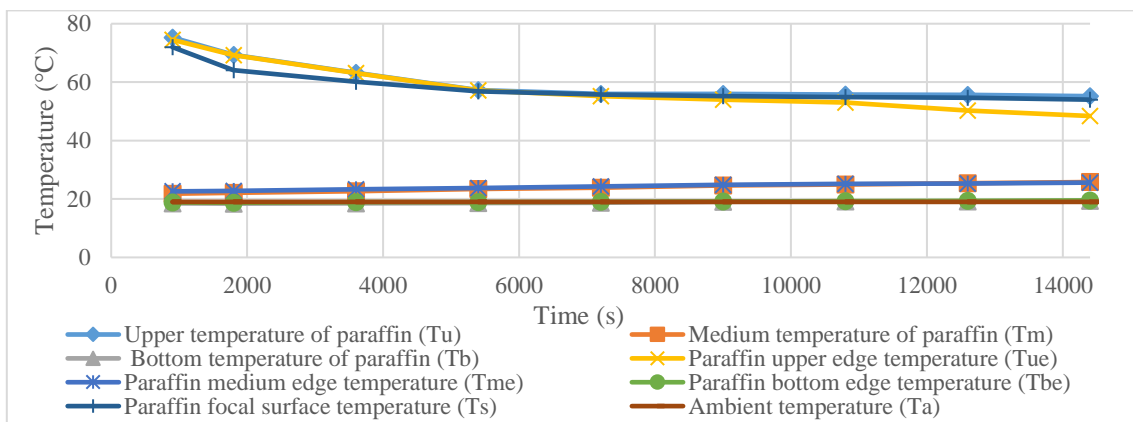


**Figure 11.** Temperature curves of the furnace depending on time in case of paraffin discharge

The paraffin thermal energy storage charging experiment is carried out by keeping the top surface temperature at approximately 80 °C considering the paraffin evaporation

temperature as shown in Table 5. As seen in Figure 10, the average focal temperature is 210 °C, while higher temperatures are obtained in the upper region. Due to the low thermal



conductivity of paraffin, the temperature change in the bottom regions of the furnace is slow.

Figure 11 shows that in the case of paraffin discharge, the upper region temperature is 75 °C and dropped to approximately 55 °C after 4 hours. In the bottom regions of the furnace, a slight increase continues, indicating that the stored energy can be used for at least 6 hours.

**3.2. Experimental data on thermal energy storage with Hitec salt**

The infrared lamp used had a power of 500 W, and the infrared rays were concentrated in a focal surface area of about 8 cm using a conical concentrator. In the experiment, conducted at an ambient temperature of 20 °C, it was observed that the Hitec salt began to melt in approximately 10 minutes. Additionally, reflection losses between the infrared lamp and the conical concentrator were reduced in this experiment. The average data obtained from the thermal energy storage experiment using the infrared lamp are presented in Table 6. Furthermore, Figure 12 illustrates the graph showing the variation of the focal and furnace temperatures over time during the infrared lamp experiment. The focal temperature varied between approximately 280 °C and 300 °C, while an average temperature of 220 °C was observed on the upper surface of the furnace during the charging process. After 4 hours, the temperature in the upper region of the furnace reached 116 °C. Meanwhile, the temperature of the Hitec salt in the middle region of the furnace increased over time, with the highest

temperature measured at 87 °C. The rate of temperature increase in the middle region was lower compared to the measurements taken at the bottom of the furnace, where the highest temperature measured was 39 °C.

In these experiments, the furnaces were insulated with glass wool and only the upper region had an opening through which the rays entered. In the second experiment with Hitec salt, the focal area was covered with a quartz glass to reduce the loss of natural convection in the furnace.

In the discharge state, measurements were continued when the infrared lamp charging experiment was completed. The temperature values measured for two hours are given in Table 7. In addition, in the discharge condition, Figure 13 shows the furnace internal temperature change graph according to time. According to this, Hitec salt temperatures remained approximately constant in the bottom region of the furnace for two hours. The temperature in the middle region of the furnace, which is 86°C at the beginning, decreased by 65% to 56°C after two hours. The temperature of the upper region inside the furnace is observed to decrease more rapidly due to the heat loss from the furnace open to the atmosphere.

At the end of the discharge phase, it was observed that the average temperature of the upper region of the Hitec salt in the furnace dropped from approximately 102 °C to 46 °C. Thus, it has been revealed that with the current size of Hitec salt, the stored thermal energy can be transferred to the usage area for at least 4 hours.

**Table 6.** Data obtained from Hitec salt experiment with infrared lamp

Time (s)	Focal temperature (°C)	Focal temperature in the furnace (°C)	Upper temperature of Hitec salt in the furnace (°C)	Middle temperature of Hitec salt in the furnace (°C)	Bottom temperature of Hitec salt in the furnace (°C)
1800	316	210	49	36	22
3600	300	212	72	45	23
5400	290	218	80	56	24
7200	290	240	85	64	27
9000	280	230	95	69	29
10800	281	222	104	82	34
12600	280	219	112	86	34
14400	276	215	116	87	35

**Table 7.** Data obtained from the Infrared lamp experiment for the discharge state

Time (s)	Upper temperature of Hitec salt (°C)	Middle temperature of Hitec salt (°C)	Bottom left edge temperature of Hitec salt (°C)	Bottom right edge temperature of Hitec salt (°C)
900	102	86	28	37
1800	85	77	28	37
2700	75	72	28	38
3600	70	69	27	38
4500	63	64	27	38
5400	58	61	27	38
6300	57	58	27	37
7200	55	56	27	37

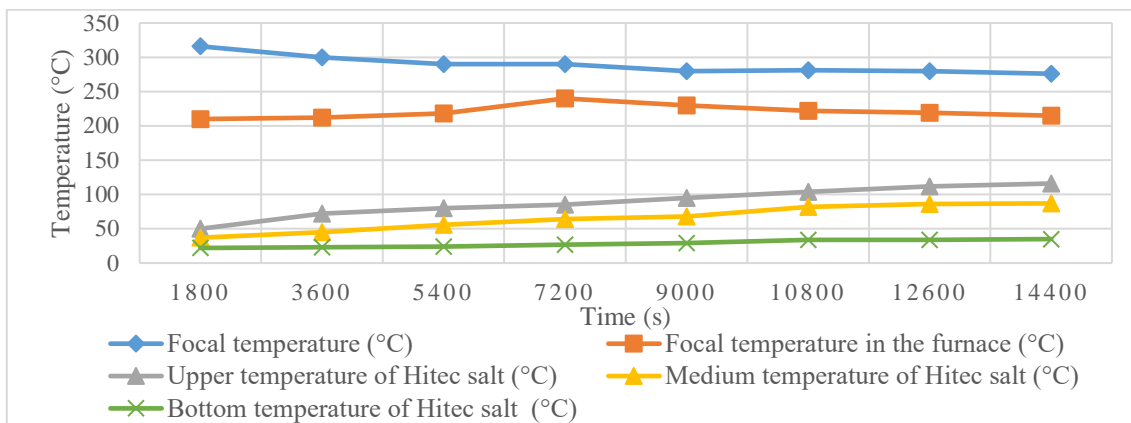


Figure 12. Variation of Hitec salt temperatures with time for the charging state of the furnace

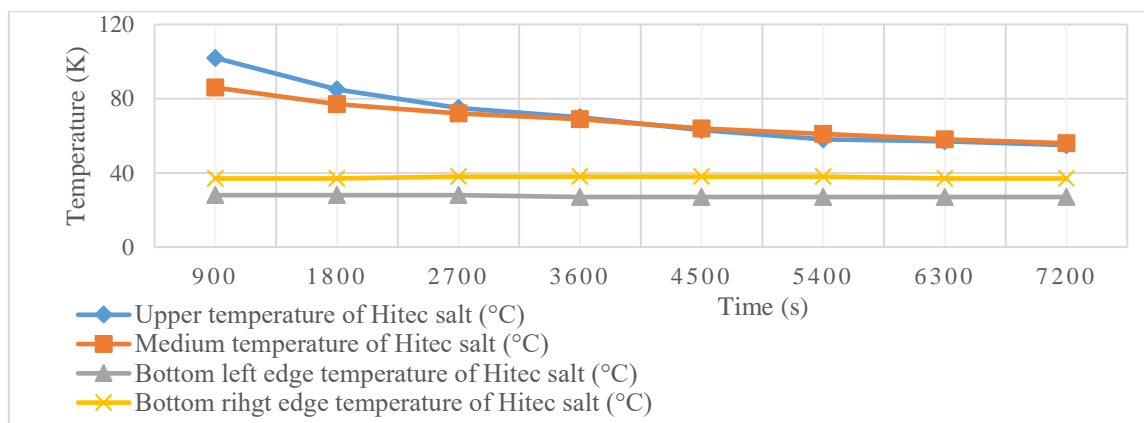


Figure 13. Temperature change of the furnace with Hitec salt according to time in the experiment conducted in discharge state

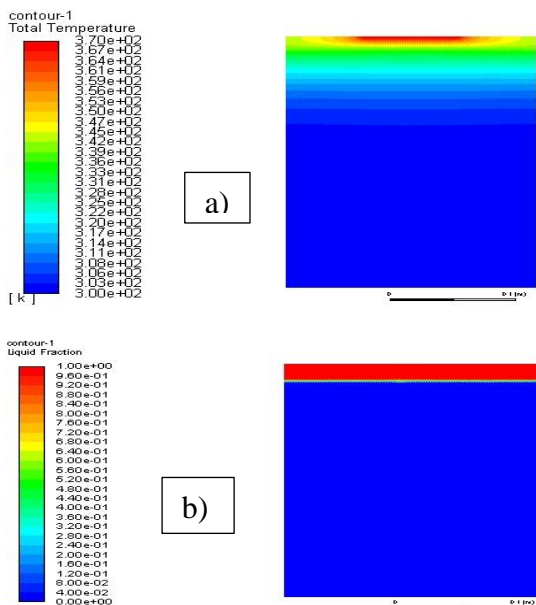


Figure 14. Contours of paraffin in the furnace in numerical analysis; a) temperature and b) melting

3.2. Numerical CFD results

Numerical CFD results for the melting and temperature conditions of paraffin and Hitec salt are given below.

3.2.1. Numerical CFD results for paraffin in storage furnace

The temperature and melting contours of the data obtained from numerical paraffin melting solidification modelling at the end of four hours are given in Figure 14. As seen in Figure 14a,

while the focal temperatures are kept at the vaporization temperature of paraffin, the regions close to the focal point are at higher temperatures, while the temperature change at the bottom of the furnace is very small. In Figure 14b, the melting rate of paraffin is approximately 7% and the mass flow rate is calculated as  $3.69 \times 10^{-5}$  kg/s. Due to the low coefficient of conductivity of paraffin, heat transfer towards the furnace bottom was found to be slow.

3.2.2. Numerical CFD results for Hitec salt in the storage furnace

According to the data obtained in the numerical analysis with Hitec salt, the focal point temperature (475 K) is kept higher than paraffin for the melting of Hitec salt. The temperature contours of Hitec salt at the end of 6 hours in numerical analysis are given in Figure 17a and melting contours in Figure 17b. As seen in Figure 17a, the temperature in the middle region of the furnace is around 86°C, and the temperature in the upper region is around 116°C, which is in agreement with the experimental data. As can be seen in Figure 18, the average temperature of Hitec salt increases and the average temperature reached at the end of 4 hours is 328 K. The volumetric fraction of liquid melted increased with time, reaching 3.1% after 4 hours and approaching 6% after 6 hours as shown in Figure 19. Figure 15 also shows that the temperature of the entire paraffin in the furnace increased over time. Additionally, Figure 16 demonstrates that the liquid portion of the paraffin in the furnace, in the melting state, increased over time. It has been found that the temperature distribution and melting rates obtained experimentally are approximately similar to each other.

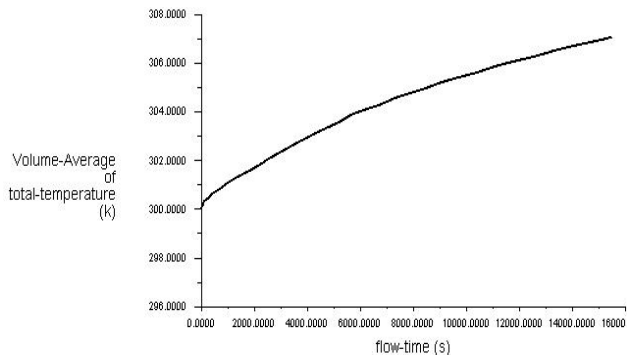


**Figure 15.** Variation of all paraffin temperature in the furnace with time

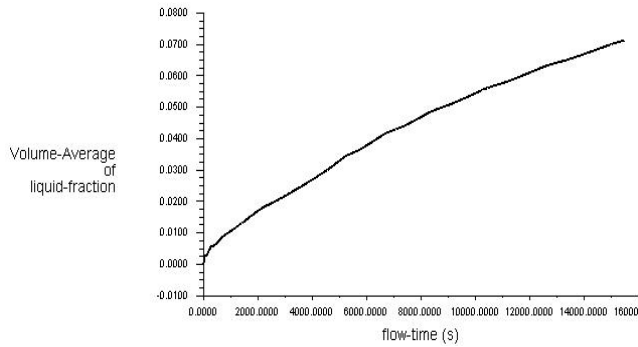


**Figure 16.** Variation of the liquid fraction ( $\beta$ ) of paraffin in the furnace with time

**4. Discussion**

**4.1. Verifying and comparing of paraffin and Hitec salt data**

In the Figure 20 shows the variation of numerical and experimental data of paraffin with time. Accordingly, the temperature and melting rates obtained for paraffin are close to each other. In Figure 21 shows the variation of numerical and experimental data of Hitec salt with time. For Hitec salt, numerical and experimental data are shown parallel increases in the gaseous state.

The melting rates and mass flow rates obtained for paraffin and Hitec salt according to the data obtained according to experimental and numerical methods are given in Table 8. According to this table, while the melting rate was 8.9% in the furnace with 7.6 kg of paraffin, the melting rate was 3.4% in the furnace with 26 kg of Hitec salt. When compared in terms of mass flow rate, the mass flow rate of Hitec salt is higher than paraffin. At the end of 4 hours, the mass flow rates of PCMs in the furnace were determined as 0.047 g s<sup>-1</sup> and 0.061 g s<sup>-1</sup> for Paraffin and Hitec, respectively.

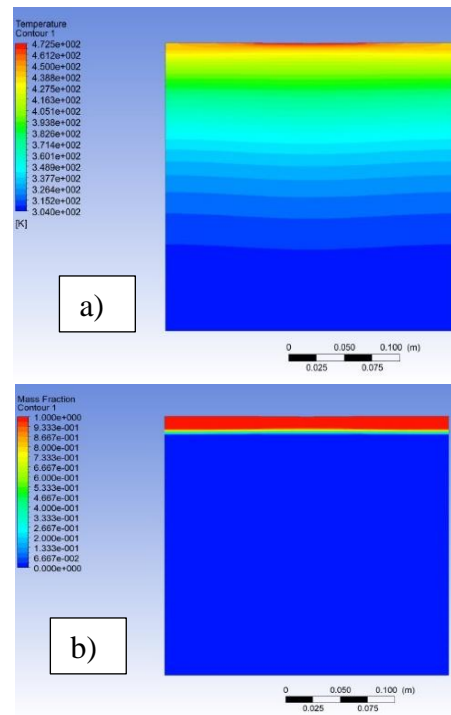


**Figure 17.** Contours of Hitec salt in the furnace numerically; a) Temperature and b) melting

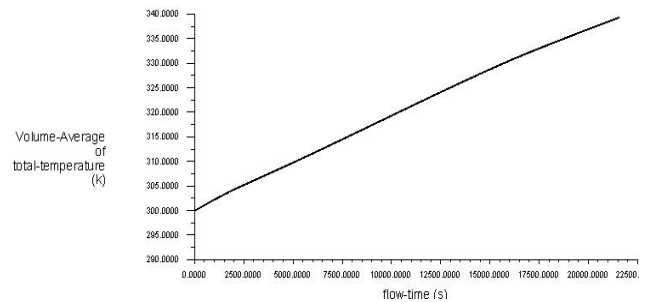


**Figure 18.** Variation of all Hitec salt average temperature in the furnace with time

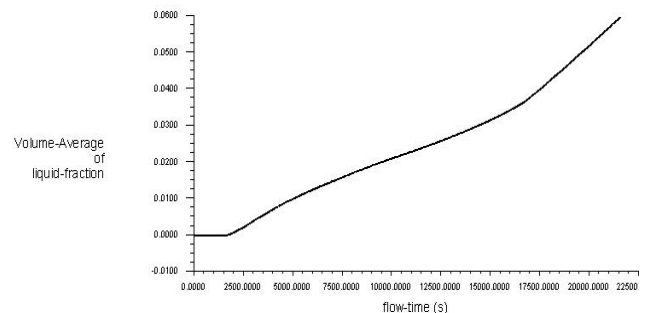


**Figure 19.** Variation of the liquid fraction ( $\beta$ ) of Hitec salt in the furnace with time

**Table 8.** Melting flow rates and melting rates in the furnace for paraffin and Hitec salt

Method	Paraffin Melting ratio $\beta$ (%)	Mass flow ratio $\dot{m}$ (g s <sup>-1</sup> )	Hitec Melting ratio $\beta$ (%) salt	Mass flow ratio $\dot{m}$ (g s <sup>-1</sup> )
Experimental	8.9	0.047	3.4	0.061
Numerical	7	0.037	3.1	0.056

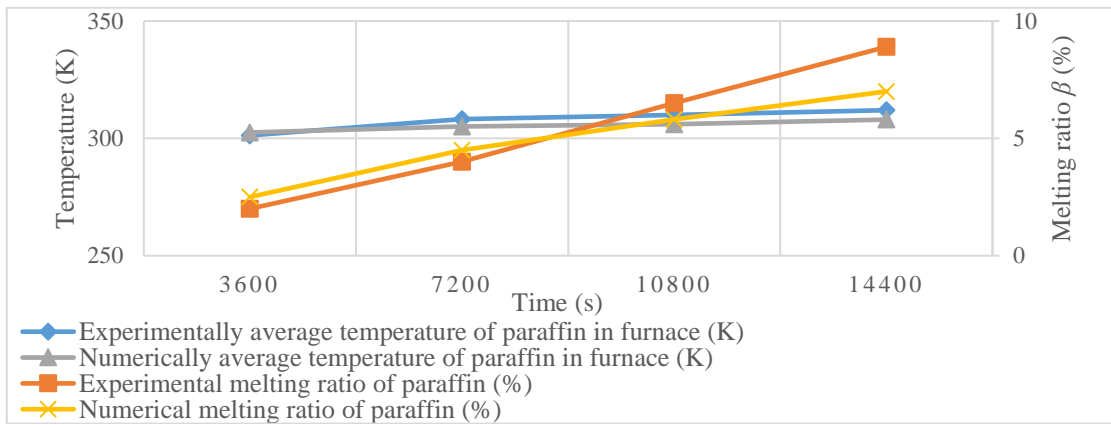


Figure 20. Comparison of numerical and experimental data for paraffin

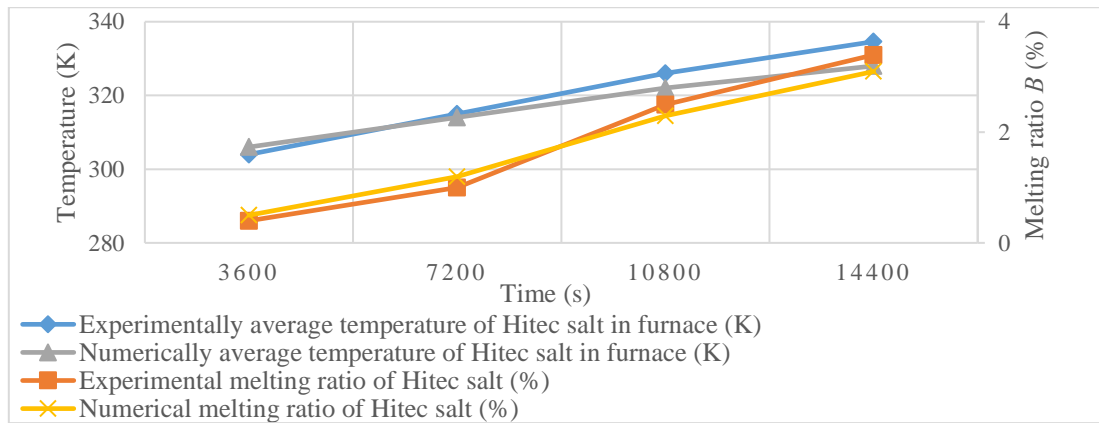


Figure 21. Comparison of numerical and experimental data for Hitec salt

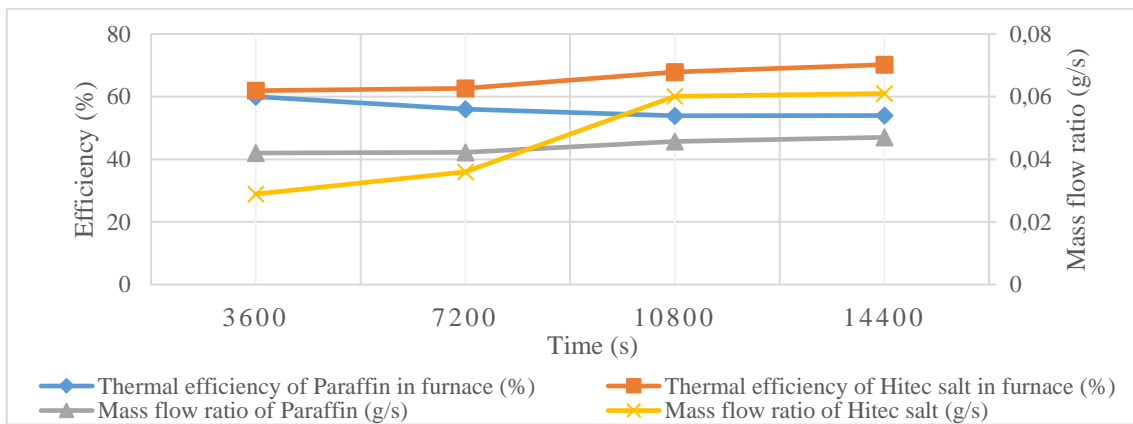


Figure 22. Thermal efficiency and mass flow rates of paraffin and Hitec salt in the furnace with time

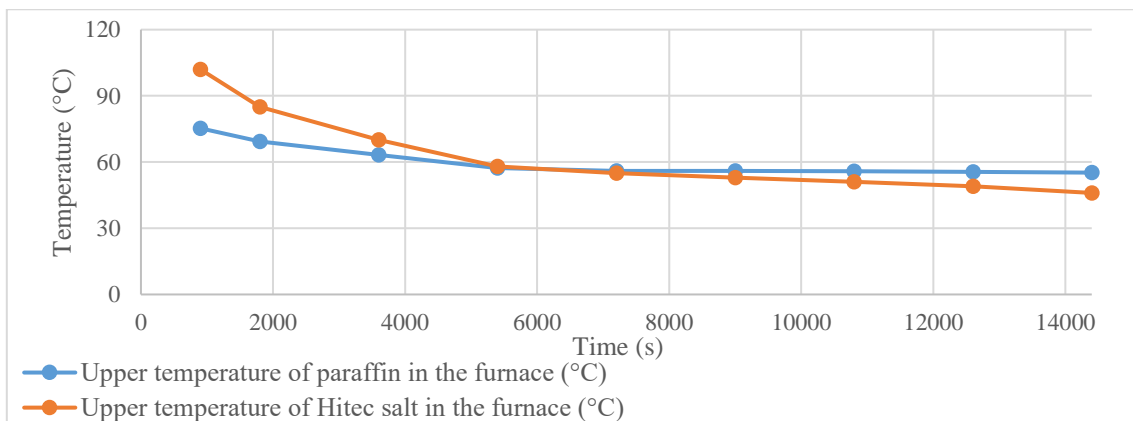


Figure 23. Time dependent temperature curve of Paraffin and Hitec salt for discharge condition

According to the focal temperatures measured in the experiments, the heat flux on the focal region of the furnace containing paraffin was calculated as  $1218 \text{ W m}^{-2}$ , while the heat flux on the focal region of the furnace containing Hitec salt was calculated as  $1955 \text{ W m}^{-2}$  with Eq. 4. Based on the experimental data with Eq. 4, the theoretically calculated heat fluxes of the infrared lamp were calculated as  $3716 \text{ W m}^{-2}$  for paraffin and  $8447 \text{ W m}^{-2}$  for Hitec. These heat fluxes were used in the thermal efficiency equations. The thermal efficiency and mass

flow rates of paraffin and Hitec salt in the furnace varying with time are given in Figure 22. The average thermal efficiency of paraffin in the furnace was calculated to be approximately 56%, while the average thermal efficiency of Hitec salt in the furnace was calculated as 65.6%. Additionally, the first law of thermodynamics efficiency ( $\eta_{\text{total}} = Q_{\text{st}}/Q_{\text{in, electric}}$ ) calculated for paraffin and Hitec salt are 8% and 19.7%, respectively. In this efficiency, 500 W electrical energy given to the system was used as the input energy.

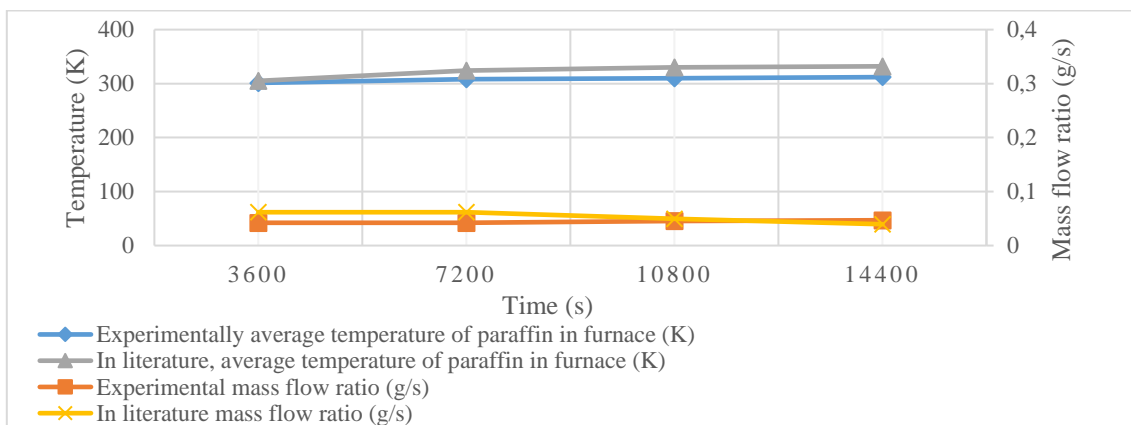


Figure 24. Comparison of this study with paraffin melting experiments of different sizes in the literature

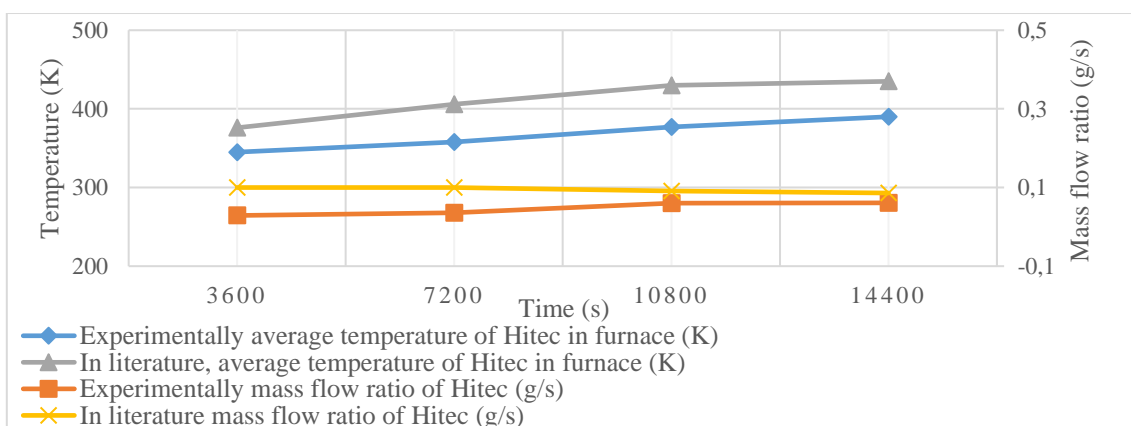


Figure 25. Comparison of similar literature on the melting of Hitec salt

According to the experimental results in the discharge, the graph of paraffin cooling at a slower rate than Hitec salt is given in Figure 23

#### 4.2. Comparison of paraffin and Hitec salt with studies in the literature

The experimental data with paraffin in this study were compared with some studies in the literature by Ambarita et al. [23]. Accordingly, the temperature change graph of paraffin in the furnace obtained when heat input was made from different regions (side) and when a similar temperature ( $80 \text{ }^\circ\text{C}$ ) input was made is given in Figure 24. It is seen that the melting flow rates obtained for  $0.89 \text{ kg}$  paraffin with dimensions of  $(10 \times 10 \times 10) \text{ mm}$  in the literature and  $7.6 \text{ kg}$  paraffin in this study are close to each other. As in the literature, the melting flow rate is high at the beginning due to the heat given to the furnace from the side. In addition, the temperature difference is observed due to the low heat conduction coefficient according to the size difference of the furnaces.

The overall four tests confirmed that paraffin and beeswax have good ability to store heat energy at the temperature above  $32 \text{ }^\circ\text{C}$  for over 8 hours in infant incubator [37]. In this study, it

is revealed that the paraffin temperature varies between  $60\text{-}80 \text{ }^\circ\text{C}$  for 4 hours in the discharge state and is suitable for long-term heat storage.

In the literature, melting experiments conducted by Xiao et al. [24] on Hitec salt, heat transfer was made to furnaces of different sizes (cylindrical with a diameter of  $95 \text{ mm}$  and a length of  $300 \text{ mm}$ ) from different surfaces. Despite these size differences, the literature study conducted with a temperature of  $160 \text{ }^\circ\text{C}$  applied to an equal surface reached melting flow rates in the range  $(0.06\text{-}0.08) \text{ g s}^{-1}$  similar to the study in this article, as seen in Figure 25. Considering the melting region in this study and the literature, there was little difference in Hitec salt temperatures since they have different surface areas and heat input surfaces. The study conducted by Xiao et al. on Hitec salt, for charging and discharging conditions, the furnace top temperature and middle temperatures in the experimental data in this article are compared in the graph in Figure 26 [24]. Accordingly, while the temperatures in the regions close to the heater are high, the temperatures in the regions approximately  $5 \text{ cm}$  away from the heater are lower. It is seen that the temperatures of the region  $5 \text{ cm}$  away from the heater ( $T_6$ ) are close to the furnace top and middle region temperatures in this

article. In the discharge condition, it is seen in Figure 26b that the T6 temperature point and the upper and middle temperatures have similar cooling curves.

Finally, if the infrared lamp simulators are compared, firstly, A radiation power of up to 2100 W with a maximum peak flux of 2700 kW m<sup>-2</sup> was presented by Bellan et al. [38]. Secondly, by Kuhn and Hund, Using a 20 kW lamp, the simulator achieved a peak flux of approximately 16,000 kW m<sup>-2</sup> and measured a

radiation power of 3000 W inside a square with a side of 7 cm. Based on the lamp's electrical input, the conversion efficiency to radiation energy was 17% [39]. In this article, a heat flux of approximately 8500 W m<sup>-2</sup> is achieved with a 500 W powerful infrared lamp, while the energy conversion efficiency is calculated as 19.7%. In addition, the focal heat flux can be increased by reducing reflection and optical losses in the focal area of approximately 8 cm.

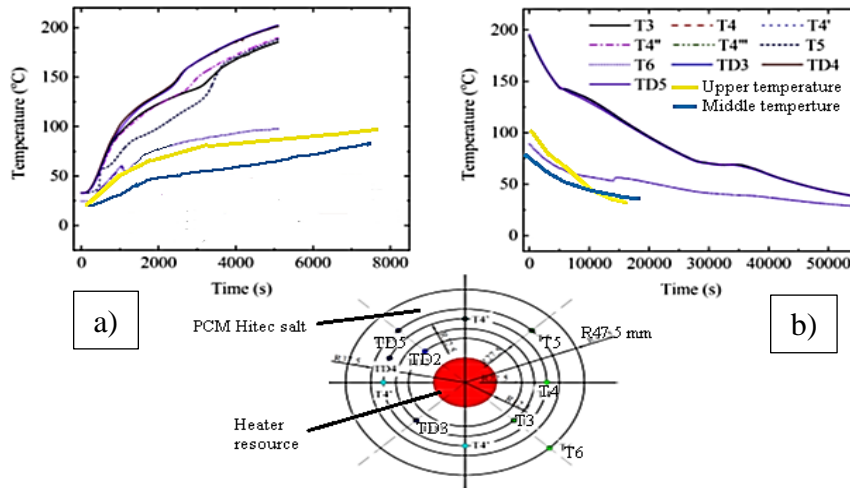


**Figure 26.** Temperature comparison with a study in the literature on Hitec salt a) in charge and b) in discharge [24]

4.3. Economic analysis of the system

The cost of the installed ray concentrator and heat storage system is quite low. The cost of all components of the system is listed in Table 9. The total installation cost was calculated to be \$300. In addition to the installation cost, there is the electricity consumption of the infrared lamps. The infrared lamp power used for the designed ray concentrator system is 500 W. In this case, if the unit price of electricity in Turkey for 2024 is approximately 0.067 \$/kWh, the infrared lamp concentrator system consumes approximately \$0.0338 per kWh.

It is aimed to reduce electricity costs by storing 4 more hours of thermal energy with the electricity given in the charging state.

**Table 9.** Component and total cost values of the whole system

Product/material/process	Unit price [\$]	Total price [\$]
Infrared lamp 500 W	10	20
Furnace1 (stainless steel)	75	75
Furnace2 (glass)	10	10
Reflective foil	20	20
Metallic sheet	10	10
Quartz glass	20	20
Sodium Nitrate	2.5	25
Potassium Nitrate	3	30
Sodium Nitrite	2.5	25
Paraffin	3.5	35
Consumables and labour	30	30
<b>Total [\$]</b>		<b>300</b>

In the system operating with Hitec salt, about 30% of the electricity consumed is stored as thermal energy, thus reducing electricity consumption costs. By spending approximately \$0.134 for 0.5 kW of power over 4 hours, at least 0.8 kW of thermal energy is stored in 8 hours. Therefore, to convert the

infrared ray concentrator system into useful work, it is sufficient to operate it for 4-6 hours instead of 8 hours. Additionally, the installation cost of the Hitec salt heat storage system was calculated to be \$255. If the system operates for 12 hours a day, the installation cost is covered in approximately 2.5 years.

The installation cost of paraffin was calculated as \$145. The amount of thermal energy stored in 8 hours with the paraffin heat storage system was obtained as an average of 0.32 kW. In order to convert this system into useful work, it is sufficient to run it for 4-6 hours instead of 8 hours. If the heat storage system with paraffin is operated for 12 hours a day, it can cover the installation cost in 1.7 years.

Thermoeconomic analysis was calculated as the ratio of the energy loss ( $Q_{loss}$ ) of the whole system to the total heat storage system installation cost ( $Z_{inst}$ ) [40]. The Thermoeconomic analysis of the whole system was calculated as 3.17 W/\$ and 1.56 W/\$ for paraffin and Hitec salt, respectively. In this case, it is seen that Hitec salt has less thermal energy loss and is more economical. On the other hand, using the same 500 W source for paraffin increased the thermal energy loss. It is recommended to use infrared light source with lower power for paraffin to prevent evaporation. Finally, in order to increase the Thermoeconomic efficiency of both storage systems, methods that increase heat transfer within the furnace should be used.

In this study, the operation and maintenance (O&M) cost of the infrared radiation thermal energy storage system was calculated to be approximately 97 \$/kW per year. The thermal energy storage costs were determined to be 195 \$/kWh for paraffin and 166 \$/kWh for Hitec salt. In previous literature, it was reported that the O&M cost for the parabolic trough type thermal energy storage system with a power capacity of 100 MW, which can provide 6 hours of thermal storage with molten salts, ranged from 60 \$/kW to 70 \$/kW, while the thermal energy storage cost varied between 50 \$/kW and 80 \$/kWh [41]. It was found that the thermal energy storage costs per unit were

higher for small-scale storage systems than for large-scale systems. In this study, the capital costs were determined to be 3625 \$/kW for paraffin and 2550 \$/kW for Hitec salt, while the capital costs for trough-type thermal energy storage systems were reported to range from 6400 \$/kW to 10,700 \$/kW [42]. These results indicate that the capital costs of energy storage systems increase as their storage capacities grow.

## 5. Conclusions

Through the infrared lamp thermal energy storage system, sufficient temperatures were reached to melt the materials used, as confirmed by experimental and numerical methods. As a result, a new thermal energy storage method was tested. It was demonstrated that the heat transfers in the system, achieved through radiation and convection, made it safer by eliminating the risks of electrical conduction and short circuits, particularly in the salts within the furnace.

In the experiments for the Hitec salt charging condition, the focal temperature varied between approximately 280-300°C, while the average temperature of the upper region of the furnace was 220°C, and the temperature of the middle region of the furnace increased over time, reaching 87°C after 4 hours. On the other hand, after the 4-hour paraffin charging experiment, the focal temperature was recorded at 210°C, the upper region temperature at 80°C, and the middle region temperature at 22°C.

At the beginning of the discharge, the temperature of the Hitec salt was 102°C, and the temperature of the paraffin was 75.3°C. After 4 hours, the temperature of the Hitec salt dropped to 46°C, while the temperature of the paraffin decreased to 55.2°C. The slower cooling of paraffin was attributed to its lower thermal conductivity. The stability of Hitec salt at higher temperatures makes it highly suitable for medium and high-temperature applications.

The mass flow rates of the phase change materials in the furnace, measured using the infrared artificial ray method, were 0.047 g s<sup>-1</sup> for paraffin and 0.061 g s<sup>-1</sup> for Hitec salt, respectively. The average thermal efficiency of paraffin in the furnace was calculated to be approximately 56%, while the average thermal efficiency of Hitec salt was calculated to be 65.6%. Additionally, the first law of thermodynamics efficiency (total efficiency) for paraffin and Hitec salt was calculated to be 8% and 19.7%, respectively. As a result, paraffin is found to have a high heat storage capacity for low-temperature applications (up to around 80°C). However, for heat storage at medium and high temperatures, the Hitec salt mixture, an inorganic salt with a low melting point, high specific heat capacity, and stable operation at high temperatures, is considered more suitable.

The installation cost of the ray concentrator system is low. Additionally, the electricity required for the system can be supplied by a photovoltaic (PV) panel, making the system more economical. For high-temperature applications, such as those using Hitec salt, the reflective surface should be made of polished metal rather than foil to ensure temperature resistance. Finally, methods to improve heat transfer in the furnace should be developed to facilitate faster melting inside the furnace.

## Acknowledgements

This article was financially supported by YÖK 100/2000 Project and TÜBİTAK BİDEB 2211-C. Also, this article is based on Ali Kemal Özcan's doctoral thesis completed in May 2024.

## Author contributions

Ali Kemal Özcan: data curation, investigation, methodology, formal analysis, software, visualization; resources, writing-original draft, writing-review & editing.

Ömer Öksüz: data curation, investigation, visualization, roles/writing - original draft, writing - review & editing.

Cevdet Demirtaş: supervision, project administration, formal analysis, conceptualization, investigation.

## References

- Kraiem, M., Karkri, M., Fois, M., & Sobolciak, P., Thermophysical Characterization of Paraffins versus Temperature for Thermal Energy Storage, Buildings, **2023**, 13(4):877
- Gallo, A., Marzo, A., Fuentealba, E., & Alonso, E., High flux solar simulators for concentrated solar thermal research: A review, Reviews, Renewable and Sustainable Energy **77**, **2017**, 1385-1402
- Ahmad, S., Hand, R., & Wieckert, C., Use of concentrated radiation for solar powered glass melting experiments, Solar Energy **109**, **2014**, 174-182
- Sari, A., & Karaipekli, A., Thermal conductivity and latent heat thermal energy storage characteristics of paraffin/expanded graphite composite as phase change material, Applied Thermal Engineering, **2007**, 27(8-9):1271-1277
- Akgun, M., Aydin, O., & Kaygusuz, K., Thermal energy storage behavior of a paraffin during melting and solidification. Energy Sources, Part A, **2007**, 29(14):1315-1326
- Arslan, B., & Ilbas, M., A numerical study on the melting behaviors of paraffin with and without Al<sub>2</sub>O<sub>3</sub> nanoparticles, Journal of Polytechnic, **2021**, 24(3): 1243-1248
- Sinaringati, S., Putra, N., Amin, M., & Afriyanti, F., The utilization of paraffin and beeswax as heat energy storage in infant incubator, ARPN Journal of Engineering and Applied Sciences, **2016**, 11(2):800-804
- Pedrosa, P., Marcelo, T., Nogueira, C.A., Gomes, A., & Diamantino, T., Molten nitrate salts containing lithium as thermal energy storage media: a short review, (ECOS) Proceedings of the 31st International Conference on Efficiency, Cost, Optimization, Simulation and Environmental Impact of Energy Systems, **2018**
- Fernandez, A.G., Galleguillos, H., Fuentealba, E., & Perez, F.J., Thermal characterization of HITEC molten salt for energy storage in solar linear concentrated technology, Journal of Thermal Analysis and Calorimetry, **2015**, 122,3-9
- Lingayat, A., Das, P., Gilago, M.C., & V.P., C. A detail assessment of paraffin waxed thermal energy storage medium for solar dryers, Solar Energy, **2023**, 261, 14-27
- Chauhan, V., Yadav, A., & Soni, S., Simulation of Melting Process of a Phase Change Material (PCM) using ANSYS (Fluent), International Research Journal of Engineering and Technology (IRJET), **2017**, 04(05):3289-3294
- Coastal Chemical Company, HITEC Heat Transfer Salt Houston, HITEC Heat Transfer Salt, **2011**
- Ivenson, B., Broome, S., Kruizenga, A., & Cordaro, J. Thermal and Mechanical Properties of Nitrate Salt Thermal Storage Salts in the Solid-Phase, Solar Energy, **2012**, 86, 2897-2911

14. Dinçer, İ., & Rosen, M., *Thermal energy storage: Systems and applications* (2. edition), Hoboken, N.J.: Wiley, **2011**
15. Lane, G. A., and Lane, G.A. eds. *Solar heat storage: latent heat materials*. Vol. 1. Boca Raton, FL, USA: CRC press, **1983**
16. Sharma, A., Tyagi, V. V., Chen, C. R., & Buddhi, D., Review on thermal energy storage with phase change materials and applications, *India: Renewable and Sustainable Energy Reviews*, **2009**, 13(2):318-345
17. Subramaniam, S.B., & Senthil, R., Heat transfer enhancement of concentrated solar absorber using hollow cylindrical fins filled with phase change material, *International journal of hydrogen energy*, **2021**, 46(43):22344-22355
18. Sansaniwal, S. K., Sharma, V., & Mathur, J., Energy and exergy analyses of various typical solar energy applications: A comprehensive review, *Renewable and Sustainable Energy Reviews*, **2018**, 82, 1576–1601
19. Stine, W., & Diver, R., *A Compendium of Solar Dish/Stirling Technology*, California, US: Sandia National Laboratories, **1994**
20. Castellanos, L. M., Caballero, G. C., Cobas, V. M., Lora, E. S., & Reyes, A. M. Mathematical modeling of the geometrical sizing and thermal performance of a Dish/Stirling system for power generation. *Renewable Energy*, **2017**, 107, 23-35
21. Özcan, A.K., and Demirtaş, C., Obtaining high temperatures with ring array type (Rac) solar concentrators. 23rd Congress on Thermal Science and Technology with International Participation (ULIBTK'21), **2021**, 1, 640-646
22. Tetreault-friend, m., Gray, l., Berdibek, s., Mckrell, t., & Slocum, a., Optical properties of high temperature molten salt mixtures for volumetrically absorbing solar thermal receiver applications, *Solar Energy*, **2017**, 153, 238-248
23. Ambarita, H., Abdullah, I., Siregar, C.A., Siregar, R.E.T., Ronowikarto, A.D., Experimental Study on Melting and Solidification of Phase Change Material Thermal Storage, *IOP Conference Series: Materials Science and Engineering*, **2017**, 180, 012030
24. Xiao, X., Jia, H., Wen, D., & Zhao, X., Thermal performance analysis of a solar energy storage unit encapsulated with HITEC salt/copper foam/nanoparticles composite, *Energy*, **2020**, 192, 116593
25. Jaramillo, O. "Transporte de energía solar concentrada a través de fibras ópticas: acoplamiento fibra-concentrador y estudio térmico." Bachelor Thesis. Universidad Autónoma de Morelos. Estado de Morelos. México, **1998**
26. Ma, M., Ai, Q., and Xie, M. Optical properties of four types paraffin, *Optik - International Journal for Light and Electron Optics*, **2022**, 249, 168277
27. Astarita, T.; Carlomagno, G.M. *Infrared Thermography for Thermo-Fluid-Dynamics*, Springer: **2013**
28. Mark, F.H.; Kroschwitz, J.I. *Encyclopedia of Polymer Science and Engineering*; Wiley: New York, NY, USA, **1989**,17
29. Migliorino, M.T., Bianchi, D., and Nasuti, F., Numerical Simulations of the Internal Ballistics of Paraffin–Oxygen Hybrid Rockets at Different Scales, *Aerospace*, **2021**, 8(8): 213
30. Farnham, C., Nakao, M., Nishioka, M., and Nabeshima, M., Quantification of the Effect of Cooling Mists on Individual Thermal Comfort, *The seventh International Conference on Urban Climate*, **2009**
31. Xie, M., Zhu, Y., Liu, Y., Yuan, Y., and Tan, H., Measurement of spectral radiative characteristics of molten salt at high temperature using emission method, *Applied Thermal Engineering* **2019**, 149, 151–164
32. Darzi, A.A.R., Moosania, S.M. Tan, F.L., Farhadi, M., Numerical investigation of free-cooling system using plate type PCM storage, *International Communications in Heat and Mass Transfer*, **2013**, 48, 155–163
33. Zhang, P., Xiao, X., Meng, Z., & Li, M., Heat transfer characteristics of a molten-salt thermal energy storage unit with and without heat transfer enhancement. *Applied Energy*, **2015**, 137, 758–772
34. Voller, V., and Prakash, C., A Fixed-Grid Numerical Modeling Methodology for Convection-Diffusion Mushy Region Phase-Change Problems, *Int. J. Heat Mass Transfer* **1987**, 30, 1709 -1720
35. Hassab, M., Sorour, M., Mansour, M., and Zaytoun, M., Effect of volume expansion on the melting process's thermal behavior, *Applied Thermal Engineering*, **2017**, 115, 350–362
36. Kline, S., and McClinton, F., Describing Uncertainties in Single-Sample Experiment, *Mechanical engineering*, **1953**, 75, 3-9
37. Sinaringati, S., Putra, N., Amin, M., and Afriyanti, F., The utilization of paraffin and beeswax as heat energy storage in infant incubator, *ARPN Journal of Engineering and Applied Sciences*, **2016**, 11(2):800-804
38. Bellan, S., Alonso, E., Gomez-Garcia, F., Perez-Rabago, C., Gonzalez-Aguilar, J., Romero, M., Thermal performance of lab-scale solar reactor designed for kinetics analysis at high radiation fluxes, *Chemical Engineering Science*, **2013**, 101, 81–89
39. Kuhn, P., and Hunt, A., A new solar simulator to study high temperature solid-state reactions with highly concentrated radiation, *Solar Energy Materials*, **1991**, 24, 742–750
40. Rosen, M., and Dincer, I., Exergoeconomic analysis of power plants operating on various fuels, *Applied Thermal Engineering* **2003**, 23, 643–658
41. Turchi, C., Mehos, M., Ho, C. K. & Kolb, G. J. Current and future costs for parabolic trough and power tower systems in the US market, Conference paper NREL CP, **2010**, 5500-49303
42. Roubaud, E. G., Pérez-Osorio, D., Prieto, C. Review of commercial thermal energy storage in concentrated solar power plants: Steam vs. molten salts, *Renewable and Sustainable Energy Reviews*, **2017**, 80, 133–148